A surface science view onto cuprous oxide: Growth, termination, electronic structure and optical response

Niklas Nilius, Jacek Goniakowski, Claudine Noguera

▶ To cite this version:

Niklas Nilius, Jacek Goniakowski, Claudine Noguera. A surface science view onto cuprous oxide: Growth, termination, electronic structure and optical response. Surface Science Reports, 2024, 79 (1), pp.100622. 10.1016/j.surfrep.2024.100622 . hal-04584815

HAL Id: hal-04584815
https://hal.sorbonne-universite.fr/hal-04584815

Submitted on 23 May 2024

A Surface Science View onto Cuprous Oxide: Growth, Termination, Electronic Structure and Optical Response

Niklas Nilius
Carl von Ossietzky Universität, Institut für Physik, D-26111 Oldenburg, Germany
niklas.nilius@uni-oldenburg.de

Jacek Goniakowski, Claudine Noguera
CNRS-Sorbonne Université, UMR 7588, INSP, F-75005 Paris, France
jacek.goniakowski@insp.jussieu.fr, claudine.noguera@insp.jussieu.fr

Table of Content:

Keywords: copper oxide, cuprous oxide, surface, oxidation, termination, reconstruction, structure, atomistic models, adsorption, electronic properties, optical properties, doping, scanning tunneling microscopy, density functional theory

Abstract:

The oxides of copper have attracted the attention of scientists already for more than hundred years. This fascination is fueled by many outstanding properties of the material, for example, a semiconducting behavior that led to the first diode fabricated in electronics, a pronounced excitonic response that stimulated an intense search for Bose-Einstein condensation, and a pivotal role in unconventional superconductivity. Despite this central position in past and present research activities, many aspects of copper oxides are not sufficiently understood to date. This applies in particular to their surface characteristics, where even fundamental questions, such as the energetically favored termination of low-index Cu_2O and CuO planes, are still subject of debates. This review aims at addressing these deficiencies by compiling state-of-the-art knowledge of the surface science of copper oxides, and especially of cuprous oxide.

A first focus of the article lies in the oxidation characteristic of copper as a means to prepare well-defined oxide surfaces. It demonstrates that low-pressure oxidation only results in the formation of ultrathin precursor oxides, with properties deviating substantially from those of the bulk material. Consequently, reliable pathways to produce high-quality and bulk-compatible surfaces, either of Cu_2O thin films or bulk crystals, are presented. The following chapter provides a comprehensive introduction into the atomic structure of the most relevant Cu_2O surfaces, i.e., the (111), (100) and (110) planes. It gives an overview of important diffraction and microscopy experiments on the most accessible Cu_2O terminations, and complements this with state-of-the-art theoretical studies to develop corresponding atomistic models. The chapter closes by presenting the atomic configurations of the most relevant Cu_2O surfaces at given thermodynamic conditions.

Chapter four develops a surface-science view onto the unique optical response of cuprous oxide. After introducing the well-known bulk behaviour, it highlights how optical properties can be probed on surfaces with high spectral and spatial resolution. The chapter discusses how optical near-field techniques are employed to analyze oxide excitons and their trapping at lattice defects in real-space experiments. The last chapter summarizes efforts to alter intrinsic Cu_2O properties, e.g., the p-type conductivity, the width of the band gap and the exciton trapping and recombination behavior, via doping. It illuminates this topic from an experimental and theoretical viewpoint and highlights several unsolved questions related to the topic.

Despite considerable efforts, this review can only present the current state of knowledge on Cu_2O surfaces, a subject that continuously advances due to new scientific findings and innovations. We nonetheless hope that it provides a comprehensive and topical overview of the unusual properties of this fascinating oxide system.

1. Introduction

The oxides of copper belong to most fascinating and most intensively studied binary oxide materials in physics and chemistry. The reasons behind are their outstanding functionality, as far as the electronic, optical and chemical characteristics are concerned, and their broad availability with copper being the 28th most abundant element in the earth crust. This review article focusses on the surface properties of copper oxides, thus aims at complementing the many insightful articles on the bulk oxide material.[1,2,3]

Following the primary Cu oxidation states, +1 and +2, two main oxide phases can be distinguished that is cuprous oxide (Cu(I)-oxide, Cu_2O) and cupric oxide (Cu(II)-oxide, CuO) (Fig. 1). Moreover, a mixed valence phase, Cu_4O_3, exists with 50% of the Cu ions in +1 and 50% in +2 oxidation state. Cuprous oxide, being in the center of this work, can be found as the natural mineral cuprite and is known for its beautiful and intense red color (Fig. 1a). The coloring gives a first hint on the band gap of the material that amounts to 2.15 eV and allows only red/orange light to be transmitted. Cuprous oxide crystallizes in a cubic lattice with *Pn3m* space group (4.27 Å lattice parameter), whereby the Cu and O ions occupy the fcc and bcc sites of the cube, respectively. Moreover, the structure comprises two Cu-O sub-lattices, being shifted against each other by ¼ of the cube diagonal. Cupric oxide, on the other hand, naturally occurs as tenorite, a black-colored mineral with a reduced band gap of 1.35 eV (Fig. 1b). The oxide crystallizes in a mono-clinic lattice (space group *C2/c*) with angles β = 100° and α, γ = 90°. Finally, Cu_4O_3 or paramelaconite adopts a tetragonal lattice with *I41/amd* space group and has an indirect band gap of 1.34 eV (direct gap 2.47 eV, Fig. 1c).[4,5]

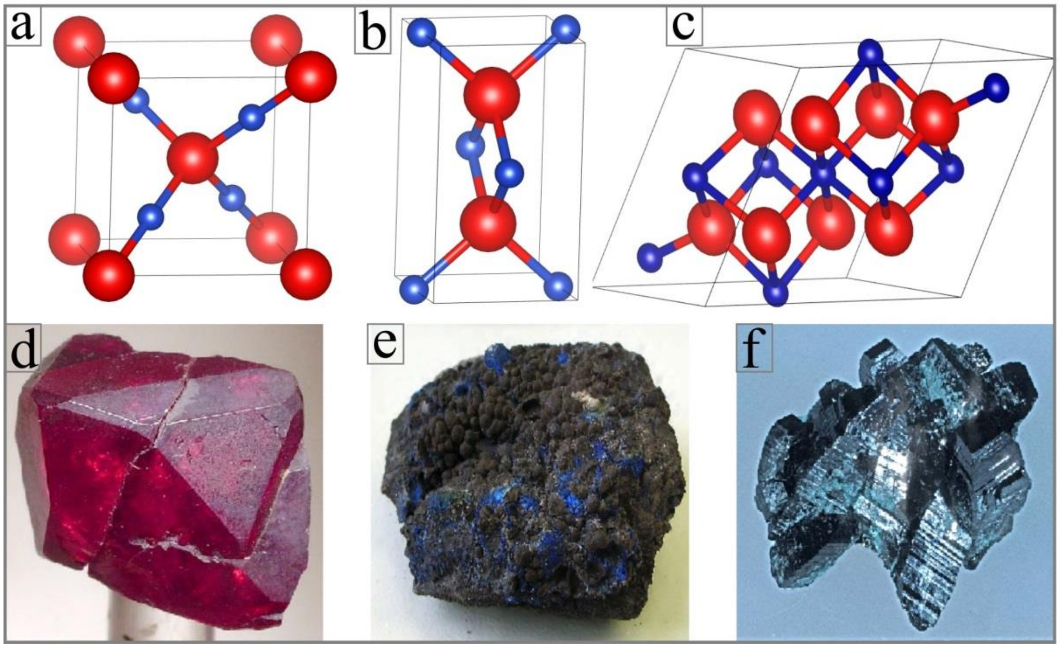

Figure 1: Crystal structures of (a) Cu_2O, (b) CuO and (c) Cu_4O_3 and photographs of the corresponding minerals. [Adapted from wikipedia]

Many unique properties render the copper oxides relevant for fundamental research and technical applications. In contrast to other binary oxides, they exhibit a pronounced p-type conductance behavior due to the low formation enthalpy of Cu vacancies (V_{Cu}) in the lattice.[6,7] The associated holes float up in the band structure and occupy delocalized states at the valence band (VB) top, ensuring high hole mobility. In contrast, charge-compensating defects, such as O vacancies and interstitials, have high formation enthalpies and get inserted into the Cu-O lattice at much lower quantities than the V_{Cu} defects.[7] Note that most other binary oxides feature n-type conductance behavior, as the formation enthalpy of O vacancies is low and hole states produced by cationic defects tend to localize in the band gap.[8] A robust p-type conductance response is found for both, Cu_2O and CuO, with the former one having higher carrier densities.[9]

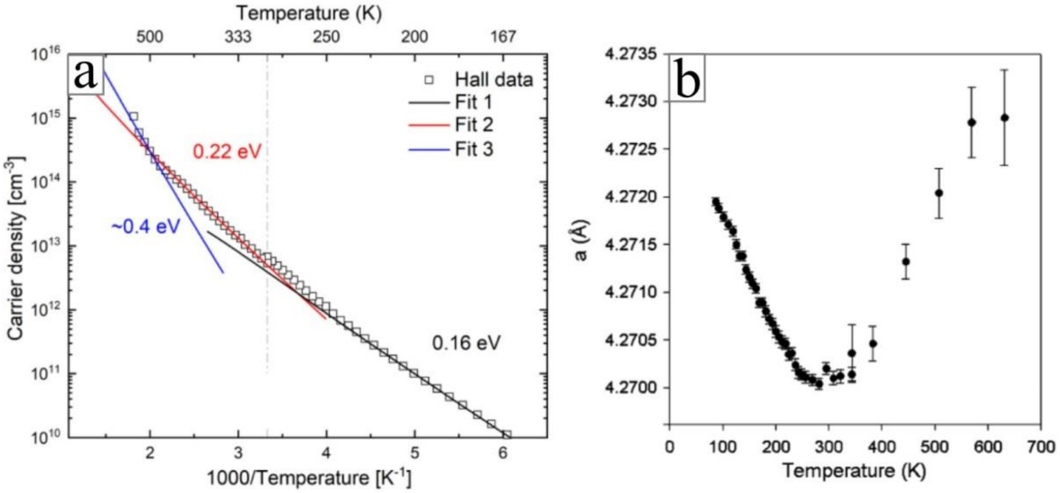

Figure 2: (a) Hole concentration versus inverse temperature as determined by Hall measurements for a Cu_2O single crystal. Arrhenius fits are indicated by solid lines, the corresponding activation energies are assigned to Cu vacancies (0.22 eV) and nitrogen acceptors (0.16 eV).[10] (b) Temperature-dependent lattice parameter of Cu_2O from X-ray diffraction measurements.[16]

Not all questions related to the p-type nature of copper oxides are comprehensively answered by now. Temperature-dependent conductivity measurements on Cu_2O, for example, appear to be incompatible with the V_{Cu} acceptor levels calculated by density functional theory (DFT).[10] Two types of V_{Cu} defects have been identified in the Cu_2O lattice, a simple vacancy produced by removing one Cu ion from the otherwise intact lattice, and a split vacancy, where an adjacent Cu ion relaxes towards the void to adopt a tetrahedral coordination with four O neighbors.[7,11] Depending on the computational approach, a variety of formation enthalpies have been calculated for the two vacancies, whereby the simple defect seems systematically preferred over the split one. Moreover, the (0/-) charging energy of simple V_{Cu} defects was found to vary between 0.23 eV[12] and 0.28 eV,[7] being in reasonable agreement with the results of deep-level transient spectroscopy.[13] Temperature-dependent conductance measurements, on the other hand, revealed a matching activation energy of 0.22 eV only in the temperature window from 200 to 500 K, while low-temperature data indicated acceptor energies as small as 0.16 eV (Fig. 2a).[10] This finding suggests the presence of another low-lying acceptor state in natural Cu_2O crystals, which was theortically connected to substitutional N-atoms on O lattice sites[14] or N_2 molecules replacing a lattice Cu atom.[15] Up to this point, the impact of nitrogen doping on the Cu_2O behavior could not be clarified, and the topic will thus be addressed later in the text.

Another peculiarity of cuprous oxide is its negative thermal expansion coefficient at temperatures between 100 and 300 K (Fig. 2b). It has been related to unidirectional phonon modes being excited perpendicular to the O-Cu-O bonds. As a result, the Cu_4O tetrahedrons undergo a tilting in the lattice and reduce their mutual distance at increasing temperature.[16]

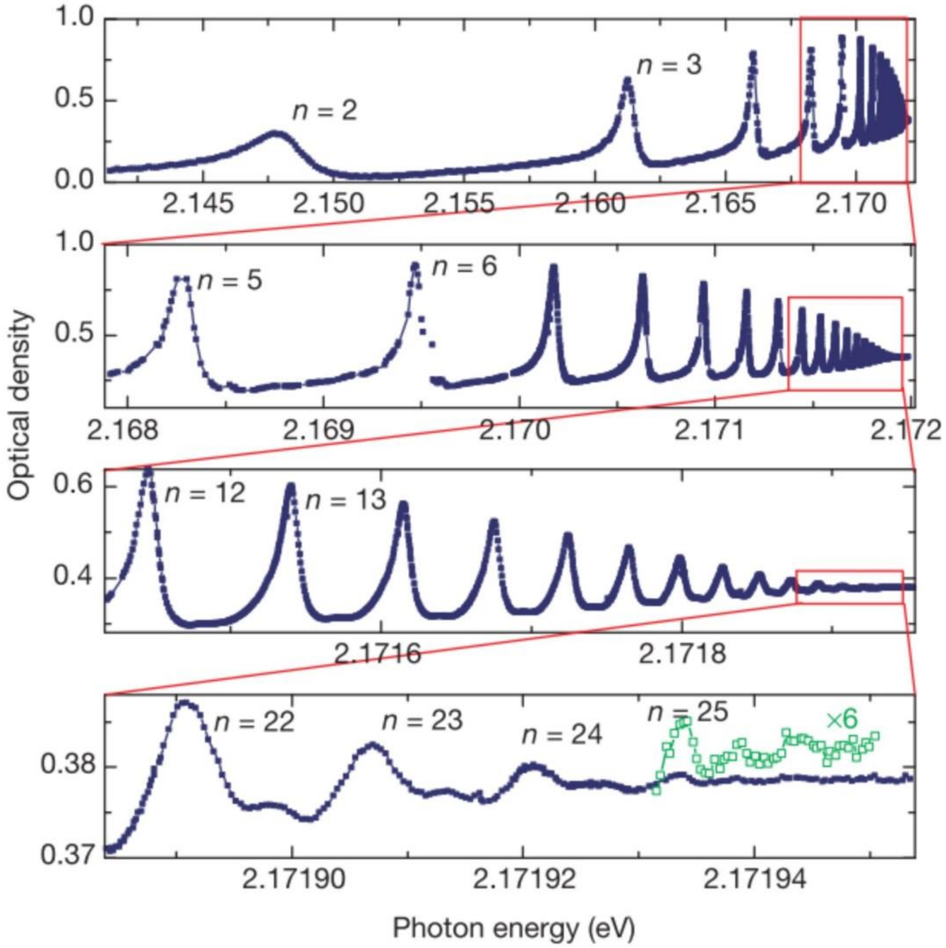

Figure 3: High-resolution absorption spectra of Cu_2O excitons measured with a single-frequency laser on a natural oxide crystal at 1.2 K. Peaks correspond to exciton resonances with different principal quantum number.[18]

A major research spotlight of cuprous oxide focusses on its rich optical response, as governed by a set of para- and ortho-excitons and their trapping behavior at Cu and O defects in the lattice. The Cu_2O excitons have exceptionally large ground-state binding energies of ~140 meV, with the para-excitons being 12 meV more stable due to spin-exchange interactions.[17] Correspondingly, numerous Rydberg excitons have been detected in high quality Cu_2O crystals (Fig. 3). In fact, Cu_2O holds the world record of the highest observed Rydberg state (n=25) among all excitonic systems.[18] Moreover, the high exciton binding energy renders Cu_2O an ideal material to explore bosonic condensation of electron-hole pairs.[19,20] However, unambigious evidence for the formation of excitonic condensates could not be provided so far. The condensation seems hampered by two-body collision processes at high exciton density, whereby one exciton recombines while the other decays into two unbound carriers. This decay channel drastically reduces the exciton lifetime and prevents condensation.[21]

The Cu_2O excitons have a dipole forbidden nature, which is a direct consequence of the Mott-Hubbard character of the oxide band gap. The hot electrons hereby occupy Cu *4s* derived CB states, the corresponding holes localize in the Cu *3d* bands at the VB top. Exciton recombination thus requires a change in the orbital momentum quantum number of $\Delta l = 2$. While radiative decay of para-excitons is spin-forbidden in addition, making them optically dark, ortho-excitons can recombine via phonon involvement.[22] Not surprisingly, the dipole forbidden nature gives rise to long radiative lifetimes,[23,24] and extended diffusion lengths of Cu_2O excitons, reaching up to 100 µm for para-excitons in ultraclean Cu_2O crystals.[25] Along their diffusion path, the excitons couple to defects and trapping at Cu and O vacancies gives rise to particularly strong luminescence peaks. The V_{Cu} mediated emission hereby locates at 940 nm, while peaks at 750 and 830 nm originate from radiative recombination via double and single-charged O vacancies in the Cu_2O lattice, respectively.[26]

The fascinating electronic and optical properties of copper oxides have initiated an intense search for technical applications. After discovery of the first diode behavior in a Cu/Cu_2O junction in 1933,[27] copper oxide was considered to be an auspicious material to fabricate semiconductor devices. However, the semiconductor revolution actually bypassed the Cu-O system due to difficulties to produce a clean and defect-free feedstock with controlled doping level. However, its p-type nature together with a direct-forbidden band gap in the visible spectral range renders Cu_2O interesting for solar-cell applications. The oxide matrix hereby simultaneously acts as absorber and hole conductor, whereas charge separation and electron collection takes place at the interface to an n-type material.[28] A prototypical all-oxide solar-cell design comprises Cu_2O/ZnO heterojunctions that have matching band alignments and good interfacial lattice registry at the same time.[29,30] Accessible light-to-current conversion rates remained low, however, with a maximum efficiency of about 2% reported in 2006.[31,32] The rather high defect concentration and the presence of parasitic recombination channels for hot carriers was found to be responsible for the low charge-separation efficiency, and still represents the main bottleneck for establishing a Cu_2O solar-cell technology.

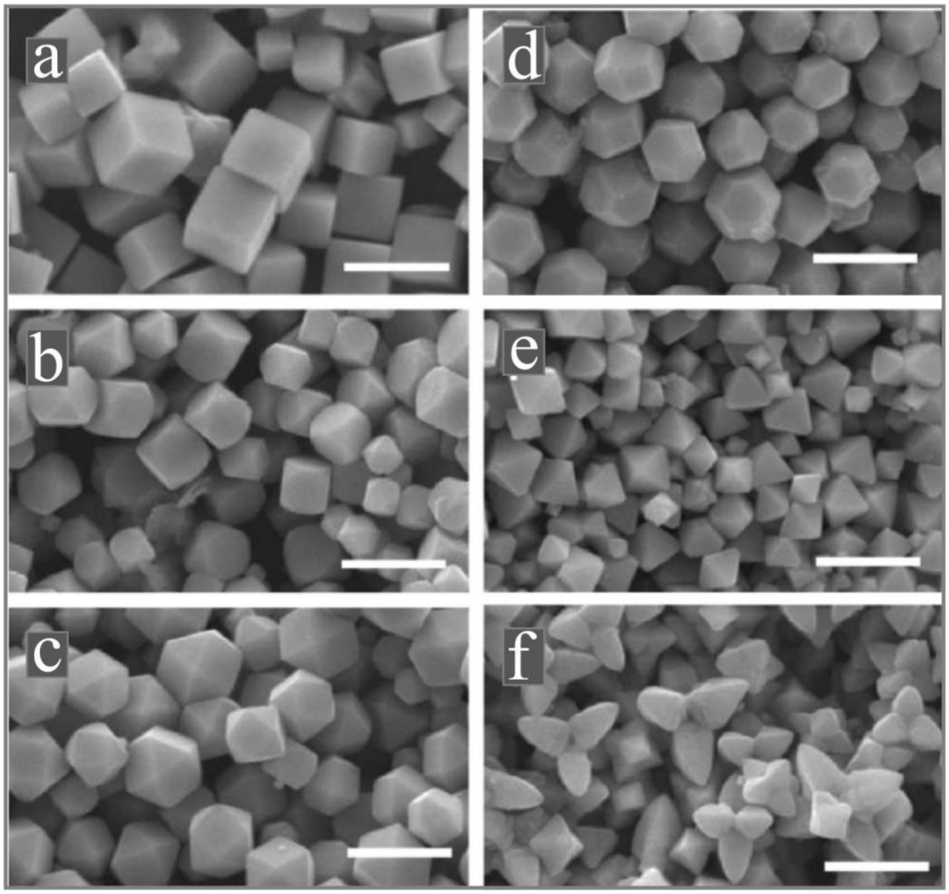

Figure 4: SEM images of shape-selected Cu_2O nanocrystals prepared with wet chemical, electrodeposition and solvothermal synthesis methods: (a) cubes, (b) truncated cubes, (c) cuboctahedrons, (d) truncated octahedrons, (e) octahedrons and (f) extended hexapods. All scale bars: 1 μm. Adapted from [36].

All applications discussed so far rely on the specific bulk properties of copper oxides, for which a mechanistic level of understanding has been achieved in the past years.[1] The situation is less satisfying as far as the surface properties of CuO and Cu_2O are concerned, and hardly any surface-science studies have been reported for Cu_4O_3.[33] Designated surface experiments have mostly been carried out with oxide nanoparticles, for which several, easily accessible preparation schemes are available. Low-dimensional oxide structures have consequently become a research spotlight in the last decade.[34,35,36] Cu-O nanoparticles can be fabricated with well-defined shapes nowadays, opening a convenient pathway to address the unique performance of a given oxide termination (Fig. 4).[37] Common routes towards facet engineering rely on the use of distinct precursor solutions, reduction conditions or calcination temperatures that favor the development of a certain oxide facet.[38]

By employing highly homogenous particle ensembles, the catalytic impact of individual Cu_2O facets can be addressed explicitly. For example, hydrogen and CO reduction experiments were used to determine the reactivity of cubic versus octahedral Cu_2O nanoparticles, exposing mostly (100) and (111) crystal facets, respectively.[39] Hereby, the onset temperature for oxide reduction was found to be ~100 K lower for octahedral particles, suggesting a higher reactivity of the $Cu_2O(111)$ surface. This finding is traditionally explained with the presence of low-coordinated Cu_{cus} ions in the bulk-cut (111) plane, although the availability of such sites in real surfaces was never proven and seems questionable in the light of studies presented in this article. The activity of (100) and (111) facets in light-driven hydrogen evolution reactions was probed by time-resolved photocurrent measurements performed with a transient photoelectron microscope (PEEM).[40] The experiments demonstrated ultrafast electron transfer from (111) to (100) facets to be a key component for the catalytic activity of the nanoparticles (Fig. 5). Even the charge flow between different facets of individual Cu_2O crystallites could directly be probed with a double-tip atomic force microscope (AFM).[41] Cu_2O and CuO nanoparticles finally exhibit a promising, yet hardly elucidated potential to serve as chemical sensors, e.g. for CO, or as building blocks for supercapacitors and high-duty batteries.[42,43,44]

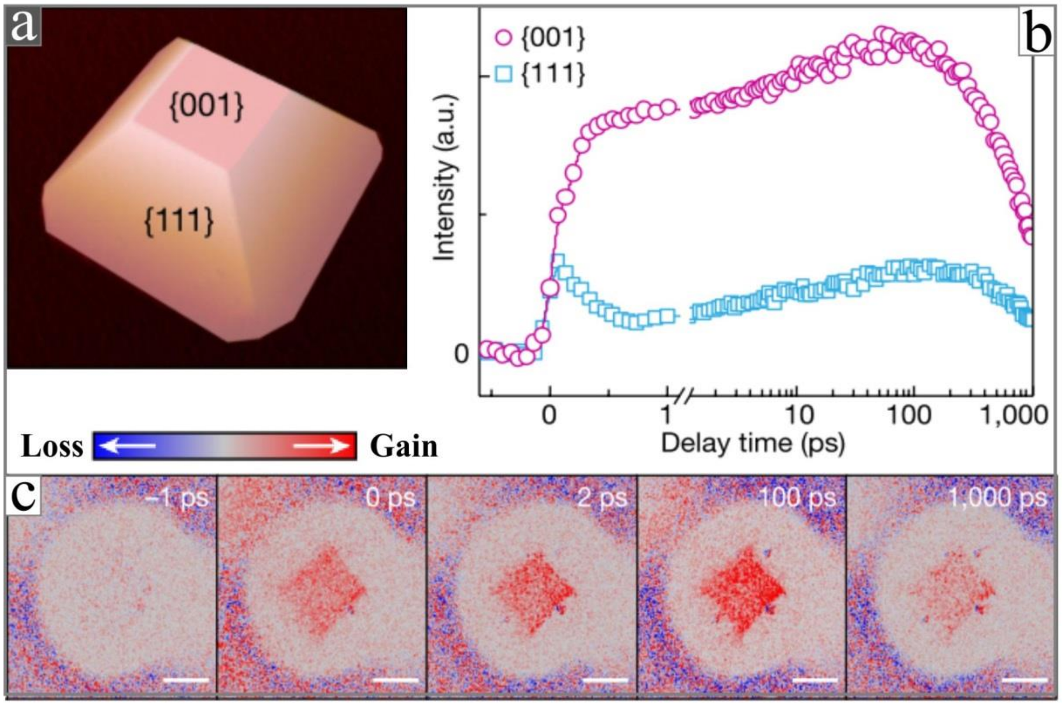

Figure 5: (a) Facet arrangement of an ideal Cu_2O crystallite as used in the studies described in Ref. [40]. (b) Time evolution of the energy-integrated photoelectron intensity from two Cu_2O cluster facets as measured with a transient PEEM. The data reveals a net electron flow from (111) to (100) facets. (c) Visualization of the photon-induced electron exchange between these two facets as a function of the pump–probe delay. The scale bar is always 2 µm.

From a thermal-catalysis point of view, copper oxide nanoparticles are mostly relevant for CO oxidation,[45] steam reforming of methanol,[46] methanol synthesis from CO_2,[47,48] and C−S cross-coupling reactions.[49] Their photocatalytic performance is typically explored in three model reactions, i.e., the hydrogen evolution process,[50,51] the CO_2 reduction to methanol,[52] and the photo-induced degradation of organic molecules.[53] Insufficient knowledge on the termination of the active Cu-O phase hereby turned out to be the main bottleneck for interpretating the catalytic data, a situation that demands for a surface-science specific view onto copper oxides.

Besides the nanoparticle route, bulk crystals and thin films have thus been utilized to explore the surface characteristics of Cu-O materials. The respective experiments take advantage of the large arsenal of surface-science methods to gain comprehensive and detailed information on the atomic structure, chemical composition and electronic properties of model-type oxide surfaces. Moreover, the well-defined geometry of low-index planes enables a direct correlation between experiment and DFT calculations, generating mechanistic insights into the structure-functionality relationship of copper oxides.

Such fundamental studies on the atomic configuration, the electronic and the optical behavior of well-defined copper oxide surfaces now stand in the focus of this review article. It combines state-of-the-art experimental and theoretical work, dealing mostly with the surface properties of Cu_2O. Moreover, it aims at clearing out several misconceptions on the thermodynamically preferred surface configuration, the defect landscape and the catalytically active sites of those surfaces. Our article is structured as follows. Chapter 2 deals with experimental approaches towards clean and well-defined Cu_2O surfaces, either by growing thin films on suitable metal supports or preparing respective cuts of a bulk crystal. As thin films are typically formed by copper oxidation, we emphasize kinetic and thermodynamic hindrances in the oxidation process. Such barriers often lead to self-terminated oxide growth, whereby the resulting ultrathin layers may be fundamentally different from the respective bulk surfaces. In fact, various thin-film phenomena related to Cu_2O actually arise from strong metal-oxide interactions and have been erroneously associated to copper oxide. To avoid such misinterpretations in future, we present a set of indicators that allow safe discrimination between ultrathin oxide precursors and genuine bulk-derived Cu_2O surfaces.

Chapter 3 provides a comprehensive introduction into low-index Cu_2O surfaces, as derived from the (111), (110) and (100) planes. The building principles of CuO surfaces are not explored at this point, as reliable experimental and theoretical insights into this phase are still missing. In chapter 4, we discuss the unique electronic and optical properties, especially of the Cu_2O(111) surface. The chapter aims at connecting mean-field properties as measured by non-local methods with the behavior explored by scanning probe microscopy, putting special emphasis on the role of surface defects on the local electronic, optical and adsorption response. The final chapter summarizes the state-of-the art knowledge on Cu_2O doping, highlighting the discrepancy between the theoretically anticipated behavior and phenomena that have actually been confirmed by experiment. A short summary recapitulates the most relevant properties of Cu-O surfaces and addresses questions and problems that presently hamper their technical utilization.

2. Copper oxidation

2.1. Introduction

Copper oxidation is one of the most intensively studied oxidation reaction and stands in the focus of research already for many decades.[54,55] This huge interest is based on several advantageous features of the reaction. First, there is the relatively low heat of oxidation (-170 kJ/mol for $2Cu + ½O_2 \rightarrow Cu_2O$) that enables a detailed examination of the process at accessible time and temperature scales. Second, the reaction is known for its smooth progression that lacks large spatial dependencies. And last, it results in a small number of reaction products, essentially limited to Cu_2O and CuO. As a consequence, Cu oxidation reactions have been intensively examined with various experimental techniques, especially with micro-gravimetry (probing the weight increase upon oxidation),[56] optical and THz spectroscopy,[57.58] ellipsometry,[59,60] and conventional photoelectron-spectroscopy (XPS) that is particularly surface sensitive.[61] Apart from these in-situ approaches, snapshots of the sample morphology upon oxidation were revealed by electron microscopy and diffraction.[62,63] The so obtained experimental results were used to develop, confirm and refine model concepts for oxidation reactions in general and for Cu oxidation in particular.[64]

The most fundamental oxidation theory was devised by Tammann, Pilling and Bedworth already hundred years ago.[65,66] It treats oxidation processes as the diffusion of neutral particles, following the concentration gradient between the metal-oxide and the oxide-gas interface. Assuming a concentration-independent diffusion coefficient, the oxide thickness d grows with the square root of time, according to $d(t)\sim\sqrt{t}$. The Wagner theory, on the other hand, relates oxide formation to the diffusion of charged particles, which brings the electric field, the mobility and chemical potential of cations and anions into play.[67] At the assumption of locally constant concentration gradients, the model can be simplified again to a square-root dependence between film thickness and oxidation time, $d(t)\sim\sqrt{t}$.[55] In the limit of ultrathin oxide films, the Cabrera-Mott theory delivers the most reliable description of metal oxidation processes.[68] Its starting point is a spontaneous electron transfer from the metal-oxide to the oxide-gas interface, stimulated by a step in the vacuum potential. The electron exchange produces metal cations and oxygen anions at interface and surface, and leads to the development of an electric field across the oxide layer. The latter provides an electrostatic stimulus for the hopping motion of ions, being the prerequisite for the oxidation reaction. This mechanism gives rise to an inverse logarithmic relation between oxide thickness and time $d(t)^{-1}\sim A-B\cdot\ln(t)$, with A and B being parameters.[55] As tunneling is the major electron-transfer mechanism through the emerging oxide film, the Cabrera-Mott theory is valid only for layers thinner than 3-5 nm. Several attempts have been made to extend its validity by replacing electron tunneling with more long-ranged transport schemes, such as thermionic emission.[69] Moreover, direct logarithmic laws, $d(t)\sim\ln(A+t)$, can be obtained when treating cationic and anionic diffusion with position-dependent activation barriers inside the emerging oxide film.[70]

2.2. Low-pressure oxidation of copper

In this review, we concentrate on surface-science relevant aspects of copper oxidation that are compatible with vacuum-based experiments, hence in line with the Cabrera-Mott theory. A careful look at low-pressure Cu oxidation is required here, as many studies that presumably address the surface properties of copper oxide were actually performed on ultrathin oxide precursors that neither mimic the structure nor the electronic properties of the genuine oxide material. The scientific history of these monolayer-thick oxide films started with oxidation experiments of Cu(111) performed at 10^{-6} mbar O_2 pressure.[71,72] Two distinct ultrathin precursor oxides were revealed by electron diffraction and scanning tunneling microscopy (STM) in those early experiments, the so called ‘29’ and ‘44’ structures, labelled according to the size of their unit cells with respect to the one of Cu(111) (Fig. 6). Given the mere dimension of those cells, a reliable structural analysis of the precursor oxides turned out to be difficult and is still subject of research.[73] Despite remaining ambiguities, Cu-O six-membered rings could be identified as the fundamental building blocks of both ad-layers, in line with the main structural motif of the bulk-cut Cu_2O(111) surface. The six-membered rings of the ‘29’ structure are hereby subject to pronounced distortions, being required to achieve registry with the Cu(111) surface, and contain an oxygen ion in the center.[74] The level of ring-distortion is reduced in the expanded ‘44’ configuration that already resembles a Cu_3O_2 honeycomb structure with O ions located at the corners of the oxide rings.[73] The growth characteristics, defect properties and electronic structure of the two oxide precursors have been investigated in numerous follow-up studies, some of them highlighting feigned similarities to bulk-type Cu_2O.[75,76,77] However, neither the atomic structure nor key electronic aspects of the two oxide films, e.g. a real band gap, reflect respective bulk properties, which render the ‘29’ and ‘44’ layers an unsuitable model system for Cu_2O.

The ultrathin oxide precursors on Cu(111) gained nonetheless some relevance on their own, because of an exceptionally high reactivity in the low-temperature CO and H_2 oxidation.[78] In fact, exposing the ‘44’ layer to ambient-pressure CO triggers an immediate reduction of the oxide precursor to metallic copper even at room temperature. Even the reaction fronts associated with this reduction process could be visualized in real space and real time, using time-resolved STM measurements.[79]

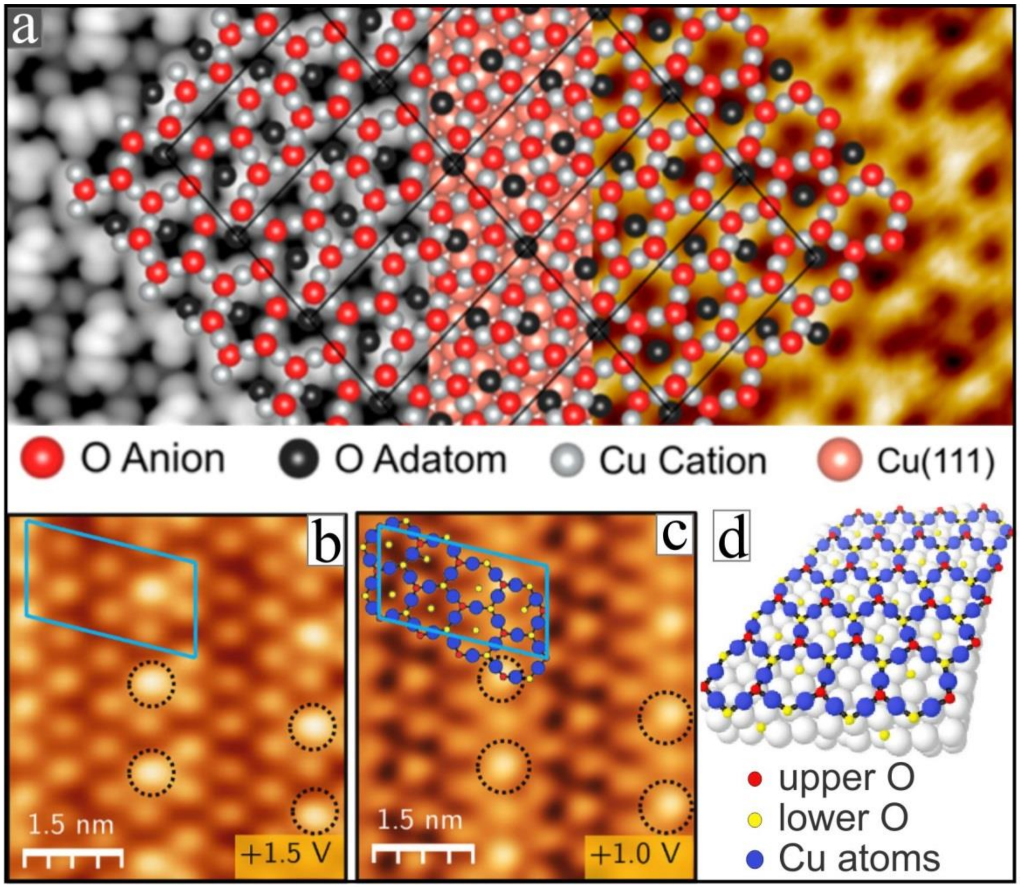

Figure 6: (a) Simulated STM image, atomic structure model and experimental STM data ($U_B = -0.5$ V, 3.5 × 3.5 nm^2) of the '29' Cu-O ad-layer prepared by Cu(111) oxidation.[74] (b) Experimental and (c) simulated STM image as well as (d) structure model of the '44' Cu-O ad-layer on Cu(111).[73]

The self-terminated growth of ultrathin oxide precursors on Cu(111), observed in a wide range of oxygen pressures and temperatures, is usually linked to the interfacial lattice mismatch between metallic and oxidized copper, as additionally reflected in the large unit cells of the '29' and '44' films. Consequently, substrates with a more favorable lattice match with respect to bulk $Cu_2O(111)$ have been tested to synthesize oxide films that are not affected by growth limitations. An obvious first choice was Au(111), whose lattice parameter is 13% larger than that of Cu(111) and within 4% of the $Cu_2O(111)$ lattice constant.[80,81] Reactive Cu deposition in 1×10^{-6} mbar O_2 indeed results in several well-ordered Cu_3O_2 structures, depending on the applied post-annealing conditions (Fig. 7).[82] All films feature a (2×2) superstructure with respect to Au(111), confirming the idea of reduced interfacial lattice strain. Similar to the '44' layer on Cu(111), main building blocks are Cu-O six-membered rings arranged in a honeycomb configuration. Hereby, threefold-coordinated O ions, alternately bound to Au top and fcc-hollow sites, interconnect to Cu ions located in hcp-hollow positions (Fig. 7c). The O-ions assemble in two surface-parallel planes located 0.4 Å below and 0.9 Å above the Cu layer, whereby the upper plane governs the contrast in the STM images. The residual lattice mismatch between a freestanding Cu_3O_2 honeycomb layer and Au(111) gets released via a well-ordered dislocation network, the appearance of which changes with annealing temperature. Whereas a triangular domain pattern with 8 nm edge length is observed in low-temperature films (600 K), it evolves to a zig-zag and a stripe-pattern upon annealing to 650 and 750 K, respectively (Fig. 7d-f). In a combined STM and DFT study, even the atomic structure of these dislocation lines could be analyzed, giving insight into the underling strain-relaxation mechanism.[82] Very similar results have been obtained in another Cu-O growth study on Au(111),[81] which focussed mainly on the competition between armchair and zizag edges terminating the Cu_3O_2 islands.

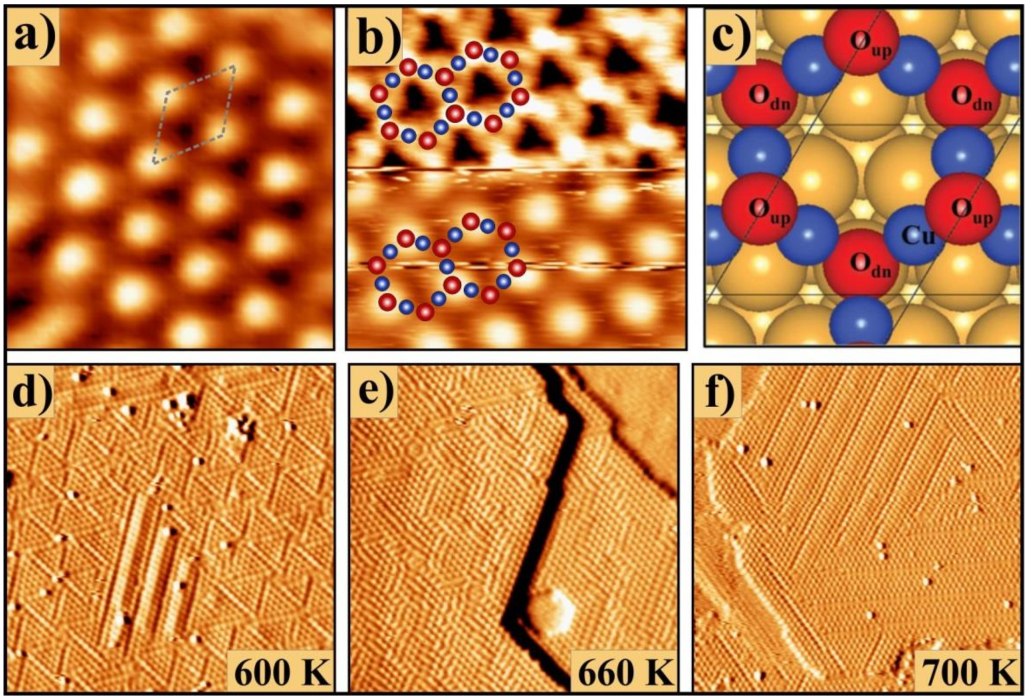

Figure 7: (a) STM image of the honeycomb Cu_3O_2 monolayer film on Au(111) (0.5 V, 3×3 nm^2). A tip change in (b) makes not only the (2×2) lattice of the O_{up} ions but both oxygen species visible. (c) Structure model of the Au-supported Cu_3O_2 monolayer. (d-f) STM images of differently annealed Cu_3O_2 honeycomb films, showing the evolution of the strain relaxation patterns from (d) triangular, (e) zig-zag to (f) Au[110]-oriented stripe networks (10×10 nm^2).[82]

A lattice parameter of 2.77 Å combined with a low oxygen affinity makes Pt(111) a suitable support to grow Cu-O thin films as well. Surprisingly, the low-temperature oxide layer displays identical properties to the oxide precursors formed on Cu(111), despite the substantially larger lattice parameter of Pt(111).[83] In fact, the well-known ‘29’ structure is found for films annealed to 550 K, and evolves to the ‘44’ configuration upon rising the temperature to 600 K (Fig. 8). While this observation comes unexpected at first glance, it gives additional evidence for the self-terminated growth of Cu-O films in vacuum-compatible preparation schemes. Similar to the findings on Au(111) and Cu(111), the precursor oxide only thickens to monolayer height on Pt(111), which is enough to reduce the surface energy of the metal substrate without building up interfacial lattice strain. In contrast to Au(111), however, Cu atoms that are not incorporated into the surface oxide accumulate at the Pt/oxide interface, where they generate an identical growth environment as encountered on Cu(111).[71] A similar behavior is not observed on the gold substrate that shows a high tendency for alloy formation with the excess copper.[82,84] As this alloy rapidly dissolves into the gold crystal, the initial Au(111) lattice parameter remains nearly unchanged and the Cu-O precursor oxide develops the strain-reduced (2×2) configuration in that case.

For the Cu-O growth experiments on Pt(111), the monolayer nature of the precursor oxide was also verified by XPS measurements.[83] The spectra demonstrate that most of the copper indeed remains metallic and accumulates in the form of Cu^0 at the Pt(111)/oxide interface. Only a small O *1s* peak reflects the Cu-O monolayer at the surface. The data confirm that growth of thick and bulk-like Cu_2O films is inhibited even on lattice-matched substrates, such as Au(111) and Pt(111), independent of the amount of deposited Cu, of the oxidation temperature and the O_2 pressure as long as it stays below 10^{-3} mbar. Based on these findings, a new mechanism for the self-terminated growth of Cu-O films was proposed.[83,85] Apparently, neither the interfacial lattice mismatch nor the moderate Cu oxidation enthalpy, being similar to the one of Ni for example, is responsible for the inhibited thickening of the precursor oxide. Instead, the unique porous structure of the oxide ad-layer hampers a continuous oxidation process, as incoming Cu atoms readily penetrate the Cu-O six rings and accumulated at the interface, where the access to gas-phase oxygen is blocked. Successful preparation of bulk-type Cu_2O films thus requires oxygen pressures that are sufficiently high to pull the Cu atoms back to the surface in a Cabrera-Mott type scheme.[68] The correctness of this assumption will be proven in chapter 2.3, demonstrating successful growth of bulk Cu_2O in a high-pressure O_2 atmosphere.

Although formation of bulk-type Cu_2O turned out to be unsuccessful, reactive Cu deposition on Pt(111) nicely illustrates the growth complexity of metal-oxide thin films, as depicted in Fig 8.[83] Below 650 K deposition temperature, the experiments unraveled the ‘29’and ‘44’ Cu-O precursor oxides due to Cu accumulation at the metal-oxide interface, as discussed before. The situation changes drastically upon sample annealing above 700 K, when Cu-Pt intermixing sets in and the lattice parameter of the substrate gradually increases from 2.55 Å for Cu(111) to 2.61 Å for a $Cu_3Pt(111)$ alloy.[86] The associated built-up of interfacial lattice strain triggers an order-disorder transition in the Cu-O precursor oxide that becomes manifest by rearranging the Cu-O six-membered rings into heavily distorted five-, six- and seven-membered rings (Fig. 8c). At the end of the phase transition, the surface oxide has become amorphous and any registry to the substrate is lost.

Surprisingly, further annealing to 750 K stimulates a second phase transition in the oxide ad-layer, whereby the Cu-O network breaks apart into localized Cu_3O building blocks that perfectly arrange in a $(2\sqrt{3}\times2\sqrt{3})$ superstructure (Fig. 8 d,e).[83] The discrete nature of these units removes the lattice strain and renders the ad-pattern stable up to 900 K. Moreover, the ad-layer can be re-oxidized in 5×10^{-7} mbar O_2, whereby Cu from the Cu_3Pt alloy is pulled out of the metal support and reintegrates into a compact and closed-packed Cu-O network (Fig. 8f). Not unexpected, this process does not restore the original, highly strained honeycomb lattice, but three adjacent rings merge to a triangular pore with an O defect in the center. This new, more open Cu-O network represents an effective means to cope with the residual lattice strain at the interface.[87] The amorphization of the Cu-O precursor oxide upon high-temperature annealing has been reported for Cu(111) substrates, too.[88] Moreover, the unique ability of strained Cu-O networks on Pt(111) to release oxygen in a CO oxidation reaction has been addressed in the literature.[89] It should be noted in this regard that the high reaction rate reported in that study actually arises from the interplay of an easily reducible precursor oxide and the favorable catalytic properties inherent to Pt(111).

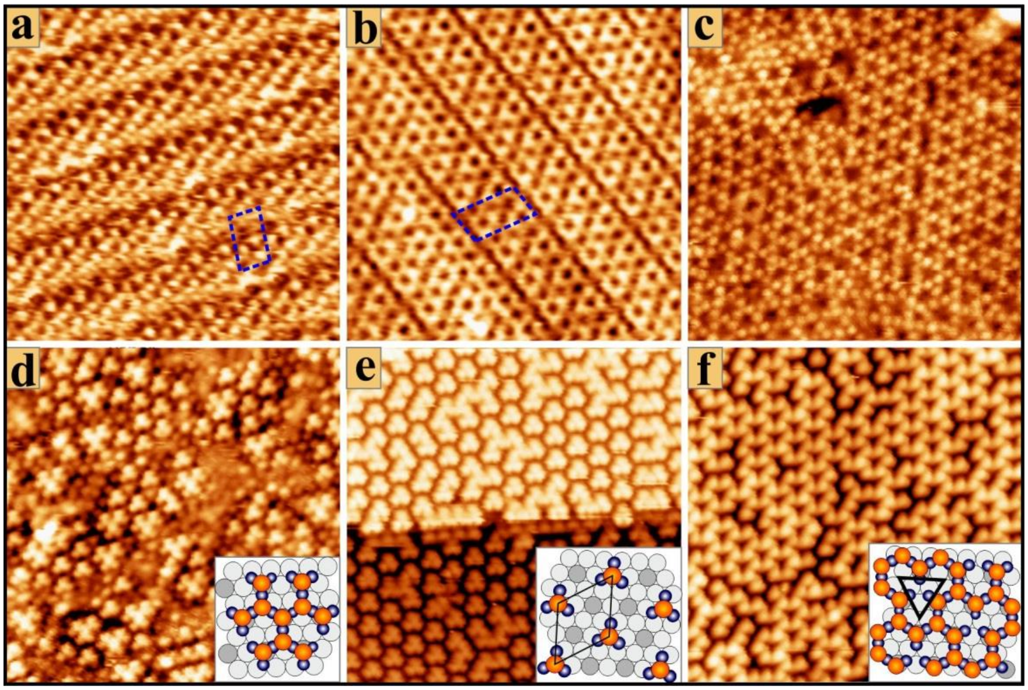

Figure 8: STM image of (a) the '29' and (b) the '44' Cu-O ad-layer on Pt(111). The oxide precursors match the ones grown on Cu(111), as excess copper accumulates at the metal-oxide interface. (c) Strain-induced amorphization of the oxide film due to formation of 5-, 6- and 7-membered rings. The effect is driven by alloy formation of interfacial Cu with the Pt substrate at higher temperature. All images are 10 × 10 nm^2 in size. (d) Decay of the compact oxide film at even higher temperature into isolated oxide units with star-like and (e) Cu_3O trimer-type configuration (9 × 9 nm^2). The latter structure can be re-oxidized into an open Cu-O network (f). Characteristic building blocks of the different layers are depicted in the insets (Cu_{ox}: blue, O: orange, Pt: grey, Cu_{Pt}: dark grey).[83]

The various examples discussed in this paragraph aim at demonstrating that low-pressure oxidation of Cu does not allow to prepare thick copper oxide films. In contrast to many reports in the literature, vacuum-compatible preparation schemes are neither suited to prepare Cu_2O or CuO bulk-type films nor to analyze their specific surface properties. In the next section, we will therefore present how bulk-compatible oxide films of high quality can be fabricated with common surface-science preparation techniques.

2.3. High-pressure copper oxidation

The oxidation of copper has evolved to a case study to explore the thermodynamics and kinetics of metal-oxygen interactions.[90,91] Early Cu-oxidation experiments date back already to the 1950s and revealed an inverse logarithmic growth rate for Cu_2O in the low-temperature limit and at ambient O_2 pressure.[92] Over the years, this inverse logarithmic oxidation rate could be reproduced in many studies,[93,94] including recent XPS measurements with particularly high surface sensitivity.[61,95] All these experiments impressively validated the original idea of Cabrera and Mott, connecting metal oxidation in the thin-film limit to an emerging surface electric field that drives the reaction.[68] The probably most comprehensive experimental series was performed by Fujita et al. via ellipsometry.[63] The authors observed a crossover from an inverse logarithmic to a cubic and finally a parabolic growth rate for oxide thicknesses below 5 nm, below 50 nm and above 50 nm, respectively. The thin-film oxidation thus follows the Cabrera-Mott scheme,[68] while the universal parabolic law devised in Wagner's theory prevails in the limit of thick layers.[67] From an Arrhenius analysis, the main activation energies related to Cu oxidation were determined to ~30 and ~100 kJ/mol and correlated to surface and grain-boundary diffusion of copper in the limit of thin and thick films, respectively. The importance of Cu transport through grain-boundaries was further corroborated by Zhu et al., who reported activation energies of ~40 kJ/mol, being much too low for Cu diffusion in a compact bulk-type environment.[56]

In order to link the surface-science approach to copper oxides, as discussed in the previous chapter, to conventional oxidation studies, designated experiments are presented here that interrogate at what temperature and O_2 pressure the growth transition from ultrathin Cu-O precursor oxides to truly bulk-type films occurs. The measurements employed UV/Vis spectroscopy to probe the time-dependent change in optical transmittance when exposing a pre-deposited Cu film to O_2 pressures of up to 1 bar and temperatures of up to 800 K.[96,97] Apart from the actual oxidation, all experimental steps including sample preparation and characterization were carried out in an UHV environment to avoid parasitic effects. The robustness of such an optical approach enabled the in-situ monitoring of oxidation processes even at harsh chemical conditions that are unsuitable for classical surface-science techniques, such as XPS.

An exemplary series of transmission spectra, acquired during the oxidation of 50 nm Cu at 420 K and 100 mbar O_2, is depicted in Fig. 9a.[97] The increasing transmittance due to gradual conversion of metallic Cu to dielectric Cu_2O is readily observed (blue to red spectra). By fitting the experimental data to existing oxidation models, direct insight into the oxidation mechanism could be obtained. The optical simulations were carried out with the transfer-matrix method applied either to Cu_2O-Cu bilayer or Cu_2O-mixed Cu/Cu_2O-Cu trilayer models (Fig. 9b).[98] While the former model assumes a planar metal-oxide reaction front, the latter accounts for an inhomogeneous interface between Cu and Cu_2O components. Hereby, two arrangements of oxide particles in the Cu host were tested, a random and a chain-like distribution, as accounted for in the Maxwell-Garnett and the Brüggeman mean-field schemes, respectively.[99,100] Only the latter enabled reliable fitting of all spectra in a transmission series with one set of parameters, demonstrating that Cu oxidation does not proceed homogenously but along distinct reaction paths (Fig. 9c). Accompanying TEM experiments clearly confirmed this interpretation and provided direct evidence that polycrystalline Cu films oxidize along grain boundaries in the material.[97]

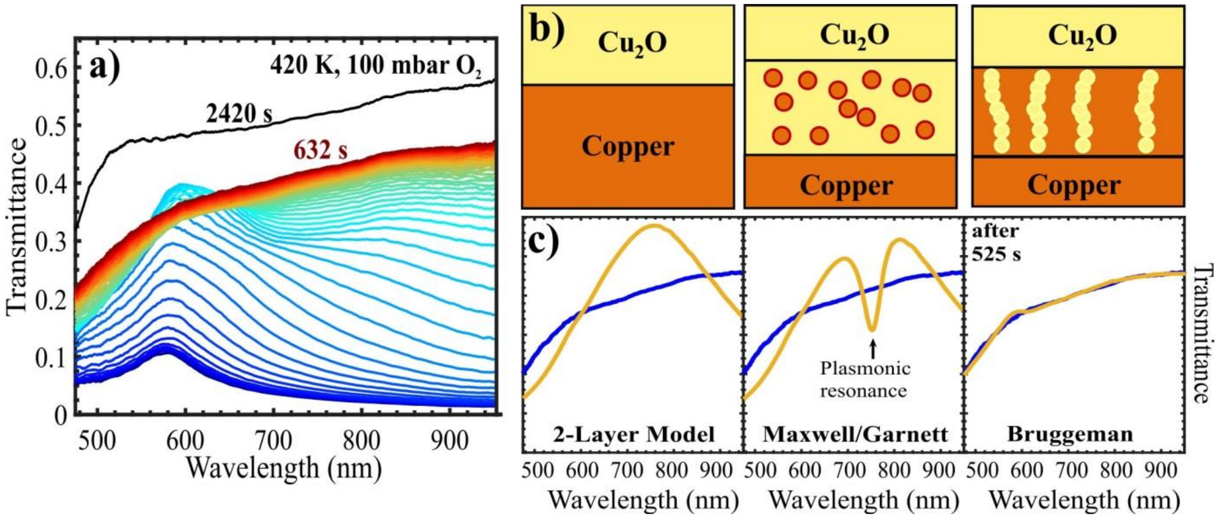

Figure 9: (a) Series of optical transmission spectra acquired during the oxidation of 50 nm polycrystalline copper at 420 K and 100 mbar O_2. The spectra are color-coded according to their chronological order (blue to red), the top spectrum represents the final state of the sample after oxidation. (b) Two and three-layer models to simulate optical transmission spectra. The mixed layer in the center is described either with the Maxwell-Garnett or the Bruggeman approach, focusing on plasmonic inclusions and percolated particle chains, respectively. (c) Fit of the experimental spectrum taken 525 s after starting the oxidation to either a two-layer model or three-layer models described with the Maxwell-Garnett or Bruggeman scheme. Only the latter yields good agreement between theory and experiment.[97]

Having established a Cu oxidation model, the kinetics of the process was analyzed in a wide range of O_2 pressures and temperatures, as shown by the corresponding oxide growth curves in Fig. 10. Distinct kinks in all curves mark the point in time, when the reaction front reaches the backside of the sample and the process slows down (see arrows). By fitting the growth rates to a temperature-dependent Arrhenius behavior, the activation energy associated to Cu oxidation was determined. Over a wide range of O_2 pressures and Cu thicknesses, a barrier height of 40 kJ/mol was determined, a value that agrees well with theoretical diffusion energies of Cu atoms along grain boundaries (Fig.10, inset).[56,101] Conversely, bulk diffusion through a compact oxide lattice comes along with barriers above 100 kJ/mol, emphasizing again the pivotal role of defects and boundaries in realistic oxidation processes.[63] It is interesting to note that Cu oxidation is entirely controlled by the high mobility of Cu ions and their transport towards the reaction zone. Oxygen diffusion, on the other hand, requires much higher activation energies and consequently plays no role for the kinetics of oxidation. The importance of Cu diffusion has been impressively demonstrated in numerous oxidation studies on Cu nanoparticles.[102,103] In the course of such reactions, oxide material preferentially accumulates at the surface while a hole develops in the particle center. The resulting formation of hollow structures is commonly referred to as the Kirkendall effect and provides direct evidence for the dominance of cationic over anionic transport during copper oxidation.

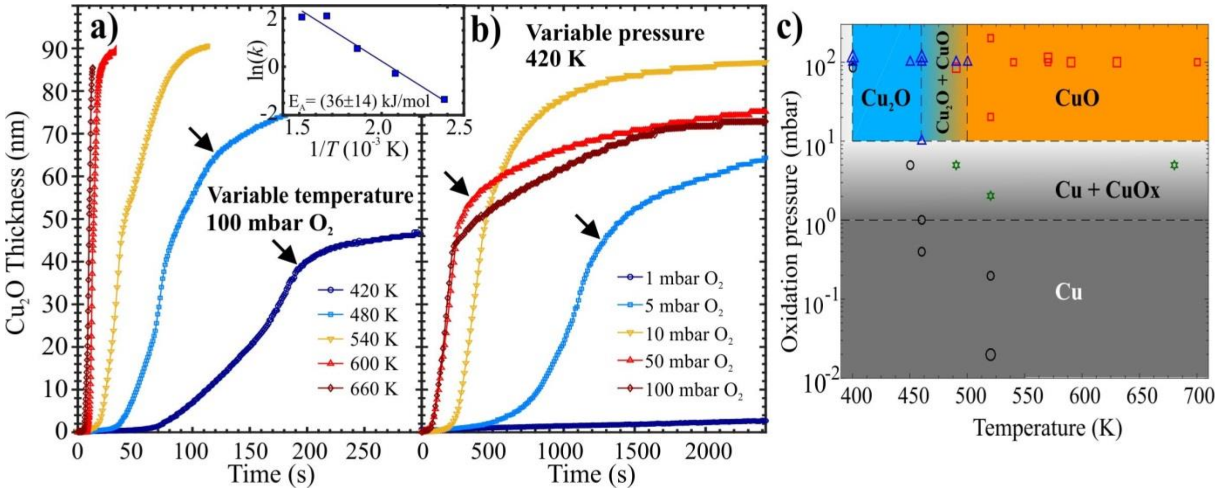

Figure 10: Cu_2O growth curves measured as a function of (a) temperature (p_{ox} = 100 mbar) and (b) O_2 pressure (T = 420 K). The inset shows an Arrhenius plot of temperature-dependent oxidation rates and yields the activation energy of the oxidation process. (c) Formation diagram of Cu oxides, as derived from the growth studies presented in Figs. 9 and 10. Black, blue and red symbols stand for predominately bare Cu, Cu_2O and CuO phases, respectively. Stability regions of the respective phases are depicted in matching colors; coexistence regions are shown with color gradients.[96]

Direct evidence for a reaction scheme that relies on Cu transport along grain boundaries was obtained from oxidation studies performed on nano-crystalline films with variable grain sizes.[104] The respective samples were fabricated by Cu deposition at increasing temperature, making use of Ostwald ripening processes to change the crystalline texture. As expected, a high oxidation speed was observed for Cu films grown at low-temperature, given their small average grain size, but gradually decreased with rising annealing temperature. For high-temperature films prepared at 700 K, only incomplete oxidation was observed as the large, defect-free Cu grains could not be converted into Cu_2O fully within the time span of the experiment. The reaction rates deduced for differently annealed Cu films showed a nearly linear dependence on the total perimeter length of Cu grains, as measured with STM prior to oxidation. This correlation further corroborated the pivotal role of defect-mediated diffusion in Cu oxidation processes.

With increasing temperature, not only the Cu to Cu_2O oxidation, but also the Cu_2O to CuO phase transition was observed.[105] As CuO exhibits deviating dielectric properties, the two oxides are readily distinguished in transmission spectra (Fig. 11a). Moreover, a Tauc analysis of the data revealed the evolution of the oxide band gap during oxidation (Fig. 11b). The phase change from cuprous to cupric oxides sets in at 480 K and accelerates with increasing temperature (Fig. 11c). Fitting the optical data with the transfer-matrix method indicates that the Cu_2O oxidation proceeds along a flat and homogenous reaction front,[105] and not along defect-mediated pathways as observed for Cu oxidation before.[97] The difference is readily rationalized with the nano-crystalline or even amorphous nature of the Cu_2O starting material. The higher oxidation temperature towards CuO, on the other hanfd, reflects the large activation barrier that needs to be overcome to change the Cu oxidation state from 1+ to 2+ and to squeeze extra oxygen into the already dense Cu_2O lattice. The effect was quantified with an Arrhenius analysis again, plotting the logarithmic CuO growth rates as function of the inverse temperature. As expected, the analysis yields a two times larger activation energy for CuO formation with respect to Cu_2O (79 versus 36 kJ/mol).[105]

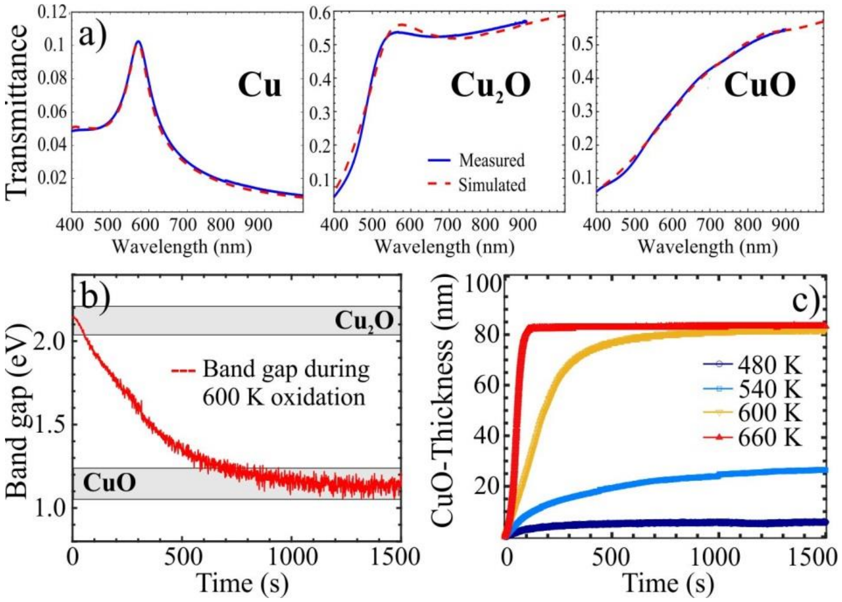

Figure 11: (a) Experimental and simulated transmission spectra of pristine Cu (thickness 50 nm), Cu_2O and CuO films. (b) Time evolution of the gap size, reflecting changes in the Cu_2O/CuO ratio during the oxidation process. (c) CuO growth curves measured at the indicated temperatures (p_{O2} = 100 mbar).

The information gathered in various high-pressure Cu oxidation experiments was finally used to establish a copper-oxide formation diagram, covering a wide pressure and temperature range (Fig. 10c).[96] Its key message is that Cu oxidation beyond monolayer thickness is possible only for O_2 pressures beyond 10 mbar. The associated pressure-dependent growth obstacle was identified in the effective Cu diffusion through the emerging Cu-O precursor oxide, separating the Cu metal from the gas-phase oxygen. Deep Cu oxidation only sets in when outward diffusion of Cu gets activated in a Cabrera-Mott-type scheme at high oxygen chemical potentials.[91,103] The growth temperature, on the other hand, primarily controls whether Cu_2O or CuO evolves in the oxidation process. While formation of phase-clean Cu_2O is highly favourable at oxidation temperatures below 450 K, CuO becomes the dominant phase above 500 K. In the intermediate temperature window, mixed oxidation states are stabilized, such as paramelaconite Cu_4O_3, although a detailed exploration of this transition range is still pending.

After this throrough discussion of Cu oxidation mechanisms, we take a closer look on the structural properties of low-index Cu-O surfaces in the next chapter. For the Cu_2O phase, we can resort to experimental results, acquired either on polished single crystals or oxide films grown on noble metal (111) surfaces, as well as to various DFT calculations. For CuO, mostly theoretical models are available, that could not be confirmed by high resolution diffraction and microscopy experiments so far. The available knowledge is therefore too premature to be compiled in this review article.

3. **Copper oxide surfaces**

The surface-science era of cuprous oxide started already in the 1990's with the seminal experiments of Cox and co-workers performed on Cu_2O single crystals.[106] These early diffraction and XPS studies identified several reconstructions for both, the (111) and (100) surface that stimulated a whole cascade of DFT calculations. However, reliable atomic structure models of the thermodynamically preferred $Cu_2O(100)$ and (111) reconstructions could only be obtained 25 years later by combining high-resolution STM data of thin-film and bulk oxides with state-of-the-art DFT calculations. After a general introduction into the surface properties of Cu_2O, we will present the currently most reliable structure models for its (111) and (100) surface, whereas our understanding of the (110) plane remains fragmented at this point.

3.1. Introduction

To provide first insights into the nature of low-index (100), (110) and (111) planes of Cu_2O, the respective bulk-cuts of the oxide lattice are depicted in Fig. 12. Along (100), pure copper and oxygen layers alternate (…/2Cu/O/…), having a ±2 formal charge per (1×1) surface unit cell. Along the (110) direction, the alternation comprises mixed layers composed of 2Cu and 2Cu+2O, again with a total of ±2 formal charges. Along (111), finally, the stacking is composed of neutral $O/Cu_4/O$ trilayers. The number of oxygen-cation bonds cut upon surface formation is usually considered to be a good indicator of its relative stability. For the three orientations, two Cu-O bonds are cut per unit cell at both the (100) and (110) surface, while only a single bond gets disrupted between two subsequent trilayers with (111) orientation. Considering the associated surface-cell areas (a^2, $a^2\sqrt{2}$ and $a^2\sqrt{3}$ for (100), (110) and (111), respectively, with a the bulk lattice parameter), the expected surface stability decreases from (111) to (110) and (100), i.e., the bulk-cut (111) surface would be the preferred oxide termination. Apparently, this criterion is insufficient to account for the observations, since the (110) surface is the least represented in Cu_2O nanoparticles.[36,37]

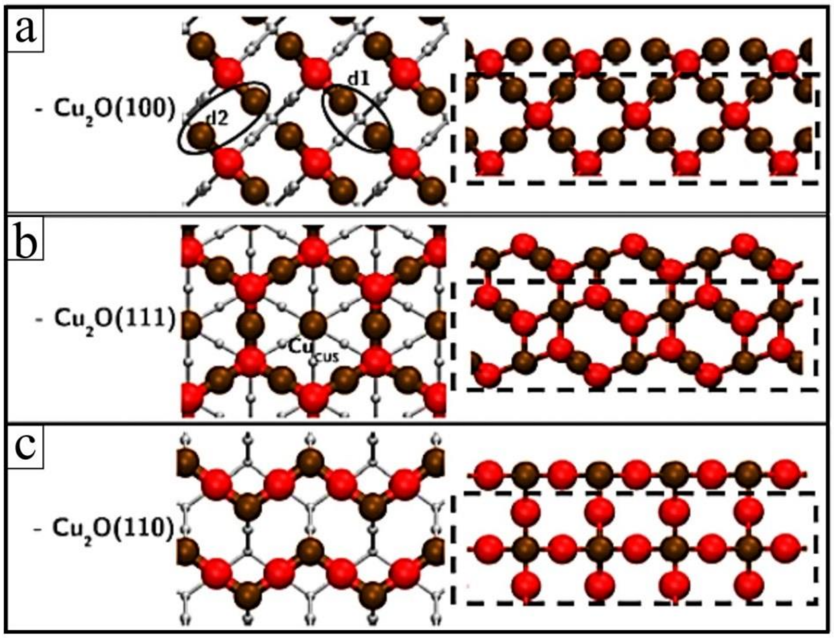

Figure 12: Atomic structure of the low-index bulk-cut surfaces of Cu_2O. Cu and O atoms are represented with dark and red balls, respectively.[2]

Several reasons may be invoked for this discrepancy. The first one is linked to surface polarity effects.[107] The (100) and (110) orientation yield Tasker-type III polar terminations and require ±1 charge compensation per (1x1) unit cell.[108] The (111) orientation belongs to the Tasker-type II category and exhibits a non-polar termination if no O/4Cu/O trilayer is cut, but becomes polar otherwise. The compensating charges to reach electrostatic stability of polar surfaces may be provided by (i) substantial electron redistribution in the surface layers (electronic reconstruction), (ii) spontaneous desorption of surface ions changing the surface stoichiometry (non-stoichiometric reconstruction) or (iii) adsorption of charged species, such as hydroxyl groups from dissociative water adsorption.[107,109] The first mechanism is usually not favorable from an energetic point of view, because it involves an effective electron transfer across the band gap. In particular, in strongly ionic, wide-gap oxides, where charge transfer occurs from valence *O 2p* states to the cation-derived conduction band (CB), the energy costs are prohibitive and the mechanism is never observed. However, in Cu_2O with its moderate gap and Mott-Hubbard character, it may compete with the structural reconstruction and the adsorption mechanisms. At this point, one should distinguish between stoichiometry changes due to missing surface ions, altering the formal surface charge and thus the polarity, and reconstructions due to position changes of the surface ions, which preserve the surface charge and do not alter the polar character. As many erroneous statements are present in the literature, it is useful to recall the interrelation between surface relaxation and surface polarity. Relaxation effects always lower the surface energy compared to bulk-cut configurations and alter the surface dipole moment. However, whatever their amplitude, surface relaxation alone cannot compensate surface polarity. Indeed, the latter is due to a divergence of the macroscopic dipole that can only be healed by additional surface charges but not by finite changes of the surface dipole moment.[110]

The second important parameter controlling the surface stability is the oxygen content. The stability of surfaces with different stoichiometry is typically assessed by comparing their relative Gibbs free energies. Depending on the experimental conditions, i.e., an oxygen-lean or oxygen-rich preparation environment, more Cu-rich or more O-rich terminations may be favored. The associated gain or loss in surface Gibbs energy then competes with other surface-energy contributions, e.g. the costs for bond breaking or polarity stabilization. Indeed, we will see in the following that different surface terminations and/or reconstructions may be observed under different surface preparation conditions.

And last, independent of the dominant polarity compensation mechanism either by electronic reconstruction or stoichiometry changes, the outermost layers have to accommodate excess electrons or holes. A peculiarity of Cu_2O is its Mott-Hubbard character, reflected in the presence of Cu orbitals at both sides of the band gap. The required excess charges thus localize mainly on the Cu atoms, yielding either an increase (excess holes) or decrease (excess electrons) of their oxidation state. In the latter case, formation of Cu dimers with quasi-metallic bonds between the two atoms is revealed on several (100) and (111) terminations, as detailed later.

Before closing this section, some general statements on DFT calculations are useful. From a theory point of view, Cu_2O is a rather complex system. Already a correct treatment of the p-type conduction behavior of the bulk was shown to require an exchange-correlation functional, beyond the Generalized Gradient Approximation (GGA)[6] and even beyond GGA+U, in order to describe the transition between polaronic levels of the split Cu vacancies.[111] A similar conclusion was reached in a G_0W_0 study, aiming at reproducing the direct/inverse optical band gap and the edge positions of Cu_2O.[112] The authors pointed out that the wave functions and energies, which served as inputs to the perturbative G_0W_0 approach, had to be calculated at the hybrid level. They explained this with the unique electronic structure of Cu_2O, i.e., the mixed *s*-*p*-*d* character of its band-edge states, which requires electrons in all orbitals to be treated with exact exchange and not only the *d* states as in the DFT+U approach. Despite these findings, most existing simulations of Cu_2O surfaces are based on either GGA or GGA+U functionals. One purely technical reason is the prohibitive cost of hybrid calculations in the case of large unit cells. The GGA method hereby exaggerates the covalent nature of the Cu-O and Cu-Cu bonds, and therewith largely underestimates the gap width (~0.5 versus 2.15 eV in the experiment) and the costs for electronic reconstructions at polar Cu_2O surfaces. The GGA+U method has similar drawbacks since it is unable to significantly open the band gap (0.5–0.8 eV for U parameters between 2–8 eV). We will see in the following that GGA calculations predict a polar Cu-deficient (111) surface to be more stable than the stoichiometric, non-polar one in the entire stability range of bulk Cu_2O. In contrast, the stoichiometric termination is favored when using hybrid Heyd-Scuseria-Ernzerhof (HSE) functionals over a wide span of oxygen-lean conditions under which bulk Cu_2O is thermodynamically stable.[113]

3.2. The Cu_2O(111) surface

3.2.1 Termination: Theory and experiment

Among all low-index planes of cuprous oxide, the (111) surface plays an exceptional role given its potentially non-polar and thermodynamically stable nature. Not surprisingly, pristine Cu_2O nanocrystals often take octahedral shapes, reflecting the dominance of (111) crystal facets.[34,36] The surface-science exploration of macroscopic Cu_2O(111) planes was initiated by Schulz and Cox on appropriately cut single crystals.[106] Using electron diffraction, they identified two distinct surface terminations, a simple hexagonal (1×1) pattern and a $(\sqrt{3}\times\sqrt{3})R30°$ superstructure. The former was prepared by ion bombardment and subsequent vacuum annealing at 1000 K and did only show associative O_2 adsorption at low temperature. It was therefore assigned to the quasi-ideal, stoichiometric surface (ST-surface, Fig. 13). The $(\sqrt{3}\times\sqrt{3})R30°$ termination, on the other hand, got stabilized after multiple adsorption/desorption cycles, e.g. of propene, whereby the desorption process was suggested to trigger oxygen removal from the surface. The reconstructed surface was consequently associated with an ordered array of oxygen vacancies (ST-O_s with $^1/_3$ O defects per unit cell, Fig. 13), even though ultraviolet photoelectron spectroscopy did not reveal a reduced oxygen content with respect to the stoichiometric (1×1) surface. The concept that the $(\sqrt{3}\times\sqrt{3})R30°$ reconstruction of Cu_2O(111) is due to an oxygen deficiency nonetheless governed the experimental and theoretical studies of the coming years.

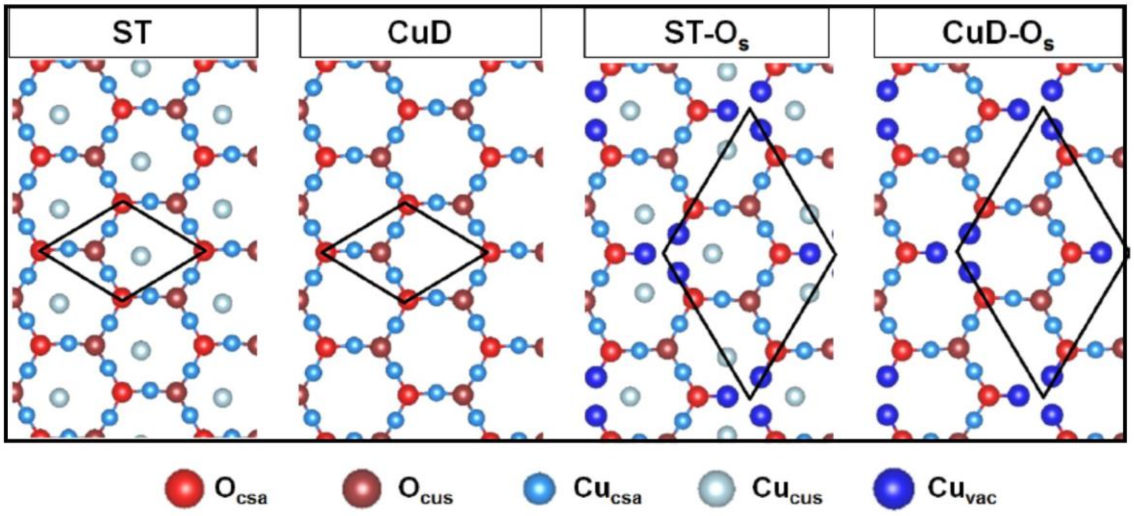

Figure 13: Atomic models of the most studied $Cu_2O(111)$ terminations composed of coordinatively saturated (csa) and unsaturated (cus) ions. **ST**: Stoichiometric (1×1) surface, **CuD**: Cu-deficient (1×1) surface with Cu_{cus} vacancies, **ST-O_s**: $(\sqrt{3}\times\sqrt{3})R30°$ surface with $^1/_3$ of the O ions missing, **CuD-O_s**: $(\sqrt{3}\times\sqrt{3})R30°$ surface with Cu_{cus} and $^1/_3$ O_{cus} vacancies. In the two $(\sqrt{3}\times\sqrt{3})R30°$ configurations, Cu atoms close to the O vacancy (Cu_{vac}) are represented with dark blue balls.[114]

In the following years, elucidation of the surface atomic structure of $Cu_2O(111)$ relied solely on DFT calculations. Starting point was always the non-polar, bulk-cut (111) surface, made of an interwoven network of Cu-O six-membered rings with a coordinatively unsaturated Cu_{cus} ion in the ring center and unsaturated O_{cus} ions in the outermost positions (Fig. 13: ST configuration). In a first comprehensive GGA study, a large number of stoichiometric Cu- and O-rich as well as Cu- and O-depleted $Cu_2O(111)$ terminations was investigated, all of them computed on (1×1) surface unit cells.[115] The thermodynamically favored configuration at O-rich conditions was found to be the Cu-deficient one (CuD surface, Fig. 13), obtained by removing the Cu_{cus} ions from the stoichiometric (111) surface. At O-poor conditions, the lowest energy was realized by a Cu-rich surface, in which additional Cu_{ad} atoms bind to the unsaturated O_{cus} ions of the stoichiometric termination. With the same GGA approach, large relaxation effects were found on the Cu-rich termination, including Cu-Cu dimer formation, intermixing of the outermost layers, and large charge reduction of the surface copper ions.[116] With a DFT+U approach, the Cu-deficient termination (CuD) was predicted the most stable in a wide range of oxygen chemical potentials,[117] although the stoichiometric (1×1) surface was close in energy, especially at O-poor conditions.

However, as both, Cu and O removals give rise to polar surface terminations, the validity of the GGA and DFT+U approaches was questioned and the relative stability of stoichiometric (ST) versus Cu-deficient (CuD) terminations was revisited by means of hybrid calculations.[113] In contrast to the earlier GGA and DFT+U predictions, the CuD termination appeared unfavorable in HSE calculations due to an increased cost of polarity compensation, shifting its stability region towards significantly more O-rich environments (Fig. 14a). As a consequence, the HSE approach produced a qualitatively different surface stability picture, in which the stoichiometric (1×1) termination remains favored over a relatively large span of oxygen-lean conditions at which bulk Cu_2O is thermodynamically stable. This pronounced deviation between GGA and HSE calculations was linked to the different description of the oxide electronic structure in the two approaches. More precisely, the hybrid approach was found to better account for the surface ionization potential and the electron affinity, both largely affecting the costs of polarity compensation via the electronic reconstruction mechanism. The findings emphasize the intrinsic susceptibility of GGA(+U) approaches to artificially over-stabilize polar oxide terminations, which may also concern other Cu_2O surface orientations.[113]

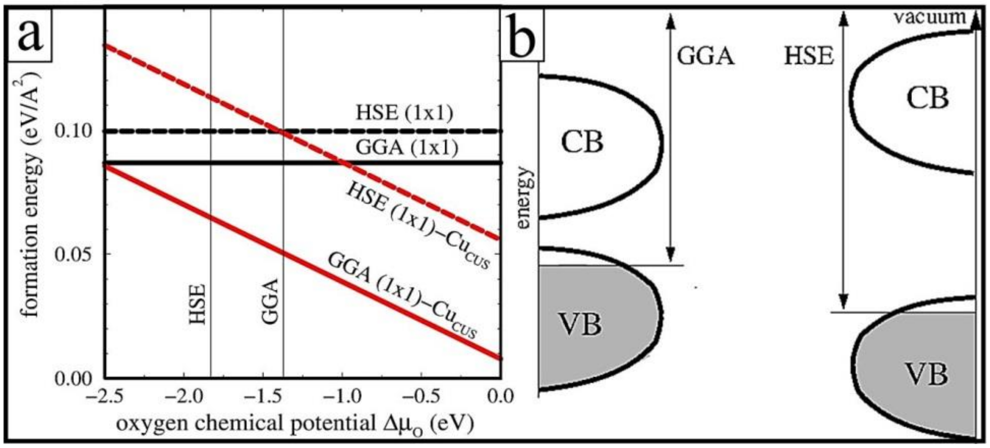

Figure 14: (a) GGA and HSE formation energies of the (1×1)-Cu_2O(111) stoichiometric and Cu-deficient terminations as a function of oxygen chemical potential. The vertical lines demonstrate the stability range of the Cu_2O bulk phase. (b) The schematic Cu_2O band structure displays the improved description of the ionization potential in the HSE approach. Since the ionization potential of Cu_2O is 0.8 eV larger in HSE than GGA calculations, the associated downward shift of the VB with respect to the vacuum level reduces the stability range of the Cu-deficient surface.[113]

Inspired by the early results of Cox et al.,[106] several O-depleted terminations have been tested with GGA/ GGA+U approaches to describe the more complex (√3×√3)R30° reconstruction, e.g. configurations with $^1/_3$ of the O_{cus} ions being removed and the Cu_{cus} ions being either present or absent (ST-O_s and CuD-O_s, Fig. 13).[113,117] All such O-depleted surfaces appeared energetically unfavorable under realistic oxygen conditions and could not compete with the Cu_{cus}-deficient (CuD) and the stoichiometric (ST) termination. Also, the more Cu-rich (√3×√3)R30°-O_{cus}+3Cu_{cus} surface turned out to be less stable than the (1x1)-Cu_{cus} termination.[118] Better insights into the surface reconstruction could only be gained when high-resolution STM measurements of Cu_2O(111) became available. The first atomically resolved images of a Cu_2O(111) crystal surface were provided by Önsten et al.[119] Similarly to the early results of Cox and coworkers,[106] a (1×1) surface was revealed upon annealing in 2×10^{-6} mbar of oxygen, while vacuum annealing resulted in a sharp (√3×√3)R30° superstructure. However, the switch between (1×1) and (√3×√3) R30° termination was not fully reproducible and turned out to depend heavily on the preparation history of the crystal.

The STM signature of the (√3×√3)R30° reconstruction was a regular array of triangular protrusions, coexisting with small (1×1) patches on the oxide surface. Importantly, the maxima showed up with bias-independent size and shape, suggesting a topographic and not an electronic origin. However, the authors kept an interpretation based on O vacancies,[119] although the pronounced bias-dependent appearance of anionic defects was long recognized in the STM community.[120] Atomically-resolved STM images of a Cu_2O(111) single crystal performed by Nilius and coworkers essentially reproduced those early results, revealing large oxide terraces homogeneously covered with a (√3×√3)R30° array of triangular protrusions (Fig. 15 a,b).[121] Only a single study on bulk Cu_2O(111) deviated from the ones described before.[122] Despite similar preparation conditions (sputtering and annealing in 2×10^{-6} mbar O_2),[119,121] the oxide crystal showed a clear (1×1) pattern in LEED and a corresponding close-packed hexagonal lattice in STM (Fig. 15 c). A few triangular protrusions, similar to the ones forming the (√3×√3)R30° pattern, were found to be scattered over the surface. Consequently, the detected termination was assigned to the stoichiometric (1×1) surface with the low-coordinated Cu_{cus} ions being present, and therefore followed the respective HSE prediction.[113] Moreover, the authors successfully identified two characteristic defects in the surface, i.e., Cu_{cus} vacancies showing up as voids in the Cu-O six-membered rings and O_{cus} vacancies that appeared as unique atomic triples due to an inward relaxation of the three adjacent Cu ions (Fig. 15 d).[122]

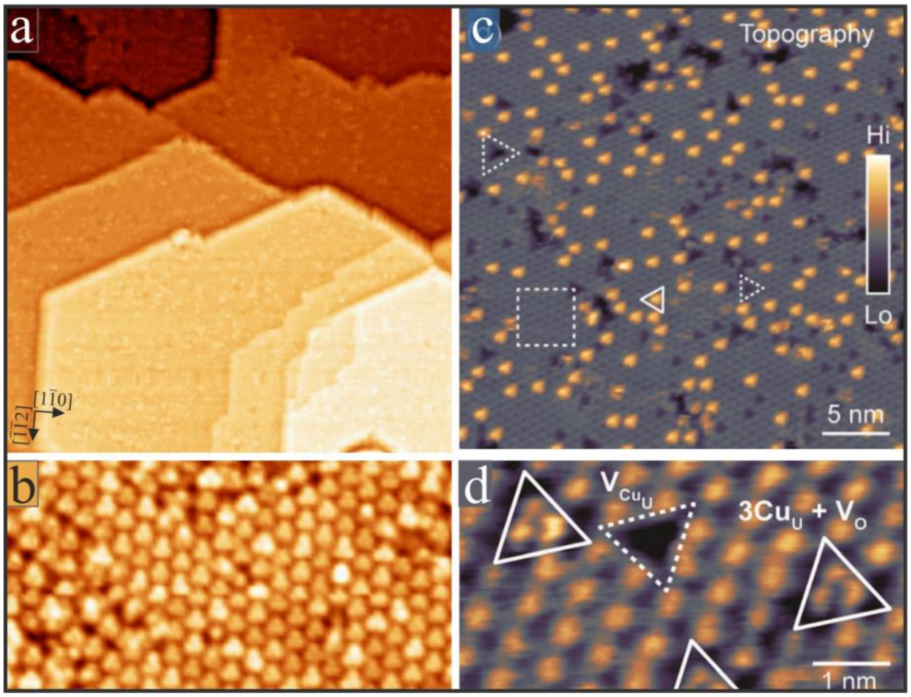

Figure 15: (a) Overview (125×125 nm^2, U_B = 3.8 V) and (b) atomically-resolved STM topographic image of the (√3×√3)R30° reconstructed surface of bulk $Cu_2O(111)$ (20×10 nm^2, -2.3 V). The array of triangular protrusions is readily detected.[121] (c) Overview (35×35 nm^2, -1.5 V) and (d) atomically-resolved STM topographic image of (1×1) terminated $Cu_2O(111)$ (6×3 nm^2, 1.5 V). The up- and down-oriented triangles mark O- and Cu-vacancies in the surface, respectively.[122]

Further insights into the $Cu_2O(111)$ surface termination came from several surface-science studies performed on metal-supported oxide films. To avoid oxidation obstacles, as addressed in chapter 2.2, 10 nm copper was deposited onto sputtered and annealed Au(111)[123] and Pt(111) substrates,[124] oxidized at 50 mbar O_2 at 450 K and post-annealed in 10^{-4} mbar O_2 in those experiments. The bulk-like character of the resulting films was confirmed with XP and Auger spectroscopy, showing identical energy positions and line shapes as observed for bulk samples (Fig. 16). The spectroscopic fingerprints of Cu_2O generally comprise the O *1s* (530.5 eV) and Cu *2p* peaks (933 / 952.8 eV), whereby the latter alone are insufficient to distinguish between Cu^0 or Cu^+ oxidation states. This missing information is provided by Cu L_3VV Auger transitions that emerge at 918.6 (main peak) and 917 eV for metallic Cu and CuO, respectively, but shift to 916 eV for Cu_2O.[124,125,126] In correspondence to bulk crystals, the oxide thin films reproducibly displayed a (√3×√3)R30° superstructure in LEED and a respective array of (√3×√3) protrusions in STM. Moreover, the topographic height of the triangular maxima was precisely determined to 1.5 Å, independent of the STM imaging conditions (Fig. 17). The nano-protrusions were therefore related to structural elevations and not to electronic effects. Despite the high quality of all those experimental studies, the question on the nature and composition of the (√3×√3)R30° reconstruction remained pending.

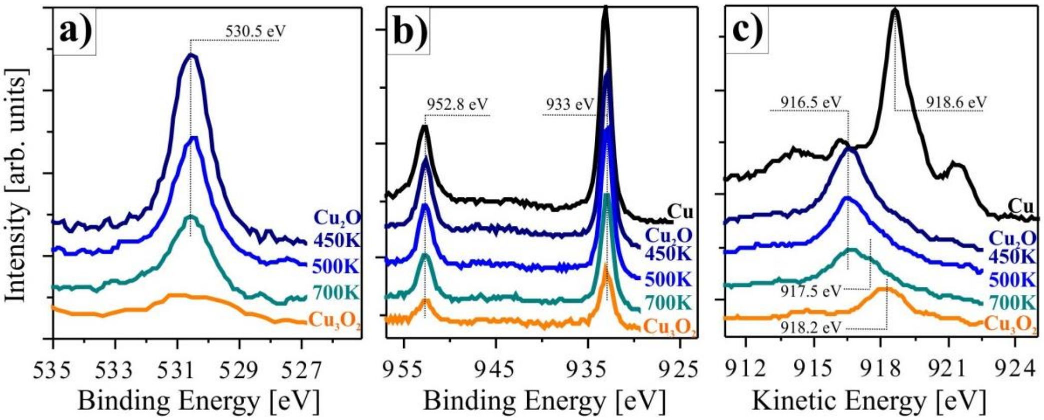

Figure 16: XP spectra of 10 ML Cu on Au(111) exposed to different oxidation conditions. The panels display (a) the O *1s* states, (b) the Cu *2p* states and (c) the *Cu L_3VV* Auger transitions. While the black curve is representative for Cu metal, the blue and orange ones were taken after high- and low-pressure oxidation of the samples, respectively. The low-pressure Cu_3O_2 film was post-annealed to 650 K; the annealing temperature of the high-pressure samples is indicated in the panels. Only the XP fingerprint of the high-pressure films matches the one of Cu_2O bulk crystals.[123]

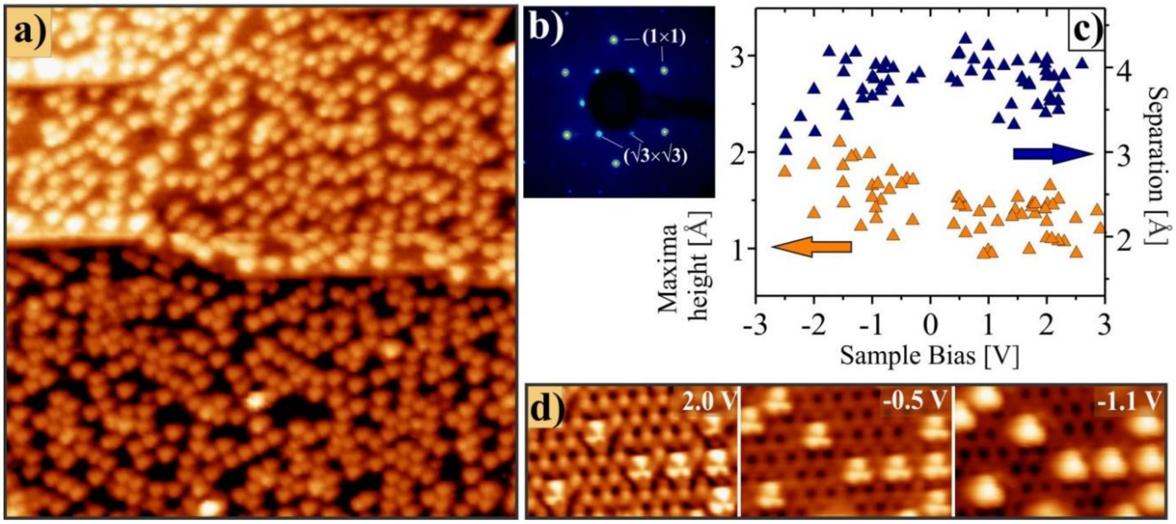

Figure 17: (a) STM image of a bulk-like (√3×√3)R30° reconstructed Cu_2O film on Au(111) (35×35 nm^2, $U_B = -2.0$ V). The surface is densely covered with characteristic triangular maxima. (b) LEED pattern of the Cu_2O(111) surface, showing the fundamental (1×1) spots together with the (√3×√3)R30° reconstruction (E_{kin} = 21 eV). (c) Topographic height and mutual distance of the triangular maxima as a function of bias voltage. Apart from small changes with STM polarity, the protrusions exhibit a bias-independent contrast. (d) Isolated triangular maxima of the (√3×√3)R30° reconstruction, demonstrating their bias-independent appearance in STM (7.5×4 nm^2).[123]

The riddle of the $Cu_2O(111)$ surface reconstruction was finally solved in a joined STM/DFT-HSE study.[114] Starting point was the experimental registry of coexisting (1×1) and (√3×√3)R30° lattices, as seen in LEED, and the apparent STM height of the detected triangular protrusions (1.5 Å, Fig. 17). On that basis, various surface models were constructed, e.g., the removal 1/3 of the low-coordinated surface O_{cus} ions either from the stoichiometric (ST) or Cu-deficient (CuD) termination, or the addition of different Cu-O complexes in the center of every third Cu_6O_6 surface ring. Surface energies of all models were evaluated at the HSE level, revealing a clear preference for a novel surface structure in a wide range of oxygen chemical potentials that was coined the nano-pyramidal reconstruction (PY, Fig. 18). In this structure, the trifold protrusions are made of Cu_4O units positioned in the center of every third Cu_6O_6 surface ring of a Cu_{cus}-deficient (CuD) surface. Hereby, three Cu ions form a triangle that is capped by a terminating O species, while the fourth one locates in the original position of the Cu_{cus}. The thermodynamic preference for this reconstruction largely arises from the chemical saturation of the low-coordinated surface O_{cus} atoms that obtain a fourth binding partner. The terminating O_{cus} species on top of the Cu_4O units binds strongly to their three Cu neighbors, resulting in a high level of chemical saturation. The Cu_4O pyramids populate every third six-membered surface ring, as they simultaneously saturate surface O_{cus} ions in three neighboring rings. It is worth pointing out that, similarly to the CuD termination in Fig. 13, the non-stoichiometry of the PY surface makes its calculated stability very sensitive to the correct account for the surface electronic structure. Consequently, the relative stabilities predicted by HSE and GGA approaches qualitatively differ, confirming the inability of GGA to assess the energetics of Cu_2O surfaces (Fig. 18).

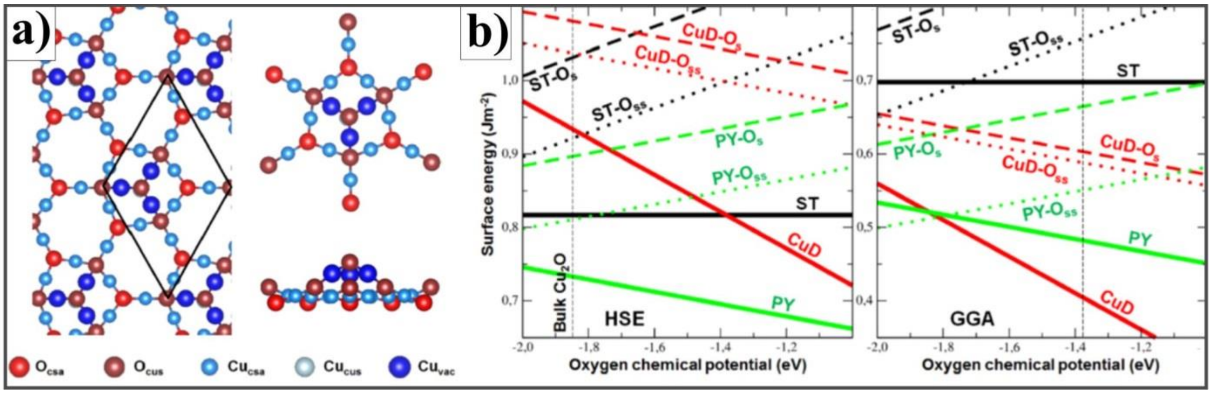

Figure 18: (a) Top and side views of the nano-pyramidal reconstruction (PY) of the (√3×√3)R30° $Cu_2O(111)$ surface with a Cu_4O unit in the center of every third Cu_6O_6 surface ring.[114] (b) Calculated HSE (left) and GGA (right) surface energies of various (√3×√3)R30°-$Cu_2O(111)$ model reconstructions plotted as a function of the oxygen chemical potential. The labels '-O_s' and '-O_{ss}' refer to configurations with surface and subsurface oxygen vacancies, respectively. Energies of stoichiometric (1×1) terminations (ST) are plotted for reference.

In a second step, the authors simulated STM images of all considered surface models and compared them with measured STM data (Fig. 19).[114,123] For the fundamental (1×1) lattice, being occasionally observed as minority phase next to the (√3×√3)R30° reconstruction, chemically saturated (O_{csa}) and unsaturated (O_{cus})

oxygen ions were resolved in the Cu_6O_6 rings. A uniformly dark contrast in the ring center at positive and negative polarity further suggested the absence of Cu_{cus} ions in the surface layer (Fig. 17d). This conclusion is corroborated by simulated STM images of the stoichiometric (1×1) surface that exhibits a clear contrast reversal as a function of bias, while the CuD reconstruction does not.[113] For the (√3×√3)R30° phase, an excellent match between high-resolution STM images and the nano-pyramidal reconstruction was obtained with respect to shape, position and bias-dependence of the triangular protrusions (Fig. 19b). For an O-depleted surface with 1/3 of the O_{cus} ions missing, on the other hand, the appearance of unique Cu_3 triples surrounding the vacancies on the ring perimeter was predicted, in contrast to experimental findings (Fig. 19c).[127] Finally, a Cu_{cus} and O_{cus}-depleted surface results in simulated STM images that are governed by the ring-structure of the $Cu_2O(111)$ surface with localized protrusions marking the O defects in filled and empty state images, respectively (Fig. 19d). Although not observed on regular surfaces, this signature is in line with isolated O defects that occasionally occur in the oxide films, and indeed display the predicted bias-dependent contrast.[114] In general, the measured STM data of an ideal (√3×√3)R30° reconstructed $Cu_2O(111)$ surface with its bias-independent array of triangular protrusions is clearly incompatible with both, O_{cus} and C_{cus}-depleted surface termination.[106,119,122,123]

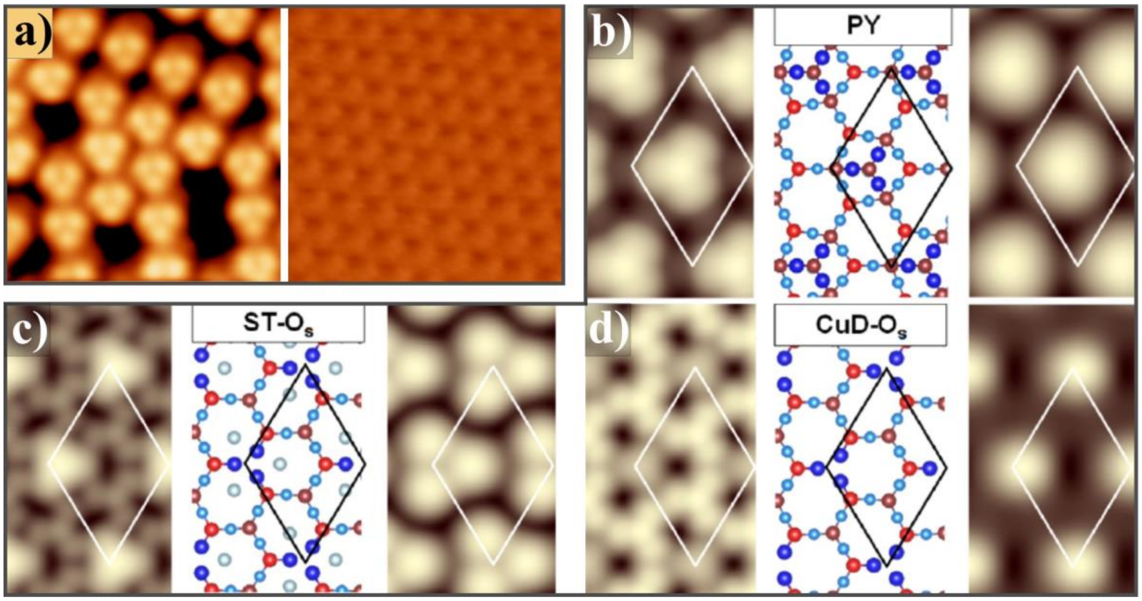

Figure 19: (a) Close-up STM images of the (√3×√3)R30° reconstruction and a (1×1) minority phase of $Cu_2O(111)$, shown on an identical height scale (U_B = -1.1 V, 5×5 nm^2). Simulated constant-current STM images and corresponding atomic representations of (b) the pyramidal, (c) the vacancy ST-O_s and (d) the vacancy CuD-O_s model of a reconstructed $Cu_2O(111)$ surface at negative (left) and positive bias (right).

As a final note, oxygen vacancies in the $Cu_2O(111)$ surface plane turned out to be instable in DFT calculations due to their tendency to migrate subsurface and to localize below the Cu_{cus} cations. The energy difference between a surface and a sub-surface O vacancy was estimated to ~0.3 eV with GGA[128] and to ~0.6 eV with HSE,[114] which renders accumulation of O defects in the very surface plane unlikely. These theoretical results falsify the established interpretation of Cu_2O experiments that assumes a well-ordered array of surface O defects to be present on the $Cu_2O(111)$ surface.[119,129] In contrast, the nano-pyramidal reconstruction model is supported by its outstanding thermodynamic stability, a perfect match to high-resolution STM data, but also by a convincing agreement between calculated and experimental electronic properties, as discussed next.

3.2.2. Electronic properties

A. Band gap and in-gap electronic states

X-ray and ultraviolet photoelectron spectroscopy (PES) was employed to map the VB structure of $Cu_2O(111)$.[106,130] The experiments unambiguously revealed the p-type character of the material, as the VB onset essentially coincides with the Fermi level (Fig. 20a). As far as bulk effects were concerned, the main features in the PES intensity could be interpreted with help of a combined HSE+G_0W_0 approach.[112] The small peak between 0 and -2.0 eV was assigned to the Cu *3d* states hybridized with the O *2p* orbitals, while the pronounced maximum between -2.0 and -4.0 eV is governed by the non-bonding part of the Cu *3d* states. The center of gravity of the O *2p* band only locates below -6.0 eV. At the band edges, the density of states includes contributions from the Cu *4s* and O *3s* orbitals. Since the energies of the *s* orbitals are usually not corrected by the DFT+U method, it becomes clear why the resulting band gap is hardly larger than the GGA one and why hybrid functionals are necessary to significantly shift the band edges. However, the dominant character of the VB and CB edge is Cu *3d* and Cu *4s*, respectively, rendering Cu_2O a typical example for a Mott-Hubbard insulator.[131]

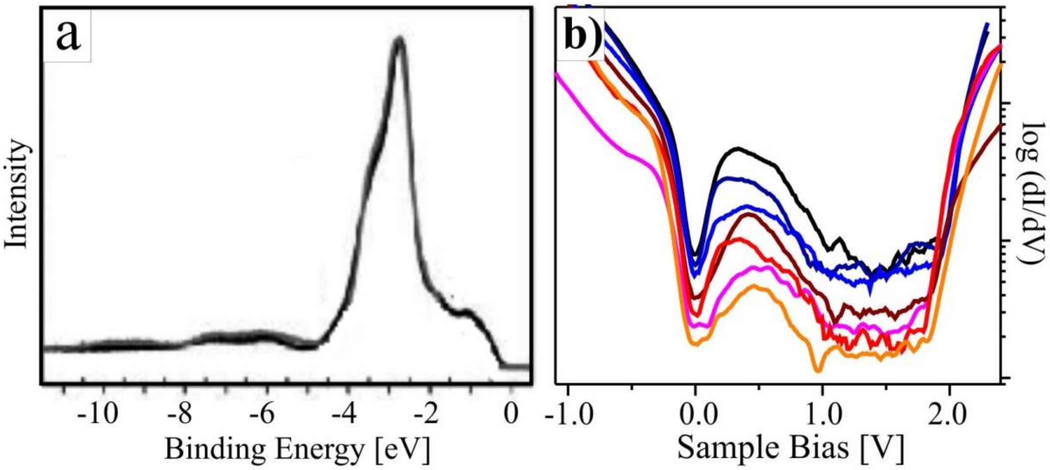

Figure 20: (a) VB structure of $Cu_2O(111)$ measured with PES.[130] (b) STM conductance spectra taken at different positions of thick (upper three curves, 2 nm) and thin (lower four curves, 1 nm) Cu_2O films grown on Au(111). The spectra are displayed in logarithmic representation to highlight the small in-gap intensity. The VB and CB onsets are readily identified at 0 and +1.9 eV, respectively.[134]

Theoretical studies of the $Cu_2O(111)$ surface electronic structure have been performed on the basis of either GGA,[115,116,118], DFT+U,[117,122,132] or HSE methods.[113,133] They consistently disclose the semiconducting nature of the stoichiometric (ST) surface that exhibits a Cu_{cus} gap state with a position sensitive to the employed exchange-correlation functional.[113] Also for the oxygen-deficient $(\sqrt{3}\times\sqrt{3})R30°$ ST-O_s termination, a semiconducting character is revealed with the empty Cu_{cus} state still being present in the gap. In contrast, the top of the VB is intersected by the Fermi level in Cu-deficient terminations, producing a metallic electronic structure. Experimentally, mostly the $(\sqrt{3}\times\sqrt{3})R30°$ reconstructed $Cu_2O(111)$ surface was investigated. In surface sensitive O *1s* core level spectra, two oxygen species were identified, being localized in the bulk and surface of the crystal, respectively.[130] Given the pronounced inhomogeneity of the $Cu_2O(111)$ surface, as caused by different reconstructions and defect features, averaging XPS techniques are unsuitable to provide information on the local electronic properties and their interplay with the atomic structure. For this purpose, STM differential conductance (dI/dV) spectroscopy is the method of choice to examine the surface electronic structure of bulk and thin-film $Cu_2O(111)$.[121,134]

Respective spectra consistently show the band gap of the material, with the VB top located at the Fermi level (E_F) and the CB onset at +1.9 eV, in line with the p-type nature of cuprous oxide (Fig. 20b).[1] Moreover, the measured gap size was found to be identical in thin-film and single-crystal data and agreed with literature values, too.[121,134] This correspondence emphasizes once more that high-pressure Cu_2O films grown on metal supports can be used as model systems for the bulk material. In addition, STM spectra taken on different $Cu_2O(111)$ samples systematically revealed a finite dI/dV intensity in the lower part of the band gap (Fig. 20b). Due to small signal strength, this in-gap intensity is recognized best in logarithmic representations of the dI/dV traces. While the conductance peak is centered at ~0.5 eV in thin-film Cu_2O, it narrows and downshifts to 0.3 V in spectra taken on bulk samples. Several scenarios have been considered to rationalize this unique in-gap intensity, for example resonant tunneling into Cu vacancy states and polaronic effects in the electron transport.[111,134] In order to clarify this point, we discuss spectroscopic fingerprints of the two Cu defects in bulk Cu_2O first (Fig. 21).

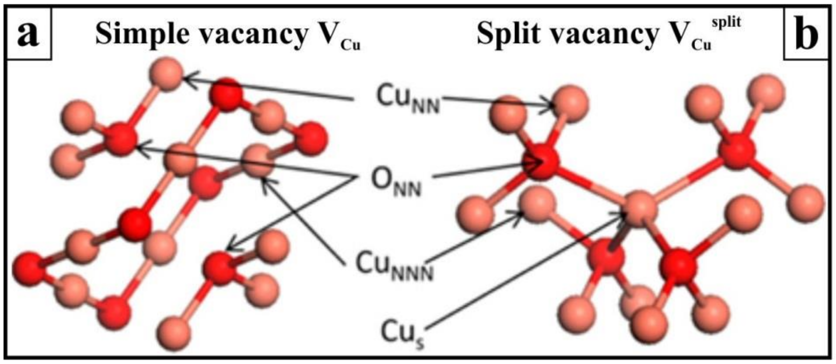

Figure 21: Local structure surrounding (a) V_{Cu} and (b) V_{Cu}^{split} defects in Cu_2O, as derived from DFT calculations. In the split vacancy, Cu_s moves towards the center of the vacancy where it tetrahedrally coordinates to the four nearest neighbour O atoms (O_{NN}). Cu_{NN} are the Cu atoms nearest to Cu_s.[11]

The p-type conductance behavior of Cu_2O has been convincingly linked to the low formation energy of Cu vacancies in the lattice, which gives rise to low-lying acceptor states just above the VB edge.[7] Two types of bulk Cu defects have been identified by DFT calculations.[6,11,12] The so-called simple vacancy evolves from removing one Cu atom from the lattice and inducing a small relaxation of the two neighbouring low-coordinated O_{cus} ions (Fig. 21a). In the split vacancy, a neighbouring Cu moves towards the defect position until it reaches tetrahedral coordination with four adjacent O ions (Fig. 21b). While the structural parameters seem settled for the two defect types, their formation energies and thus their thermodynamic preference are still subject of controversy. In most theoretical approaches, the simple vacancy is energetically preferred over the split one, whereby differences in the formation energy range from 0.83 eV[12] to 0.06 eV,[6] depending on the DFT functional used in the calculations. In a designated HSE work, much higher formation enthalpies were determined, i.e., 1.3 (O-poor) and 1.15 eV (O-rich) for the simple V_{Cu} defect and 1.6 (O-poor) and 1.4 eV (O-rich) for the split vacancy, respectively.[11] Only in one work, the V_{Cu}^{split} defect was found to be lower in energy.[135] Unfortunately, the experimentally determined defect formation energies exhibit an even larger spread, ranging from 0.39 to 0.97 eV/defect, depending on the growth procedure of the Cu_2O samples.[136,137,138] This uncertainty renders a clear assignment of the experimental fingerprints to either simple or split Cu vacancies impossible.

More relevant for explaining the dI/dV intensity in the Cu_2O band gap (Fig. 20b) is however the position of the defect state induced by a given Cu vacancies. Although advanced hybrid functional DFT approaches have been exploited, the calculated single-particle defect energies show a substantial scattering as well. Scanlon et al. found in-gap energy levels of 0.52 and 1.12 eV for the simple and split vacancies in a bulk environment,[12] respectively, while Isserhoff and Carter determined those states to be just above E_F for the simple defect and at 0.57 eV for the split one.[11] These numbers need to be compared with the activation energies determined from temperature-dependent conductivity measurements on high-quality Cu_2O samples, using an Arrhenius approach (Fig. 2a). The relevant experiments clearly disclosed different conductance regimes, governed by a relatively high barrier of 0.4 eV above 500 K, which drops to 0.22 eV in the temperature range from 200 to 500 K and finally reaches 0.16 eV below 250 K.[10] The associated activation energies have been tentatively linked to the V_{Cu}^{split} induced acceptor level (0.4 eV), the simple V_{Cu} state (0.22 eV) and to a conductance mechanism mediated by nitrogen dopants in the Cu_2O lattice (0.16 eV). Alternative techniques, such as deep-level transient spectroscopy and photo-luminescence measurements, confirmed this range of acceptor activation energies. However, substantial scattering of the data between 0.15–0.65 eV with respect to the VB top again prevented unambiguous assignment of the conductance channel to either simple or split Cu vacancies.[139,140,141,142]

In principle, the asymmetric in-gap dI/dV intensity detected in STM conductance spectra of $Cu_2O(111)$ would be compatible with the presence of two gap states, as introduced by two unique Cu defect types (Fig. 20b). In fact, the in-gap maximum can be de-convoluted into two Gaussians centered at 0.4 and 0.75 V, bias values that fairly agree with DFT predictions of the two bulk defect levels.[11,12] Despite these similarities, an assignment of the in-gap dI/dV maxima to resonant tunneling into defect states provided by simple and split Cu vacancies appears implausible for the following reasons. First, with STM spectroscopy as a local probe, it should be possible to identify and differentiate single Cu defects in the surface. However, the in-gap dI/dV response was found to be homogenously distributed across the entire $Cu_2O(111)$ surface. Second, the detected asymmetry of the in-gap intensity is similar at all spectral positions, although simple and split vacancies should exhibit a certain distribution in the film. And third, the intensity of the dI/dV signal varies distinctively with layer thickness in case of Cu_2O films, and can be manipulated via the tunneling current in spectra acquired on Cu_2O bulk crystals.[121] Especially the last observation is in conflict with an interpretation based on resonant tunneling into oxide defect states but rather suggests electric-field effects in the tip-sample junction to be responsible for the in-gap dI/dV intensity. Consequently, an additional aspect needs to be considered for explaining the finite conductance signal in the Cu_2O band gap, namely intrinsic and extrinsic band-bending effects in the reconstructed $Cu_2O(111)$ surface. The origin of surface band-bending and its impact on the electronic structure of different $Cu_2O(111)$ terminations is discussed in the next paragraph.

B. Band-bending effects

Surface band-bending may follow two fundamental schemes, the first one initiated by a deviating stoichiometry of different oxide reconstructions with respect to bulk cuprous oxide (intrinsic band bending), the second one being introduced by an incomplete screening of the tip-electric field at the dielectric surface (tip-induced band bending).

The previously considered $Cu_2O(111)$ reconstructions (Fig. 13), all come with a distinct chemical composition of the surface oxide layers. Only the stoichiometric (1×1) surface (ST) is charge neutral, while the O-deficient ST-O_s with 1/3 of the surface O_{Cus} ions being removed has two excess electrons per $(\sqrt{3}\times\sqrt{3})$ unit cell. The Cu-poor terminations, on the other hand, are all electron-deficient, with the nano-pyramidal (PY) and the Cu-deficient (CuD) reconstruction lacking one and three electrons per $(\sqrt{3}\times\sqrt{3})$ cell, respectively. An intermediate charge state is adopted in the PY-Cu_{cus} phase, which derives from the pyramidal reconstruction with the Cu_{cus} ions below each nano-pyramid being removed. In that surface, formally two electrons are missing per (√3×√3) cell with respect to the stoichiometric case. To deduce the real charge distribution in the surface and the emergence of surface dipoles, screening effects of the formal charge imbalances need to be taken into account. Cuprous oxide, as a prototypical p-type conductor, features high hole mobility, while excess electrons tend to localize in the Cu orbitals of the surface atoms. The screening response and the resulting charge distribution in surface and sub-surface layers of $Cu_2O(111)$ are displayed in the calculated charge profiles shown in Fig. 22.[133] An essentially flat profile is obtained for the stoichiometric termination (ST), as expected from its charge neutrality. A similarly flat profile is found for the Cu-rich ST-O_s termination as well, showing that surface oxygen vacancies do not trigger a considerable subsurface electron redistribution. Indeed, the excess electrons left behind by the missing oxygen atom remain mostly localized on the three nearest Cu neighbors. Conversely, in the Cu-deficient terminations (CuD, PY, and PY-Cu_{cus}), the holes created at the VB top around E_F produce a positive charging which propagates into the subsurface layers S-1, S-2, and beyond. These positive charges are balanced by a negatively charged surface trilayer (S and S+1 layers), as depicted in Fig. 22a.

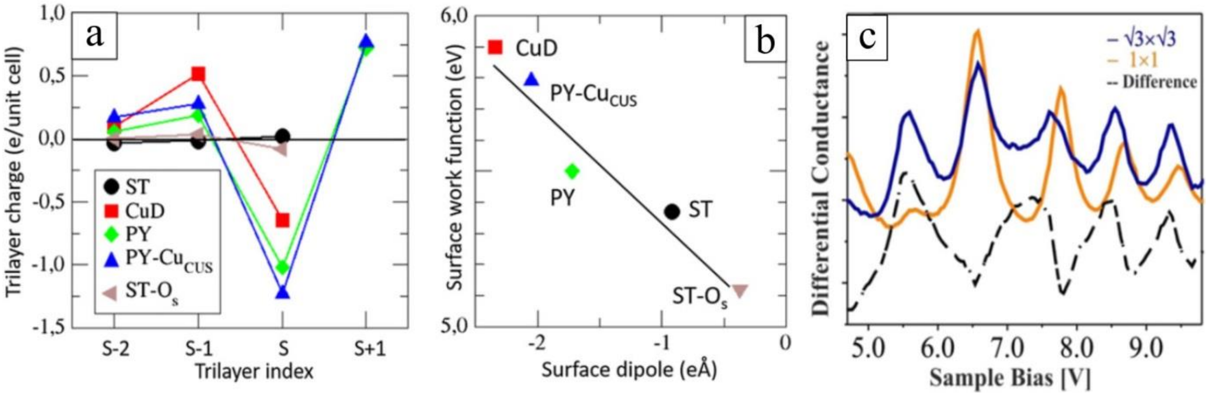

Figure 22: (a) Calculated charge profiles of trilayers in different $Cu_2O(111)$ terminations. Indices S, $S-1$, and $S-2$ refer to the surface, subsurface, and sub-subsurface trilayer, respectively. $S+1$ includes all atoms above the surface plane of the ST surface. (b) Work function of various $Cu_2O(111)$ terminations calculated as a function of their total surface dipoles. (c) Series of field emission resonances (FERs) measured on (√3×√3) and (1x1) patches of $Cu_2O(111)$ films. The black curve shows the difference of the two spectra.[133]

The subsurface propagation of positive charges produces a surface dipole moment that in turn affects the work function ϕ of the different $Cu_2O(111)$ terminations (Fig. 22b). In correspondence to the basic Helmholtz formula, surface dipole and work function follow a nearly linear relationship with the CuD having the largest ϕ value due to its electron-rich surface configuration. Experimentally, the local surface potential of the coexisting CuD and PY terminations has been determined via the positions of field emission resonances (FERs) in the STM junction. The latter correspond to bound electronic states in a potential well formed between vacuum barrier and sample surface.[143] From the results shown in Fig. 22c and a fit of the resonance positions to a triangular particle-in-a-box model, work function values of 5.85 and 5.4 eV were obtained for the (1×1) and (√3×√3)R30° surface, respectively. The results reflect the lower work function of the PY termination with respect to that of CuD, in agreement with the higher Cu-deficiency of the latter. In fact, there is even a quantitative agreement between calculated and experimental ϕ values.

Figure 23 displays the relationship between the surface-charge distribution in different $Cu_2O(111)$ terminations and the electrostatic potentials experienced by Cu and O ions in successive trilayers. The potential shifts are hereby representative for both, the positions of the core levels and the center of gravity of the oxide VB (Fig. 23b). The qualitatively different behavior at O-poor and Cu-poor terminations is best seen in the response of the coordinatively saturated ions (Fig. 23a). While O-poor surfaces display a flat profile, the Cu-poor terminations are characterized by an upward shift of the potential due to hole migration towards subsurface layers, as discussed before. The up-shift of the potential also gives rise to an upward band bending in the Cu-deficient $Cu_2O(111)$ surfaces that disappears for stoichiometric and O-deficient configurations (Fig. 23b,c). An additional up-shift of the atomic levels arises for coordinatively unsaturated ions and originates from the reduced electrostatic potential associated to their low coordination. We note that there is an ongoing discussion in the literature that advocates exactly the opposite trend namely downward band bending on a hypothetical O-deficient (√3x√3)R30° surface.[129,144] However, many assumptions in those works are based on an incorrect surface model. Moreover, DFT calculations predict a unique defect state induced by O vacancies in the upper part of the Cu_2O band gap (see gap state at 1.5 eV in Fig. 23c). A corresponding resonance could never be detected in dI/dV spectra of (√3x√3)R30° reconstructed $Cu_2O(111)$, rendering an ordered array of O defects an unlikely reason for the observed surface reconstruction.

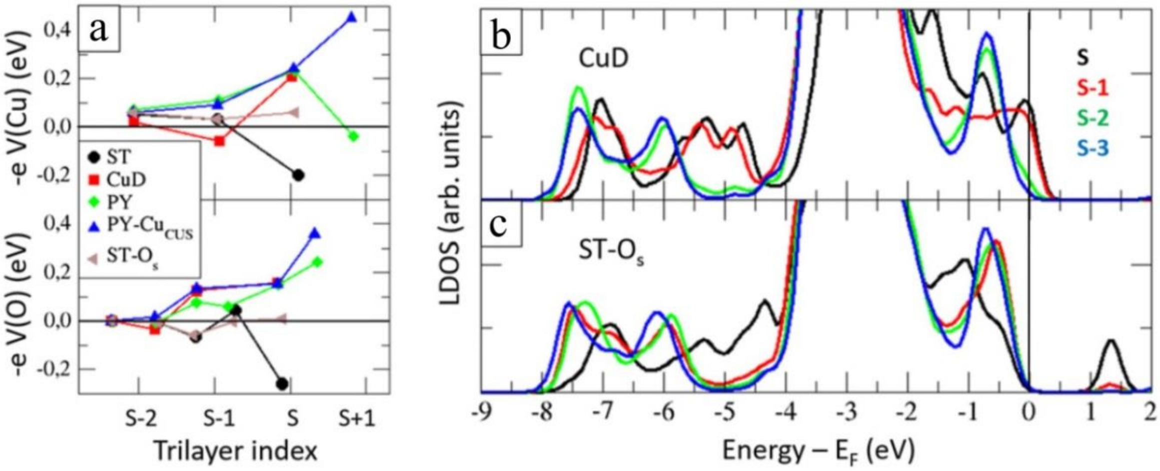

Figure 23: (a) Relative positions of atomic levels at the saturated O (−eV(O)) and Cu ions (−eV(Cu)) in S, $S-1$, $S-2$ and $S+1$ trilayers of different $Cu_2O(111)$ terminations. Density of states of (b) the CuD and (c) the ST-O_S termination projected on Cu atoms in the indicated trilayers.[133] The upward band bending in Cu-deficient surface reconstructions is clearly revealed.

The upward bending of surface bands induced by the nano-pyramidal Cu_2O reconstruction now provides a reliable explanation for the in-gap intensity detected in the lower part of the Cu_2O gap at 0.5 eV (Fig.

20b).[134] The p-type nature of Cu_2O puts the Fermi level to the VB top already in a bulk environment. The upward band bending at the Cu-deficient (√3x√3)R30° reconstruction further pushes E_F into the VB, producing an empty-state pocket at the band edge. While tunneling into this pocket is inefficient at zero bias, given the vanishing electric field in the tip-sample junction, an electron current can be detected at small positive bias, as electrons propagate from filled states in the tip towards empty states in the VB pocket. The result is a finite dI/dV intensity in the lower part of the oxide band gap, as reproducibly detected in dI/dV spectra of the reconstructed $Cu_2O(111)$ surface (Fig. 20b).

Additional proof for this band-bending model comes from modulations of the in-gap intensity in STM spectroscopy measurements either with oxide thickness for supported Cu_2O films or with the tip electric field in the case of bulk crystals.[121,134] In both cases, the intrinsic band bending due to a non-stoichiometric surface is reinforced by the electric field from the STM tip that penetrates deep into the dielectric oxide material. The consequence is a larger in-gap peak for thicker Cu_2O films, as the diminishing screening response of the metal support promotes band-bending in the oxide layer, hence the size of the empty VB pocket. On bulk Cu_2O with its low free-carrier density, tip-induced band-bending effects become evident at the CB onset as well. Here, a continuous shift of the CB edge from its zero-field position at 2.0 V to above 3.0 V is observed upon rising the tunneling current, hence the tip electric field (Fig. 24a). By fitting this shift to the Poisson equation, describing electric-field screening by the carriers of a dielectrics, an approximation of the carrier density in the Cu_2O surface is obtained (Fig. 24b). Interestingly, the CuD (1×1) surface has a much better screening ability than the (√3×√3)R30° pyramidal reconstruction, in perfect agreement with the higher Cu-deficiency of the former.

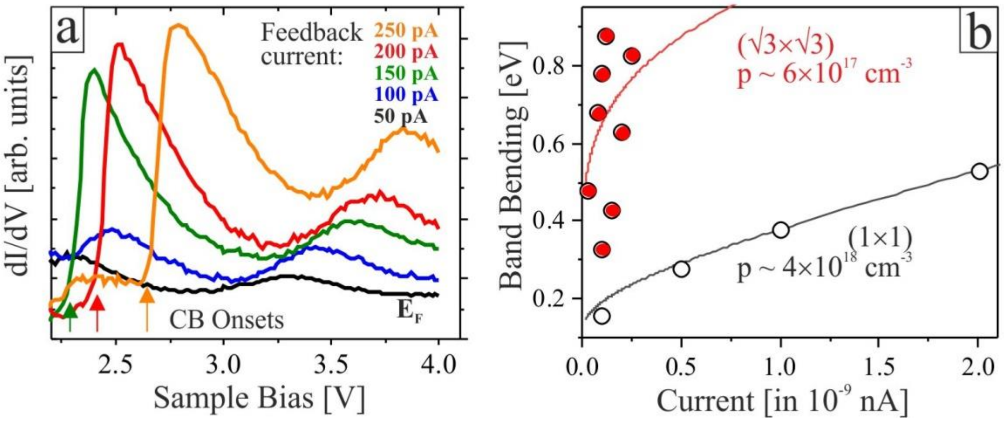

Figure 24. (a) Bias-dependent dI/dV intensity measured at constant-current conditions on bulk $Cu_2O(111)$. The CB onset of the oxide, readily recognized by the sudden conductance rise, experiences an upshift with increasing tunneling current, hence with larger electric fields (see arrows). (b) Tip-induced band bending calculated for two carrier concentrations (solid lines) in comparison with experimental values obtained on (√3×√3)R30° and (1×1) reconstructed patches of a $Cu_2O(111)$ bulk crystal (red and black dots, respectively). The carrier densities required to reproduce the measured screening response are given in the plots.[121]

C. Properties of the $Cu_2O(111)$ conduction band

STM conductance spectra acquired on different $Cu_2O(111)$ surface reconstructions revealed different d*I*/d*V* intensity courses in the region of the oxide CB. While the band onset shows up by a sudden increase of the dI/dV intensity at 2.1 V in the (√3×√3)R30° reconstructed regions, it is less pronounced in the (1×1) minority phase (Fig. 25a).[133] A similar behavior is observed in d*I*/d*V* maps of the oxide surface. The Cu_4O maxima of the (√3×√3)R30° phase turn bright and develop a sombrero shape, i.e., a bright center surrounded by a dark ring, directly at the CB onset at 2.1 V. As the bias increases, the contrast diminishes and even inverts at ~3.0 V, when the Cu_4O maxima exhibit lower conductance than the environment (Fig. 25b).

These peculiarities in the dI/dV intensity can be related to the energy course of the Cu-projected local density of states (LDOS). It exhibits a characteristic dip at ∼3.0 eV (Fig. 25c), arising from different CB onsets in different oxide regions. The stoichiometric (ST) and pyramidal (PY) phase show low-lying band onsets due to a characteristic LDOS peak at 2.5 eV, related to the presence of Cu_{cus} surface species. In contrast, no Cu_{cus} atoms are available in the CuD and PY-Cu_{cus} terminations, and the band onset consequently up-shifts to 3.0 eV. It is the missing LDOS peak at 2.5 eV that reduces the dI/dV intensity at the CB onset of the (1×1) but not of the (√3×√3)R30° termination of $Cu_2O(111)$ (Fig. 25a).[133]

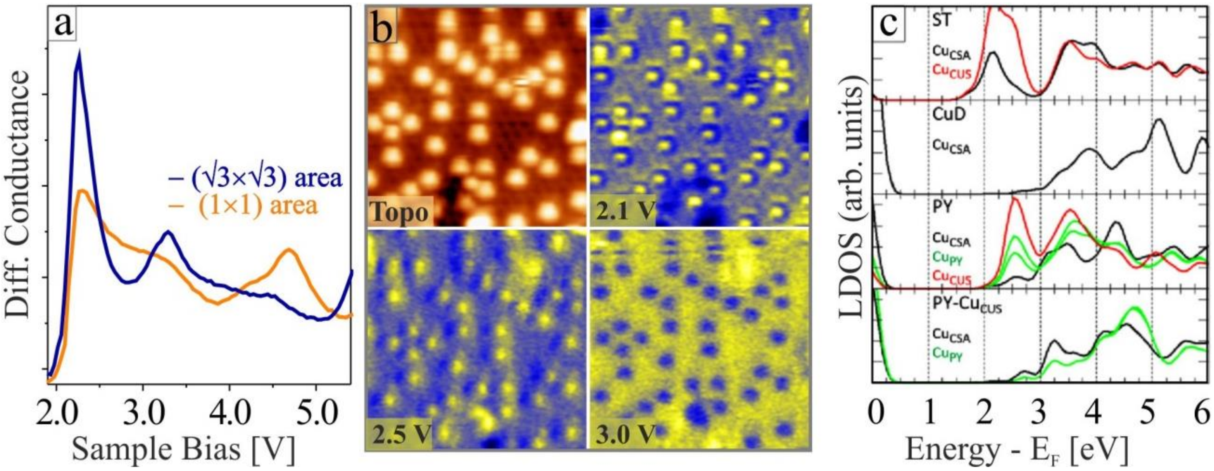

Figure 25: (a) Differential conductance (d*I*/d*V*) spectra covering the CB onset in (√3×√3)R30° and (1×1) regions of the $Cu_2O(111)$ surface. (b) Topography and conductance maps of $Cu_2O(111)$ taken at bias values around the CB onset ($I = 50$ pA, 12 × 12 nm^2). (c) LDOS of the CB region, projected onto inequivalent surface Cu atoms at the ST, CuD, PY, and PY-Cu_{cus} termination.[133]

3.2.3. Adsorption behavior and reactivity

Given its thermodynamic stability, the $Cu_2O(111)$ surface has been subject of numerous adsorption studies performed by spectroscopic and imaging techniques. Early experimental studies by Cox and coworkers date back to the 1990's, and addressed the effect of oxygen adsorption to the (1×1) termination.[106] For low and moderate O_2 exposure ($<10^4$ L), no O_2 uptake was revealed, indicating the chemical inertness of the (1×1) surface. Using STM and XPS, the adsorption of water and SO_2 on a $(\sqrt{3}\times\sqrt{3})$ reconstructed $Cu_2O(111)$ surface was examined by Önsten and co-workers later.[145] Water adsorption at 150 K resulted in a pronounced O *1s* peak due to molecular adsorption and a weak OH signal compatible with 10% dissociative interactions. Upon annealing to 180 K, the OH coverage increased to 20%, while the molecular water completely desorbed. Water adsorption at room temperature turned out to be ineffective. In contrast, SO_2 binds in the form of SO_3 to the $Cu_2O(111)$ surface, as deduced from a new O *1s* component at 531 eV in XPS.[145] At 150 K, the saturation coverage of 40% is reached, declining to 9% at room temperature. These observations have been corroborated by XP spectra covering the S *2p* core level region. Both, H_2O and SO_2 adsorption has been tentatively related to the activity of twofold under-coordinated O ions, as produced by Cu defects in the surface.[145] Moreover, two STM studies dealt with the interaction of water with copper oxide surfaces, however, only addressed the ultrathin precursor oxide grown on metal substrates. In a first work, magic water clusters composed of one or few cyclic H_2O hexagons have been prepared by low-temperature water deposition plus 300 K annealing on the oxide surface.[146] The individual water clusters could be resolved by STM, their internal structure was rationalized by means of DFT+U calculations. In a second experiment, the water was dosed at 100 K and organized on the oxide surface by gradual annealing.[147,148] At 155 K, desorption of the water multilayer was detected via thermal desorption spectroscopy, while the monolayer remained bonded up to 175 K, a temperature compatible with physisorptive interactions. High resolution STM images of the latter revealed H_2O monolayer islands without apparent long-range order (Fig. 26 a,b). Pair correlation functions calculated from these images revealed, however, a hexagonal short-range order of the individual water molecules with a mean distance of 6 Å, i.e., in registry with the $Cu_2O(111)$ lattice (Fig. 26 c,d). Also, the H_2O assembly into distorted six-membered molecular clusters was clearly revealed in this study. Further experiments investigated methanol adsorption and desorption processes on $Cu_2O(111)$ and (100) surfaces, as a means to explore CH- and CO- bond breaking reactions on oxide surfaces.[149] Dissociative methanol bonding was revealed already at temperatures as low as 140 K and led to the formation of mixed layers on the oxide surface, comprising methoxy, formaldehyde and CH_xO_y species. Hereby, the (111) surface was ound to be more reactive than its (100) counterpart.

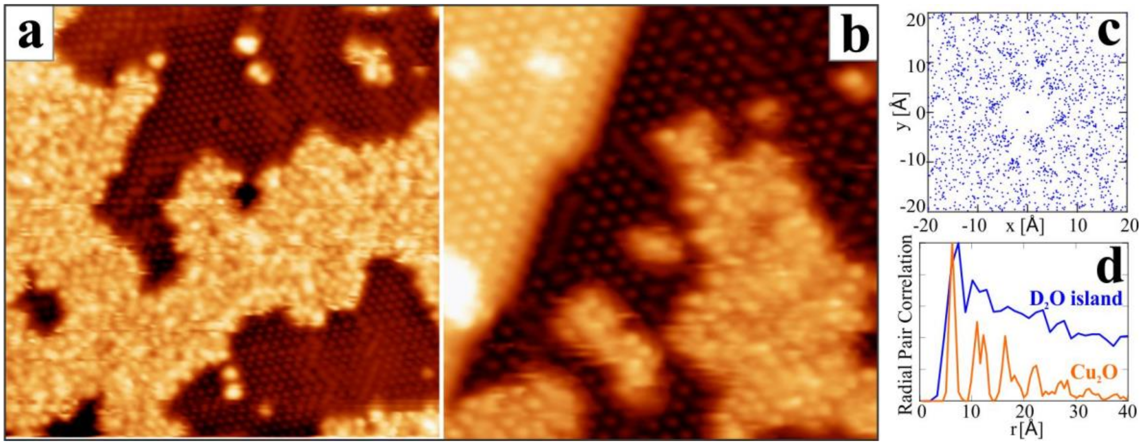

Figure 26: High-resolution STM images of water islands on $Cu_2O(111)$ thin films (a) (28×28 nm^2) and (b) (15×15 nm^2). (c) 2D and (d) radial pair-correlation function of water related maxima and the bare Cu_2O surface, as calculated from the STM image in panel (a). Despite local disorder, the water molecules follow the registry of the $Cu_2O(111)$ surface and adopt the same binding periodicity.[147]

True atomistic insights into $Cu_2O(111)$ adsorption properties, especially into binding sites and interaction mechanisms, have been generated by different DFT studies. The theoretical exploration of $Cu_2O(111)$ was initiated by a DFT+U study on CO_2 adsorption to stoichiometric, as well as Cu_{cus} and O_{cus}-deficient terminations.[150] On the stoichiometric surface, the energetically preferred binding scenario is a linear, neutral CO_2 in tilted configuration, attached to a chemically unsaturated Cu_{cus} ion (E_B = 0.4 eV with dispersion). In the presence of surface defects, bent CO_2 geometries were found, indicative for a charge transfer towards the molecule. However, the presence of defects results in an overall decrease of the mean adsorption energy, and the removal of the Cu_{cus} ions suppresses the most active sites for CO_2 adsorption.

A rather similar DFT binding scenario was uncovered for water on the $Cu_2O(111)$ surface.[151] Here, attachment of the water oxygen to low-coordinated Cu_{cus} ions produces the most effective, associative binding configuration (E_B = -1.1 eV), whereas hydrogen bonding to O_{cus} ions is less favorable (Fig. 27). Dissociative binding can be discarded, as the individual OH and H binding contributions do not compensate the energy costs of the water splitting. As discussed for the CO_2/Cu_2O adsorption system before, a Cu_{cus} depleted surface becomes inactive for water adsorption and is chemically inert. Two further DFT-based studies essentially reproduced the H_2O adsorption behavior discussed before.[152,153] Again, the Cu_{cus} surface ions were found to be the preferred adsorption sites in the low-coverage regime, while binding to low-coordinated O_{cus} ions solely takes place upon approaching monolayer coverage. As expected, population of less-preferred binding sites at higher coverage is accompanied by a gradual reduction of the mean binding energy that downshifts from -1.7 to -1.1 eV when going from one to eight H_2O molecules per unit cell, respectively. Dissociative binding scenarios of water become important only in presence of O vacancies in the $Cu_2O(111)$ surface.[154] We note that the thermodynamically preferred nano-pyramidal reconstruction of

$Cu_2O(111)$ actually lacks Cu_{cus} surface ions,[114] i.e., the primary water binding site. The topic of water adsorption to realistic $Cu_2O(111)$ surfaces thus requires careful revision both, from experiment and theory.[146]

A comparative study on oxygen adsorption to all three low-index Cu_2O planes was presented in Ref. 155. On the (111) surface, atomic oxygen preferentially binds to hollow positions formed by three Cu surface ions, two Cu_{csa} and one Cu_{cus}. A similar position is adopted by the O_2 molecule, with one O atom located above the Cu_{cus} ion and the other one on a Cu_{csa}-Cu_{csa} bridge site. Dissociation of the molecule is preferred by 0.25 eV, whereby both atoms propagate towards adjacent Cu hollow sites. Given its high symmetry and chemical saturation, the $Cu_2O(111)$ surface shows the lowest incentive for O_2 dissociation, while 1.16 eV and even 2.43 eV excess energy are released upon O_2 splitting on the $Cu_2O(110)$ and (100) surface. In both cases, the dissociation involves low-coordinated Cu_{cus} ions and results in a substantial reconstruction of the oxide top layer.[155] Again, the calculations neglect more recent atomic models of Cu_2O surface reconstructions, and cannot rely on an experimental verification of the proposed binding scenarios.

Finally, metal adsorption to the $Cu_2O(111)$ surface has been identified as a promising pathway to produce single-site catalysts.[156] A systematic DFT screening of the bonding behavior of transition metal atoms to $Cu_2O(111)$ revealed that especially the noble metals Pd, Pt and Au show a high tendency to bind as single atoms due to a highly negative binding energy and a positive dissolution energy on the oxide surface. The first successful preparation of a single-atom catalysts is reported in Ref. 157. In this experiment, Co-phthalocyanine molecules were dosed onto a O-deficient $Cu_2O(111)$ surface and decomposed via oxygen-annealing, whereby the central Co atom gets released and attaches to an O vacancy site.

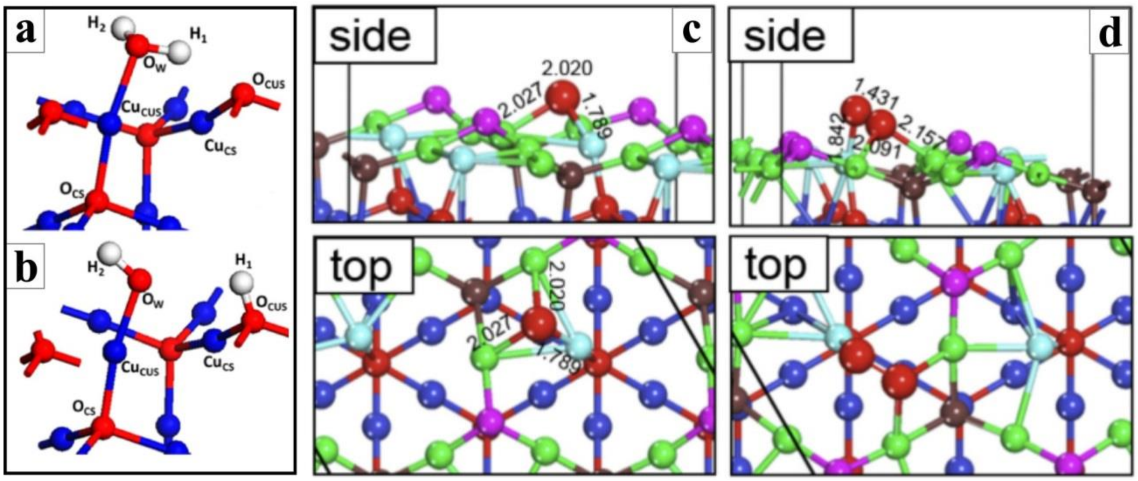

Figure 27: Optimized adsorbate geometries on stoichiometric $Cu_2O(111)$ with (1×1) periodicity, (a) datively bonded water at 0.5 ML coverage and (b) dissociated water at 1 ML coverage.[151] (c) Atomic and (d) molecular oxygen adsorption to $Cu_2O(111)$ (Cu_{cus}: light blue, Cu_{csa}: green, surface O: purple, other O: brown, red).[155]

3.3. The $Cu_2O(100)$ surface

3.3.1 Termination: Theory and experiment

As stated earlier, the (100) surface of Cu_2O is a Tasker-type III polar surface, as positively charged 2 Cu^+ and negatively charged O^{2-} atomic planes alternate in the direction perpendicular to the surface.[2] The bulk-cut (100) surface can thus be either O- or Cu-terminated, but is expected to undergo reconstructions to remove the macroscopic dipole and lower the surface energy. The ideal, bulk-cut surface can be seen as made of a square network of Cu_4O tetrahedrons with 4.3 Å periodicity, comprising two O ions above and two O ions below the Cu plane (Fig. 12). Already early diffraction experiments by Schulz and Cox unraveled the large susceptibility of $Cu_2O(100)$ for structural reconstructions.[106,158] Upon ion sputtering and vacuum annealing at 500 K, a faint $(3\sqrt{2}\times\sqrt{2})R45°$ superstructure was revealed in electron diffraction, although there were many missing spots in the LEED pattern. The surface was tentatively assigned to the Cu terminated phase, produced by oxygen desorption from the surface at the O-poor preparation conditions. At slightly lower annealing temperature (450 K), a $(\sqrt{2}\times\sqrt{2})R45°$ developed, indicative for partial removal of the oxygen top-layer. A surface with (1×1) registry could only be obtained upon heavy oxygen dosage of 10^9 L, suggesting the development of an O-terminated $Cu_2O(100)$ surface. The differentiation between Cu-rich and O-rich surfaces was further corroborated by XPS measurements, revealing a distinct drop in the Cu-to-O ratio from 1.6 to 1.3 at annealing temperatures above 800 K.[106]

The underlying atomic structure of the bulk-cut (1×1) Cu-terminated surface was examined in a first DFT-GGA work performed by McClenaghan et al.[159] They proposed the bulk-cut termination to be charge-compensated via an electronic reconstruction mechanism, implying partial filling of the Cu conduction states. Indeed, the authors found a reduced charge at the surface Cu_{cus} atoms, being equivalent to roughly $^1/_3$ of the bulk value. Moreover, strong relaxation effects take place, resulting in the formation of Cu dimers at the surface and between the first and third layers (Fig. 28). Upon relaxation, the Cu-Cu distances in the surface and perpendicular to it shrink from 3.02 Å to 2.37 Å and 2.46 Å, respectively. The dimerization is associated with a splitting of the compensating Cu states, transforming the local electronic structures from metallic to semiconducting. Subsequent GGA,[115,160] and DFT+U simulations[117] on this (1×1) termination essentially reported the same dimerized structure. Working in a (2×2) unit cell, Le et al. additionally showed that slightly more energy may be gained by forming pairs of dimer rows (ridge-dimer reconstruction in Fig. 28b).[160] In addition, the (1×1) O-terminated surface, comprising one bridging surface oxygen per unit cell, was studied with a GGA approach,[115] and a moderate inward relaxation of the top-most O ions was found. This termination is favored over the (1×1) Cu-terminated one in a large span of O-moderate and O-rich conditions, relevant to most UHV experiments. Removing a single Cu_{csa} or O_{csa}

in the smallest (1×1) Cu- or O-terminated surface, respectively, is in most cases thermodynamically unfavorable with respect to the ideal configuration. Only a Cu-termination with one half of the Cu atoms missing, which corresponds to a polar compensated configuration, displays a lower energy than the corresponding ideal surface. The semiconducting electronic structure of this surface was disclosed in Ref. 161.

Within this first period of time, the experimentally detected (3√2×√2)R45° superstructure of $Cu_2O(100)$ was only addressed by simulations of bulk-cut terminations in the experimental unit cells, using either a GGA approach,[160] a molecular dynamics GGA simulation,[161] or a DFT+U calculation.[117] The first study found that the (3√2×√2)R45° is unstable and relaxation leads to a (√2×√2)R45° surface pattern displaying rows of paired Cu dimers (Fig. 28b). Overall, the dimer characteristic did not change significantly with respect to that obtained in the (1×1) cell and no major energy gain was found upon increasing the unit-cell size. Consequently, no convincing explanation for the superstructure pattern detected in diffraction experiments was provided. In parallel, DFT+U calculations were employed to explore the reconstruction of the O-terminated surface by removing one-half of the surface anions in a (√2×√2)R45° unit cell.[117] By reducing the formal charge of the surface plane by half, such a reconstruction perfectly heals the polarity of the ideal oxygen termination. The (√2×√2)R45° structure was found to be the most stable in typical O environments of an UHV experiment, while the transition towards an unreconstructed (1×1) O-surface was predicted at excessively O-rich conditions. This (√2×√2)R45° reconstruction nevertheless has an energy nearly twice as large as that of the non-polar (1×1) (111) termination (1.17 J/m^2 vs 0.67 J/m^2), in agreement with the abundance of (111) with respect to (100) facets observed for Cu_2O nanoparticles.[35,36,37,38]

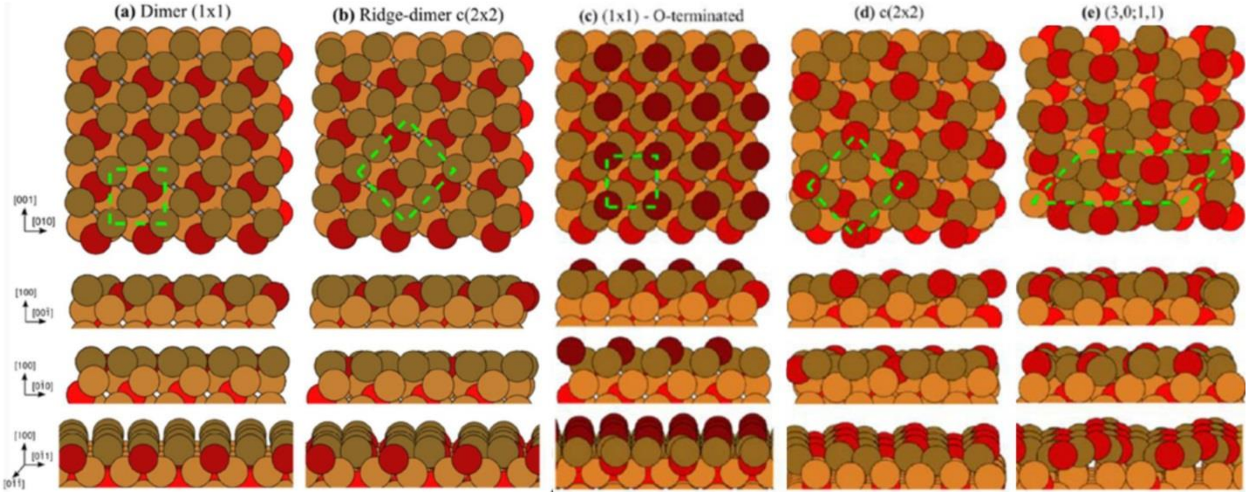

Figure 28: Top and side views of various models of the $Cu_2O(100)$ surface: (a) dimer rows and (b) pairs of dimer rows on the Cu-termination, (c) (1×1) O-termination, (d) c(2×2) and (e) (3,0;1,1) reconstructed Cu-termination. Oxygen: Red and purple balls, Copper: dark and light brown.[162]

As in the case of $Cu_2O(111)$,[114] an improved experimental description of the $Cu_2O(100)$ atomic structure became possible only with the availability of high-resolution STM images. In a systematic STM and LEED study, the group of Weissenrieder et al. explored the nature of the $Cu_2O(100)$ surface in a wide range of pressure and temperature conditions.[149,162] Three terminations were identified in the phase diagram. The most abundant one is the (3,0;1,1) reconstruction, defined here in matrix representation, that could be stabilized by moderate vacuum and oxygen annealing in a temperature window from 850 to 970 K (Fig. 29a). The (3,0;1,1) surface with its two 90° rotational domains does not match the $(3\sqrt{2}\times\sqrt{2})R45°$ phase initially proposed by Cox.[106] The (3,0;1,1) surface always coexists with a c(2×2) reconstruction assigned to the $(\sqrt{2}\times\sqrt{2})R45°$ Cu-terminated surface. The latter becomes dominant in vacuum-preparation schemes especially after elongated sputter and anneal cycles. Finally, a simple (1×1) phase could be prepared by 900 K annealing in 10^{-5} mbar O_2, pointing towards an O-terminated surface (Fig. 29c). We note, however, that the employed thermodynamic conditions to trigger a transition from the reconstructed $(\sqrt{2}\times\sqrt{2})R45°$ to the unreconstructed (1×1) O-terminated surface are not as oxygen-rich as predicted in Ref. 117 ($\Delta\mu_O$= -1.7 eV versus -1.1 eV).

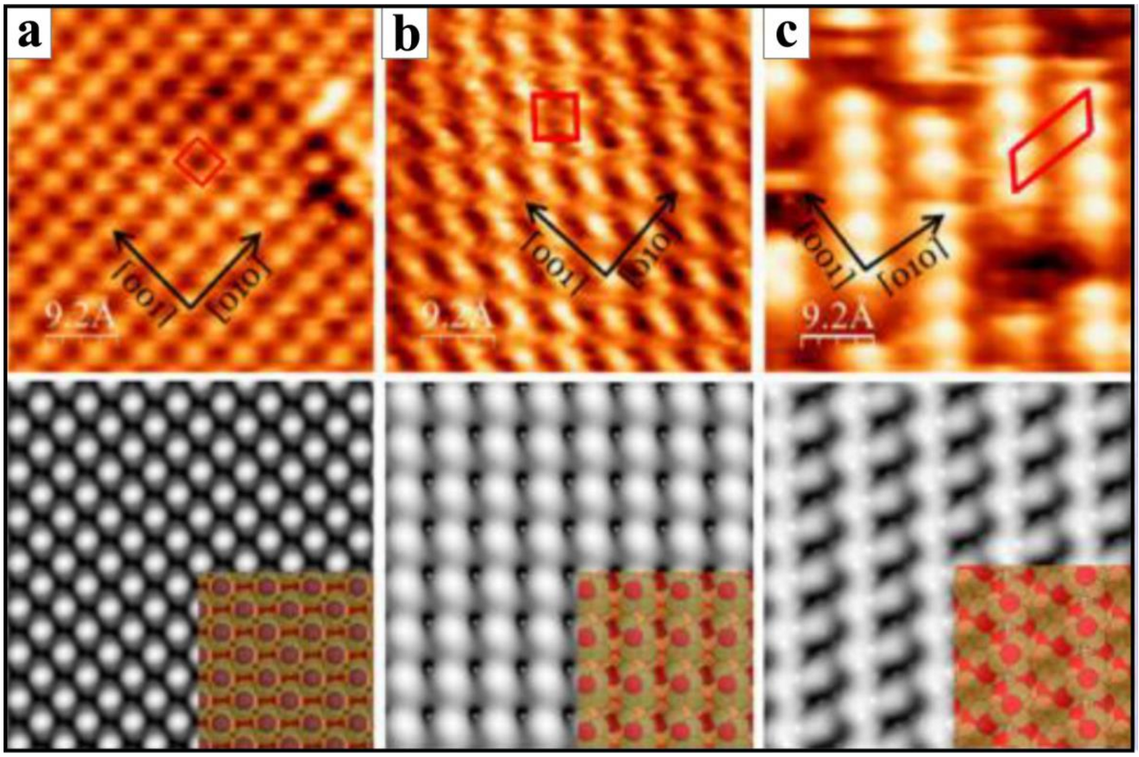

Figure 29: STM images (46×46 Å^2) of the three surface reconstructions found on $Cu_2O(100)$: (a) (1×1) collected at V= −1.8 V, I = 0.5 nA. (b) c(2×2), V= 1.1 V, I = 0.1 nA, and (c) (3,0;1,1), V= 2.8 V, I = 0.3 nA. Simulated STM images and atomic structure models are displayed in the lower row. Bright areas correspond to protrusions.[162]

For all three terminations, the atomically resolved STM images formed the basis for a DFT+U modelling, including relaxation of the two outermost atomic layers with a molecular dynamics approach.[162] The proposed atomic models (Fig. 28) derive directly from bulk-cut O- or Cu-terminated $Cu_2O(100)$ surfaces. Those for the (1×1) O- or Cu-terminations as well as for the two c(2×2) terminations (with simple Cu dimers or ridge-dimers) are essentially in agreement with the previously quoted findings.[115,117,159,160] The (3,0;1,1) model is a strongly relaxed Cu-terminated surface, at which every second subsurface oxygen moves to the surface, while simultaneously the subsurface Cu^+ cations dimerize along the [011]-direction. The vertical separation between the topmost O and Cu planes diminishes, and the overall surface develops a wavy corrugation with 3× 4.3 Å periodicity in agreement with the STM data. The presence of unsaturated oxygen atoms at the surface is in line with a low-energy shoulder next to the O*1s* peak in XP spectra that could be reproduced in simulations of the core level shifts as well.[162] All models of relaxed Cu-terminated surfaces, whether (1×1), c(2×2), or (3,0;1,1), are extremely close in energy, which is not surprising since they differ by size and symmetry of the unit cells, allowing for more or less relaxation, but not by their intrinsic composition. Since all of them are polar, compensated by the electronic reconstruction mechanism, and considering how the results of hybrid calculations have changed our view onto such surfaces, additional HSE simulations are requested to complement our understanding of the (100)-oriented surfaces.[113]

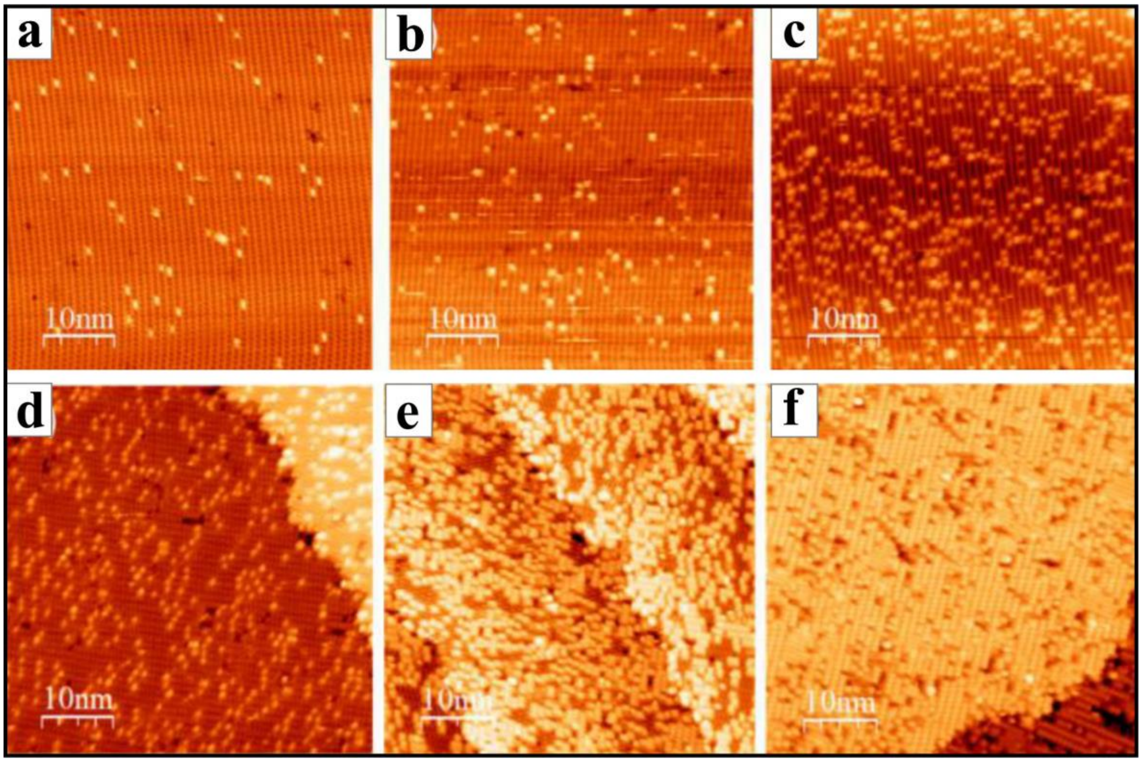

Figure 30: STM images of the clean $Cu_2O(100)$ surface (2.4 V, 0.12 nA) with increasing density of defects after (a) annealing at 650 °C for 10 min, (b) at 650 °C for 40 min, and (c) at 700 °C for 20 min. (d) STM images of the as-prepared $Cu_2O(100)$ surface (2.4 V, 0.12 nA) and after (e) 4 min and (f) 6 min electron bombardment (E_{kin} = 80 V, current: 5 μA).[163]

In a subsequent study, also defects on well-prepared $Cu_2O(100)$ surfaces have been addressed in detail.[163] The most abundant defect type shows up as a 1.6 Å-high protrusion in empty-state STM images, and tends to form rows aligned with the oxide [011] direction. Its concentration can be systematically altered by vacuum annealing and soft electron bombardment of the sample (E_{kin} = 80 eV, Fig. 30). Based on accompanying DFT calculations, the defects were assigned to oxygen vacancies located in the valleys between two rows of terminal O ions of the (3,0;1,1) $Cu_2O(100)$ surface. The vacancy formation energy was estimated to 2.04 eV, which is about 17% smaller than for the topmost O ions in the unreconstructed O-terminated surface. Despite the pronounced p-type character of Cu_2O, no signatures for Cu vacancies were revealed in that study.[163]

3.3.2 Adsorption behavior and chemical reactivity

Although numerous adsorption studies on cuprous oxide have been reported in the literature, we will concentrate here only on those performed on well-defined (100) surfaces with known termination. The era of adsorption experiments was again opened by Cox and coworkers with a set of thermal desorption spectroscopy (TDS) studies. Upon water dosing on the $(3\sqrt{2}\times\sqrt{2})R45°$ reconstructed surface, two main desorption peaks were distinguished, a high-temperature one at 465 K and a low-temperature one that gradually downshifts from 210 to 165 K with increasing coverage.[164] The former peak exhibits first-order desorption behavior and yields a H_2O binding energy of 1.27 eV, compatible with a Mars-van Krevelen-type desorption scheme involving lattice oxygen. The low-energy desorption follows a second-order scheme and has been explained with the recombination of surface OH and hydride species. The formation of copper hydrides due to attachment of atomic hydrogen to low-coordinated Cu_{cus} species has been proposed in an independent work.[165] In addition, carbon monoxide (CO) exposure to the $(3\sqrt{2}\times\sqrt{2})R45°$ reconstructed $Cu_2O(100)$ gave rise to multiple peaks in TDS, appearing at 280, 220, 180 and 140 K at low coverage and shifting downward in temperature as the coverage increased.[158] The four desorption peaks are compatible with CO binding energies of 0.69, 0.54, 0.46 and 0.36 eV, respectively. Although the precise CO binding sites could not be identified in that early study, due to a lack of theoretical support, the high-energy adsorption has been explained with CO attachment to surface Cu^+ species according to the Blyholder scheme. Interestingly, the measured binding energy is even higher than that on a Cu(100) metal surface.[166]

The picture of molecular adsorption to $Cu_2O(100)$ surfaces has sharpened substantially in a series of combined experimental / theoretical papers that were published in the late 2010's by Weissenrieder and Brinck. They were initiated by revisiting the water binding characteristics to $Cu_2O(100)$.[167] Main finding of the study was the high susceptibility of the surface to water dissociation and OH formation even at low temperature (Fig. 31). Respective XPS data revealed that already water dosage at 117 K results in an OH coverage of 0.3 ML, measured with respect to the (1×1) surface, while additional water binds associatively. Upon rising the temperature to 180 K, the OH surface coverage increased to 0.4 ML while the molecular water desorbed. The OH coverage gradually declined again with increasing temperature due to recombinative water desorption, however, residual hydroxyls could be detected on the surface until 500 K, in line with the early results of Cox.[164] The process of water adsorption and dissociation is accompanied by a transformation of the initial (3,0;1,1) reconstruction into a (1×1) phase.

The underlying reaction mechanism has been clarified by DFT calculations.[167] Molecular water preferentially adsorbs to Cu-hollow sites by forming a hydrogen bond to an adjacent surface O species in the reconstructed surface (Fig. 31b). At low coverage, water dissociation is exothermic, and the hydroxyls get stabilized in Cu-Cu bridge positions. The associated binding energies are substantial and can reach 1.1 eV on the most favorable positions. Similar binding sites are adopted by protons that arise from heterolytic water splitting. However, also homolytic H_2O bond cleavage is active on $Cu_2O(100)$, whereby a hydrogen molecule desorbs and the oxygen adatom remains on the surface. The associated accumulation of surface oxygen was now suggested to trigger the lift-off of the (3,0;1,1) reconstruction and to stabilize the O-terminated (1×1) surface.

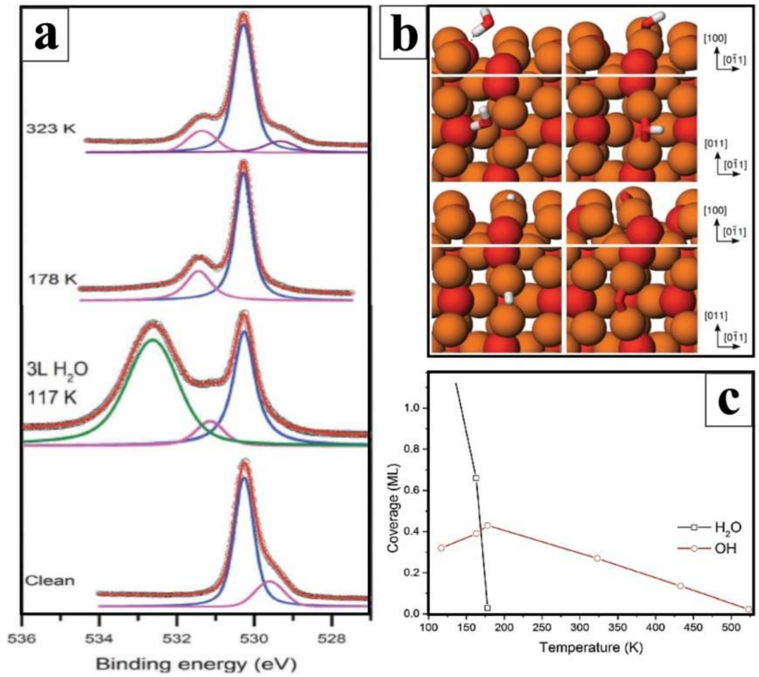

Figure 31: (a) Photoelectron spectra of O *1s* for 3 L H_2O adsorption onto $Cu_2O(100)$ at 100 K and subsequent annealing to the indicated temperatures. The clean spectrum was obtained from the surface prior to H_2O exposure. (b) Favored DFT adsorption geometries of H_2O (top left), OH (top right), H (bottom left) and O (bottom right) on $Cu_2O(100)$. (c) Estimated coverage of H_2O and OH on the $Cu_2O(100)$ surface as a function of the annealing temperature.[167]

Also, methanol adsorption was studied on the reconstructed $Cu_2O(100)$ surface by means of XPS and DFT.[149] Already at low-temperature dosage of the hydrocarbons, the XPS signature of low-coordinated surface O species disappeared, indicating a transformation of the (3,0;1,1) into an O-terminated (1×1) surface. Moreover, two new peaks emerged on the high-binding side of the O *1s* state, blue-shifted by ~1.0 and ~1.9 eV with respect to the bulk oxide peak. By means of DFT fingerprinting, they have been assigned to methoxy (CH_3O) and methanol (CH_3OH) species bound to the oxide surface, a conclusion that got further supported by an appropriate splitting of the experimental C *1s* state. While methanol desorbed from the surface already below 200 K, the methoxy species were stable up to 640 K. The findings are in good agreement with calculated adsorption energies of -1.1 eV and -2.6 eV for methanol and methoxy, respectively, with Cu-Cu bridge sites in the non-reconstructed (1×1) surface being the preferred binding positions. Interestingly, methanol dissociation was found to be unfavorable on the reconstructed (3,0;1,1) surface, explaining the observed transformation into the ideal (1×1) phase.[149] Rather similar conclusions were drawn on the basis of ethanol adsorption experiments on $Cu_2O(100)$.[168]

In a subsequent study from the same authors, the low-temperature oxidation of $Cu_2O(100)$ to CuO was monitored in a high-pressure XPS experiment.[169] In correspondence to earlier water adsorption studies, the high susceptibility of $Cu_2O(100)$ to hydroxylation was found to play a pivotal role in the oxidation reaction. CuO formation proceeds as long as hydroxyl species, arising from moisture in the rest gas, are present at the surface and correspondingly stops at monolayer CuO coverage when all OH groups are consumed. Further thickening of the CuO film via Cu_2O oxidation can only be achieved at much higher reaction temperatures, as clearly demonstrated in earlier XPS[125] and optical transmission experiments.[96]

Finally, several purely theoretical studies addressed the adsorption and reaction characteristics of the $Cu_2O(100)$ surface. As experimental verification of the proposed interaction models is still pending, we only mention those studies at this point. Rahman and coworkers explored the overall chemical reactivity of $Cu_2O(100)$, putting special emphasis on the role of low-coordinated Cu^+ surface ions and of potential CO poisoning effects during chemical reactions.[160,170] The binding behavior of water[171] and O_2 molecules[155] was addressed as well, although the (3,0;1,1) reconstruction was not taken into account in these works. Finally, photo-catalytic pathways to convert CO_2 into useful hydrocarbons on $Cu_2O(100)$ were examined in a recent study of the Muniz group.[172]

3.4. The $Cu_2O(110)$ surface

3.4.1. Termination: Theory and experiment

From all low-index Cu_2O surfaces, the (110) is the least explored one, mostly because of two reasons. In nanoparticles, the (110) surface typically takes the smallest area contribution and always coexists with sizeable (111) and (100) facets.[35,36,37,38] And, high-resolution microscopic measurements, employing either STM or TEM, have not been reported on (110)-cut single crystal surfaces up to this point. Atomic scale information on well-prepared $Cu_2O(110)$ surfaces is therefore hardly available, and given the lack of experimental input, also the amount of reliable theoretical analyses is finite.

Several research groups succeeded in preparing Cu_2O nanoparticles with dodecahedral shape, hence with a considerable contribution of (110) facets.[173,174,175] Common synthesis routes are hydro- and solvo-thermal preparations, whereby capping agents with tailored adsorption properties promote the development of the desired crystal facets, e.g. polyvinylpyrrolidone and oleic acid for (111) and (110) facets, respectively.[37,53] Scanning electron microscopy and electron diffraction data of individual (110) facets revealed a rectangular surface atomic structure, comprising a 3.0×4.3 Å^2 unit cell.[173] In an alternative approach, thick (110) oriented Cu_2O films were grown by pulsed laser deposition and plasma-assisted Cu oxidation on MgO(110) single crystals, making use of a favorable epitaxial relationship.[176,177] Although the film quality was not sufficient to gain atomic scale information, Kelvin probe and conductivity measurements provided insights into band-bending effects on this particular oxide facet.

Given the lack of high resolution measurements, truly atomic-scale insights into the $Cu_2O(110)$ surface composition still rely mostly on DFT calculations. The reference was set by the comprehensive GGA work of Stampfl and coworkers, already discussed before.[115] Based on the ideal lattice, they considered the two bulk-cut (1×1) surface terminations of mixed Cu_2O_2 and pure Cu_2 composition (Fig. 12). The by far most stable surface was the mixed Cu_2O_2 termination, comprising zig-zag rows of fourfold coordinated Cu and threefold coordinated O ions (Fig. 32a). Vertically, the topmost layer sinks into the surface by 6.3% (Fig. 32b). The Cu-terminated surface, on the other hand, is composed of $[1\bar{1}0]$ oriented Cu zigzag rows that exclusively coordinate to oxygen ions in the subsurface plane. It displays an outward relaxation of the Cu-top plane by 4.6% with respect to the bulk lattice and turns out to be less stable than the mixed termination in the whole range of oxygen chemical potentials (Fig. 32c). Structural models for both terminations, similar to those discussed above, were later derived from a DFT+U approach with the same conclusion on the high stability of the Cu_2O_2 termination.[117]

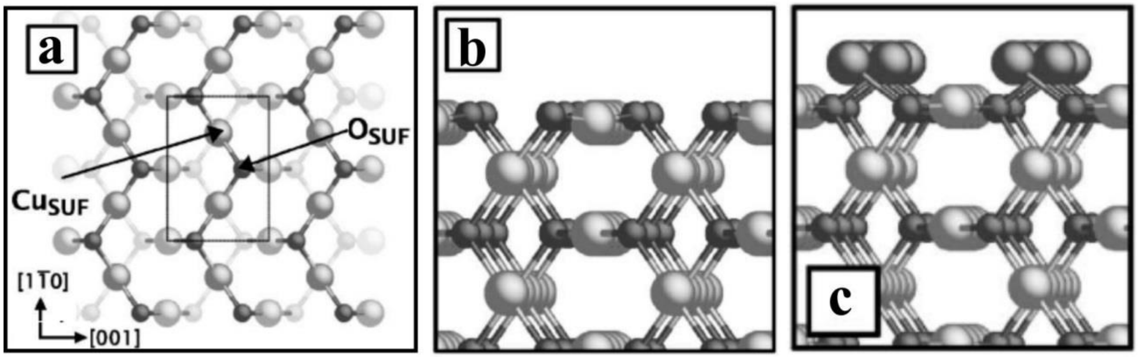

Figure 32: DFT structure models of the Cu_2O_2-terminated $Cu_2O(110)$ surface (a) top and (b) side view along $[1\bar{1}0]$. (c) Side view of the Cu-terminated $Cu_2O(110)$.[115]

Due to the alternation of layers with ±2 formal charges in the (1×1) unit cell, these two bulk-cut terminations are polar. In the absence of non-stoichiometric reorganizations, an electronic reconstruction needs to take place that involves the reduction of the surface charges by 1. As expected, the Fermi level intersects a state of mixed Cu *3d* – O *2p* character in the simulated Cu_2O_2 termination (formal charge -2), creating the hole with +1 formal charge to heal polarity.[115] In contrast, the simulated removal of either an O or a Cu atom from the topmost Cu_2O_2 layer leads to a destabilization of the termination. The modified surface composition in that case could not solve the polarity issue, as the formal charges of the surface layer become equal to 0 or -3, respectively, rather than the needed ±1 value. At the Cu-terminated surface (formal charge +2), a truly compensated configuration was obtained by removing one of the two Cu atoms in the (1×1) unit cell, as analyzed in a later DFT+U study.[132] It was found to be more stable than the Cu_2O_2 termination and exhibits a semiconducting electronic structure with a 0.3 eV wide band gap.

In absence of hints from atomically resolved experiments, theoretical simulations have been restricted to (1×1) unit cells only. Unexpected surface structures and reconstructions may well be revealed in the future, if it becomes possible to grow thick and well-ordered Cu_2O films oriented along (110).

3.4.2. Adsorption behavior and reactivity

A main motivation to study molecular adsorption on $Cu_2O(110)$ is the prospect that this oxide termination might be particularly active in thermal and photo-conversion of CO_2 into useful chemicals. So far, insights into the field were mostly gained by DFT calculations limited to unreconstructed bulk-cut surface models, either pristine or with oxygen vacancies, while experimental data are still scarce given the ill-defined nature of the oxide compounds. In a DFT study by Li et al., CO_2 activation was found to be initiated via charge transfer from the Cu_2O surface, resulting in the formation of CO_2^- anion radicals.[178] Low-coordinated Cu ions next to an O vacancy were identified as active sites in this process. In fact, CO_2 adsorption preferentially takes place to O-vacancies in the $Cu_2O(110)$ surface, whereby one O atom moves into the vacancy and the carbon coordinates to two surface Cu ions (E_B = -0.09 eV). Upon CO_2 dissociation, the O atom remains in the vacancy, while the resulting CO molecule binds with -0.63 eV to an adjacent hollow position formed by two surface Cu and one surface O atom (Fig. 33). The associated activation barrier for dissociation was calculated to be 0.25 eV, being easily accessible in thermal and photo-driven processes.[178] In the same work, the binding of atomic oxygen to $Cu_2O(110)$ was studied. Here, two preferred binding sites were identified, an asymmetric hollow position between two native surface O ions (-0.43 eV) and a bridge site located in between two subsurface Cu atoms (-0.4 eV).[178] The topic of CO_2 reduction towards methanol was addressed later again, yet with the focus on the oxide defect structure and its impact on the preferred reaction pathway.[179]

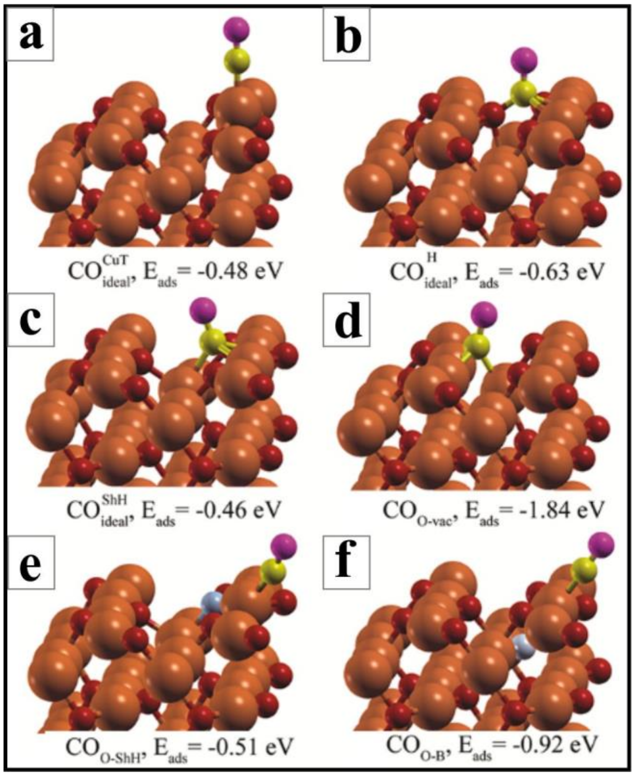

Figure 33: DFT-relaxed geometries and adsorption energies of a CO molecule on ideal and defective (110) surfaces: (a) C atom at the CuT site of the ideal surface, (b) C atom at the H site of the ideal surface, (c) C atom at the ShH site of the ideal surface, (d) C atom at the O vacancy site of the O-deficient surface, (e) C atom at the CuT site of the O-excess surface with additional O at ShH sites, (f) C atom at the CuT site of the O-excess surface with additional O at the B site. Brown and red spheres represent the Cu and O atoms of the native oxide, respectively. Yellow and purple spheres represent the C and O atoms of the adsorbed CO molecule, respectively. Blue spheres display additional O atoms on the O-excess surfaces.[178]

With a similar environmental focus, NO reduction induced by CO oxidation was theoretically explored on $Cu_2O(110)$ in a DFT+U approach.[180] The NO preferentially binds with the N-terminal to Cu−Cu bridge sites on protruding chains of the Cu-O termination, adopting an adsorption energy of −0.76 eV. The CO, on the other hand, bridges two Cu-O chains, with the C atom simultaneously coordinating to an O ion in one chain and a Cu ion in the adjacent one (E_B = -0.34 eV). For both molecules, the binding energy more than triples in presence of surface O defects, whereby either the N or C terminal enters the vacancy site, respectively. The NO reduction via CO oxidation now follows a multistep reaction, proceeding via CO_2 plus O_{vac} formation according to an Eley-Rideal mechanism, NO splitting by annihilating the O vacancy, assembling the N adatom with a second NO, and dissociating the so generated NO_2 via an O_{vac} mediated process into desorbing N_2 and atomic oxygen filling the vacancy. Although the overall process is exothermic, a number of energetically unfavorable transition states need to be populated in the reaction course.[180] Similarly, DFT calculations on water interacting with Cu_2O(110) revealed only weak adsorption (E_B = -0.39 eV) and a small trend towards dissociation in absence of structural defects in the oxide surface.[181] Finally, the adsorption of more complex organic molecules, such as chlorophenol,[182] bromobenzene and aniline,[183] to Cu_2O(110) was studied in a number of DFT calculations. Obviously, all these theoretical results should be considered as tentative, since they rely on assumed compositions and atomic structures of bulk-cut surface models on which the reactions would take place.

4. Optical properties of cuprous oxide

The optical behavior of bulk Cu_2O has been extensively studied in the past decades and a plethora of publications is available on this topic.[20,184] As the surface properties of Cu_2O stand in the center of this review, we will only summarize the most relevant bulk aspects here and focus on means to study the optical characteristics of Cu_2O surfaces in the main part of this section.

4.1. Optical properties of bulk Cu_2O

Bulk cuprous oxide has a direct, yet dipole forbidden band gap of 2.15 eV, which compares to 1.35 eV for cupric oxide.[1] Four fundamental optical transitions involving the spin-orbit split VB and CB can be detected across the Cu_2O band gap (Fig. 34a).[185] They are named according to their central absorption wavelength as yellow, green, blue and indigo series (Fig. 34b). Hereby, especially the yellow series stands in the focus of research, as it supports two fundamental types of excitons, the para- and ortho-exciton.[186] While the former has singlet character, i.e., an opposite spin orientation for electron and hole, the latter is of triplet nature, hence the effective electron and hole spins are parallel to each other. Consequently, there is a spin barrier for radiative recombination of the para- but not for the ortho-excitons. Due to the relatively small dielectric screening in Cu_2O, both excitons are characterized by large ground-state binding energies of about 140 meV and relatively small exciton radii (7 Å).[187] Para-excitons are 12 meV more stable than their ortho-counterparts, reflecting the impact of spin exchange. Both Cu_2O excitons have an optically dark *1s* ground state, as the hot electron resides in a Cu 4s derived state at the CB edge, while the hole locates in states with Cu *3d* character at the VB top. The difference in orbital momentum quantum number of the two states thus amounts to $\Delta l = 2$, rendering radiative exciton decay dipole forbidden. Nonetheless, a weak luminescence peak at 610 nm wavelength, arising from the recombination of 1s ortho-excitons (X_0) can be detected in bulk Cu_2O at 4.2 K (Fig. 34c).[26] The involvement of phonons in exciton recombination partially releases the dipole selection rules for ortho-excitons, resulting in various phonon-assisted luminescence bands in Cu_2O, with the negative-parity Γ_{25}^-, Γ_{15}^-, Γ_{12}^- and Γ_2^- phonons producing the highest emission yields (Fig. 34c). For the Γ_{12}^- phonon of 13.6 meV energy, the competition between Stokes ($X_0 - \Gamma_{12}^-$) and Antistokes processes ($X_0 + \Gamma_{12}^-$) has been analyzed to obtain an internal measure of the oxide temperature upon laser excitation.[187] Para-excitons remain optically dark even under phonon involvement, given the prohibitive spin constraint.

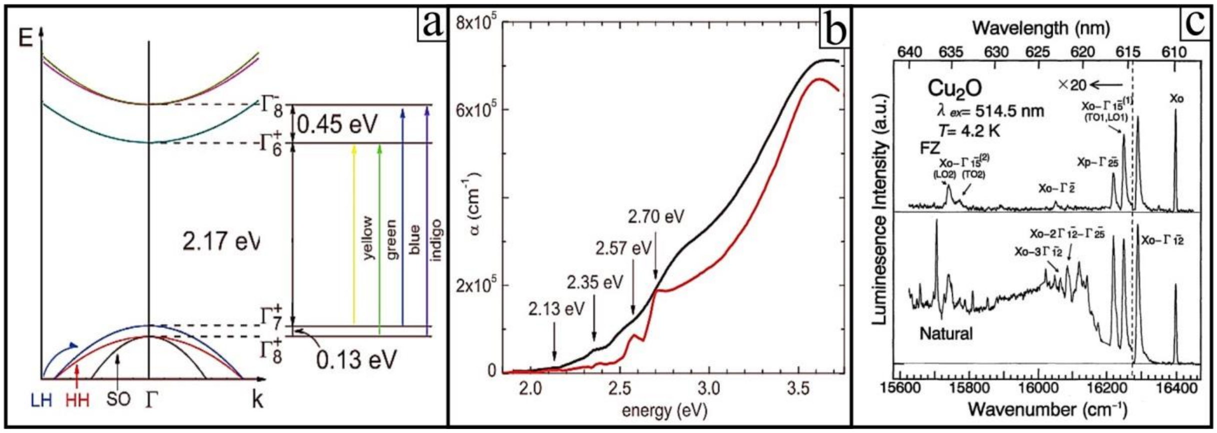

Figure 34: (a) Energy-band diagram of Cu_2O around the Γ-point. Possible interband transitions and the underlying band splittings are shown in the inset. (b) Absorption spectra of an as-grown Cu_2O film (black line) and a film annealed at 930°C (red line). The edges of the different exciton series are marked by arrows.[1] (c) Contributions of different lattice phonons to the radiative decay of Cu_2O ortho-excitons from the yellow series. The zero-phonon line (X_o) is relatively weak.[26]

The dipole forbidden nature of the Cu_2O band gap is also responsible for long decay times of the oxide excitons, reaching more than 500 ns for para-excitons at 20 K.[23,188] With ~15 ns, the lifetime of ortho-excitons is much shorter, as those effectively convert to para-excitons via spin-flip scattering.[17,24] Long lifetimes promote the observation of Cu_2O excitons in high Rydberg states, even if the underlying Rydberg energy of 92 meV is smaller than the ground-state exciton binding energy.[26,189] In fact, excitons up to the 25th Rydberg level could be detected in natural Cu_2O crystals at 1.2 K (Fig. 3), whereby the mean exciton diameter increases from ~1 nm to ~1 µm when going from the 2nd to the 25th excited state.[18] The large spatial extension renders Rydberg excitons particularly susceptible to perturbations by external electric fields, as reflected in the splitting of the n^th exciton peak in n-field dependent sub-states.[190] Moreover, excitons with high angular momentum could be detected, demonstrating small deviations of the Cu_2O lattice from ideal cubic symmetry.[142] Finally, long exciton lifetimes make Cu_2O crystals an ideal model system to study Bose-Einstein condensation of excitons.[20] As the critical phase-transition temperature depends on the exciton density to the power of 2/3, especially the long lived para-excitons seem ideally suited to observe exciton condensates at experimentally accessible temperatures.[19] Although heavily explored in the past 30 years, unambiguous evidence for Bose-Einstein condensation of excitons could not be provided so far. The main obstacle is the so-called Auger decay of excitons that leads to a dramatic decrease of the exciton lifetime at high exciton densities.[17] In that process, two excitons collide whereby the first one recombines while the second decays into two unbound carriers. The associated lifetime τ scales with the inverse exciton density times the Auger constant $A = 7\times10^{-17}$ cm^3/ns that is particularly large in Cu_2O.[21] Very recent experiments suggest that Bose-Einstein condensation of Cu_2O excitons may nonetheless be observable at very low temperatures of about 500 mK.[20,191]

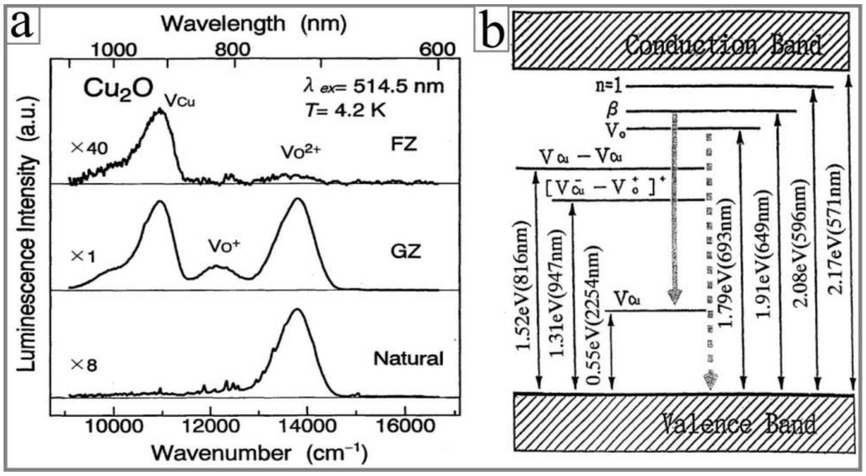

Figure 35: (a) Defect luminescence measured for three Cu_2O crystals by photo-luminescence spectroscopy. (b) Electron recombination scheme across the Cu_2O band gap, highlighting the role of the different Cu_2O defects for the observed luminescence.[26]

In addition to excitonic modes, two defect-mediated luminescence channels should be discussed in the context of Cu_2O bulk crystals (Fig. 35a). The first one relates to Cu vacancies, being the main defect type in Cu_2O due to their low formation energy and responsible for the p-type conductivity of the material.[7] The associated acceptor states are located 0.2-0.4 eV above the VB edge, whereby the scattering arises from different defect configurations (simple or split Cu vacancies) and variations in the overall sample quality.[11,13,192] The initial and final state for defect recombination are now trapped Cu_2O excitons and the acceptor level inside the band gap, explaining the sizeable redshift of the V_{Cu} emission with respect to the free exciton (920 versus 610 nm) (Fig. 35b). In fact, V_{Cu}-mediated emission bands are prominently detected in Cu_2O crystals and high-quality films, reflecting the abundance of such defects in the p-type oxide.[10,26] Conversely, the V_{Cu} band is often suppressed in materials with poor crystalline order due to an abundance of non-radiative decay channels. The correlation between crystalline order, radiative lifetime and luminescence response for different Cu_2O emission channels is discussed in detail in the next section.

The other prominent defect luminescence arises from O vacancies in the Cu_2O lattice (Fig. 35a). Also here, two defect configurations are distinguishable, a double- (V_O^{2+}) and a single-positively charged vacancy (V_O^{+}), producing two emission bands at ~750 and 850 nm, respectively.[26,193,194] While in the former case, the two electrons left behind by the desorbing oxygen species are annihilated by two holes from the p-type conductor, one excess electron remains in the defect site in the second case. The two charge states give rise to different initial-state energies of the V_O transition, both located just below the CB edge.[195,196] The final state is always a hole in the oxide VB around the Fermi energy. From the intensity ratio of the two V_O-related emission bands, conclusions on the degree of p-type conductivity of the respective Cu_2O samples can be drawn. In contrast to the V_{Cu} luminescence, the V_O-related channels are less sensitive to structural disorder and prevail also in thin films and powder samples, as shown in the next chapter.

Detailed insights into the time-dependent optical properties of Cu_2O crystals were provided by transient optical experiments and, more recently, by pump-probe techniques. Already early approaches revealed a radiative lifetime of the ortho-excitons of 10-15 ns, limited by their effective conversion to optically dark para-excitons.[186] The para-excitons, on the other hand, decay mostly via defect scattering on a time scale of 500 ns at low temperature.[23,188] For the radiative lifetime of the Cu_2O defect luminescence, two different regimes have been identified. While V_O luminescence decays within 3 ps, the radiative lifetime of the V_{Cu} emission is almost 50× longer.[197] The deviating response reflects different stimulation schemes of the defects. The V_O excitation mostly happens via free carriers in the oxide CB, giving rise to short decay times. Conversely, V_{Cu} defects are excited by mobile excitons and consequently mimic their long radiative lifetime. Moreover, the decay time of the V_O luminescence exhibits a large temperature dependence and decreases to zero above 100 K, when the optical recombination channel gets blocked. The radiative lifetime of V_{Cu} defects, on the other hand, only moderately depends on temperature.[26]

Finally, the promising role of Cu_2O as cathode material for photoelectrochemical (PEC) splitting of water shall be highlighted here. In contrast to standard oxide materials used for this purpose, Cu_2O has a number of advantages. Its band alignment is perfectly suited to sustain both, the hydrogen and oxygen evolution reaction.[198] The Cu_2O band gap is smaller than that of typical photo-catalysts, such as TiO_2 or ZnO, and a larger portion of the solar radiation can thus be harvested. And, optical stimulation gives rise to long lived excitonic states, suitable to promote PEC water splitting. The main disadvantage of the oxide material is its low stability in a liquid environment, especially at acid conditions far away from the point of zero charge. The reason is the Cu^+ to Cu^0 reduction potential that directly overlaps with the potential range of water spitting, and leads to Cu_2O decomposition during the PEC reaction.[199] Hereby, Cu_2O(100) and (110) facets exhibit lower stability than their (111) counterparts, explaining the dramatic reshaping in favor of (111) crystal terminations observed for Cu_2O nanoparticles.[200] The consequence is a continuous decline of the reaction rate during a PEC process. Many attempts have been made to overcome this problem, for example, by stabilizing the Cu_2O surface with ultrathin protective layers of ZnO or SiO_2,[201] or by adding metallic copper as a reservoir to maintain the oxide stoichiometry.[202] However, none of these approaches convincingly resolved the stability issues of Cu_2O and technologically matured solutions for using Cu_2O as cathode material in PEC water splitting are not in sight so far. The next section sheds light on experimental techniques to explicitly probe the optical response of Cu_2O surfaces with the aim to correlate structural and optical properties with high spatial and spectral resolution.

4.2. Optical properties of Cu_2O thin-films and surfaces

In many aspects, oxide thin films grown on single-crystalline metal supports turned out to be versatile model systems to explore the physics and chemistry of the respective bulk materials.[203,204,205] Especially surface properties, such as the thermodynamic preference for certain terminations, the adsorption behavior, or the occurrence of surface states, are perfectly reproduced in oxide films even of reduced thickness. However, large deviations are revealed when it comes to the optical response of low-dimensional oxides, reflecting the susceptibility of optical excitations to structural disorder and non-radiative decay channels. The effect is particularly strong for Cu_2O films and powders, due to the long lifetime and high diffusivity of the underlying excitonic modes. To demonstrate the impact of reduced dimensionality, the low-temperature luminescence of Cu_2O/Pt(111) and Cu_2O/Au(111) thin films will be compared with the one of single crystals in the following.[124] While both systems show identical behavior regarding chemical composition, diffraction pattern, electronic response and surface termination, their photoluminescence (PL) upon 532 nm laser irradiation is distinctively different (Fig. 36).

The bulk crystal features the characteristic optical bands discussed in section 4.1, namely an asymmetric peak at 620 nm due to phonon-assisted exciton decay, as well as two defect peaks at 730 and 920 nm related to oxygen and copper vacancies in the lattice, respectively.[26] All three emission channels come with their own temperature dependence (Fig. 36d). The probability for radiative recombination of ortho-excitons rises with decreasing temperature, as thermal exciton-breakup into unbound electrons and holes becomes increasingly unlikely. The trend reverses at ~125 K, when the ortho-excitons transform into non-radiative para-excitons that are lower in energy.[17] The V_O related emission channel only opens below 230 K, as electrons are back-promoted from the defect state into the CB at higher temperature. For the V_{Cu} decay, on the other hand, the final state gets blocked by thermal electrons from the VB, resulting in a decreasing emission yield at increasing temperature again.[26,188] The coexistence of Cu and O vacancies in the lattice hereby indicates incomplete equilibration of the two fundamental defect types in natural crystals.[192]

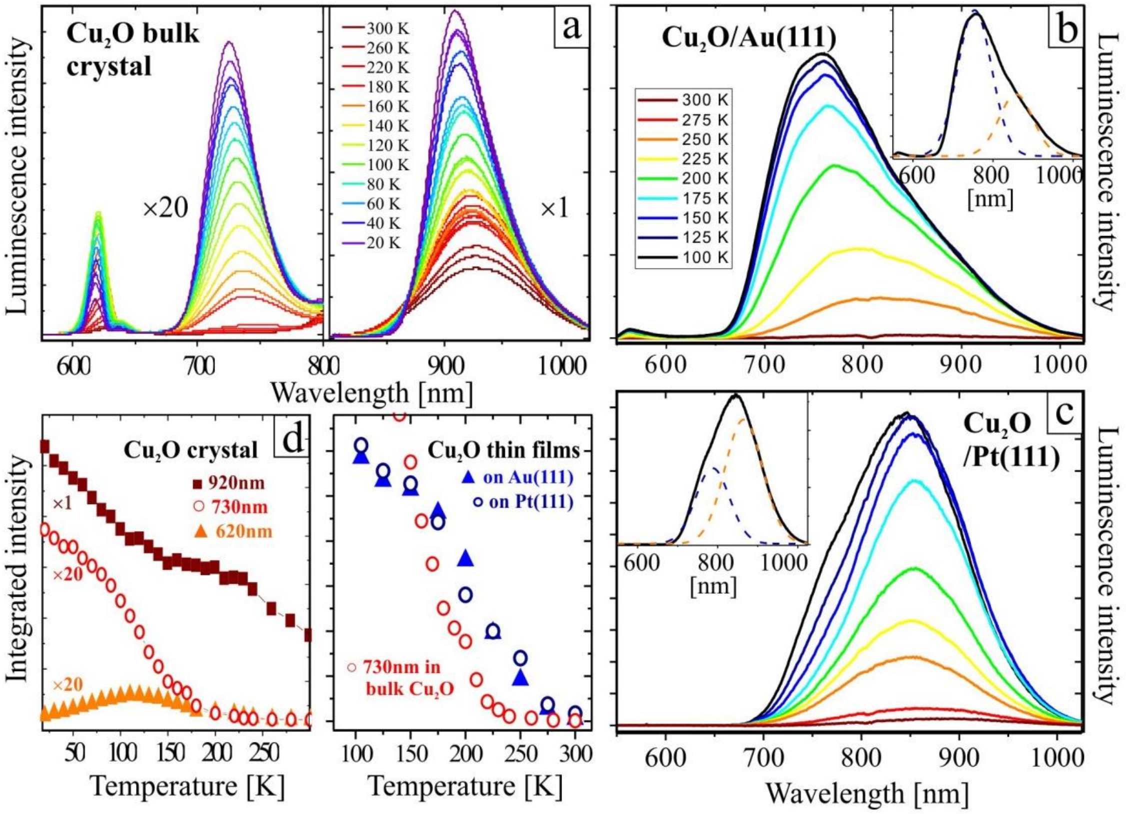

Figure 36: Temperature-dependent PL spectra of (a) a Cu_2O crystal and (b) 65 nm Cu_2O films grown on Au(111) and (c) Pt(111) substrates. The insets in (b) and (c) show the deconvolution of the emission into two maxima centered at 750 and 850 nm. (d) Evolution of the integral intensity with temperature for the various emission bands observed on Cu_2O bulk (left) and thin films (right).[124]

The luminescence response of Cu_2O films is distinctively different, not only in the experiment described in Ref. 124, but also in numerous other studies on thin-film and powder samples.[193,194,206] The films discussed here were 65 nm thick, hence bulk-compatible, and deposited onto Pt(111) and Au(111) supports with matching lattice parameters. The corresponding PL spectra are governed by an asymmetric band between 700 and 900 nm that can be de-convoluted into two maxima centered at ~750 and ~850 nm, respectively (Fig. 36b,c). While the short-wavelength peak dominates for Au(111) supported films, the long-wavelength one governs the Cu_2O/Pt(111) emission. Following the earlier discussion, the 750 nm maximum corresponds to an optical recombination channel mediated by double-charged oxygen vacancies (V_O2+), while the redshifted peak at 850 nm is induced by its single-charged counterpart (V_O+).[195] This interpretation is further supported by the temperature-dependent emission yield that follows the one observed for V_O emission from bulk crystals (Fig. 36d). According to the stronger V_O2+ emission, the Cu_2O/Au(111) films have more p-type character, as more holes are available to annihilate the excess electrons left behind by the desorbing O species. Conversely, the Pt(111) supported films exhibit a reduced hole concentration, and statistically one electron survives in the vacancy. The deviating behavior reflects the larger tendency for copper/gold alloying, producing a sink for Cu atoms on Au(111) that does not exist on the Pt substrate.[84] The Au(111) supported films have consequently a higher Cu-deficiency and are more p-type, rationalizing their different optical response (Fig. 36).[124]

Even more interesting is the absence of the free-exciton and V_{Cu}-related emission for Cu_2O films, although both are prominently detected for oxide single crystals. This observation is commonly linked to the reduced crystallinity of low-dimensional oxides but provides interesting insights into the nature of optical transitions in Cu_2O as well. As summarized in section 4.1, band-gap transitions in Cu_2O are dipole forbidden, which gives rise to long radiative lifetimes and large diffusion lengths of the oxide excitons.[23,25,188] These optical modes have thus a high probability to undergo non-radiative recombination, especially at the surface / interface of Cu_2O nanocrystals and films, which is why the free-exciton emission is largely suppressed in those systems. The same holds for the V_{Cu} emission, as exciton trapping at Cu vacancies forms the initial state for optical recombination also in this case. The V_O luminescence, on the other hand, is mediated by hot electrons in the oxide CB and no exciton formation is required here. Moreover, the radiative lifetime of the O-vacancy channel is substantially shorter than the exciton mediated pathway (3 ps versus ~100 ns at low temperature), which renders the former less sensitive to defects and structural disorder.[188,197] Given this asymmetry, the luminescence of Cu_2O films and nanocrystals is almost entirely governed by O defects, as clearly discernable in the PL spectra of Fig. 36.

In addition, pump-probe techniques were employed to investigate the transient optical response of Cu_2O surfaces.[129,207] In a first experiment on $Cu_2O(100)$, electrons were stimulated across the band gap with 2.5 eV pump pulses and the resulting electron population was interrogated after a given time delay with 4.5 eV probe pulses (Fig. 37a).[207] Surprisingly, the CB population decayed within 200 fs at the expense of a sizeable in-gap electron population centered at ~1.5 eV above the VB top. Only a lower lifetime limit of ~1 ns could be determined for electrons in this gap state. Moreover, the trapping was blocked after depositing a Pt ad-layer onto the oxide, suggesting that the relevant gap states are located close to the surface (Fig. 37b). The nature of these defect states was tentatively related to Cu vacancies, although the measured energy position obviously deviates from calculated level energies of the V_{Cu} defects.[7,11,12] In a second experiment, the time-resolved optical response of a $(\sqrt{3}\times\sqrt{3})$-reconstructed $Cu_2O(111)$ surface was probed.[129] Also here, ultrafast trapping of conduction electrons in a defect state was detected, in which they remained for more than 100 ps with negligible population decay. The position of the trap state was determined to 0.2-0.4 eV above the VB top, hence much lower than on $Cu_2O(100)$ and close to the anticipated V_{Cu} defect state.[11,12] Nonetheless, it was assigned to a lower resonance induced by O vacancies in the Cu_2O matrix by means of hybrid DFT calculations.[129,195] The presence of O defects in the $(\sqrt{3}\times\sqrt{3})$ reconstructed surface was rationalized with a downward band-bending detected by XPS. Note that an upward band-shift was revealed for the thermodynamically preferred nano-pyramidal (√3×√3) reconstruction discussed earlier,[114] and the true nature of the $Cu_2O(111)$ surface probed in that study remained ambiguous. Surprisingly, no defect-trapping occurred for the non-reconstructed (1×1) surface and a sizeable population of CB electrons could be detected there even 10 ps after excitation.[129]

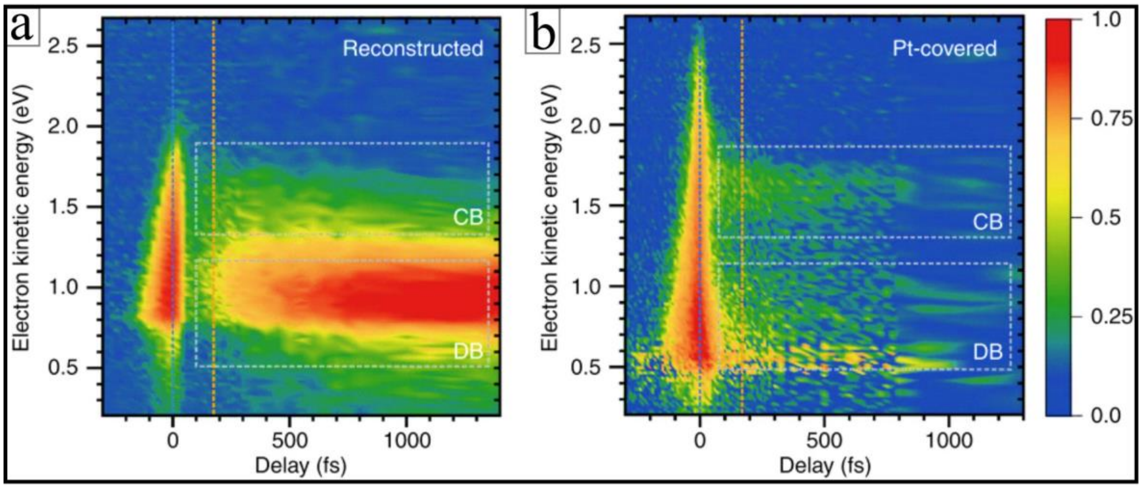

Figure 37: Color maps of the transient two-photon-photon-emission from (a) the reconstructed $Cu_2O(100)$ surface and (b) the Pt-covered oxide. The plots show the dependence of the electron kinetic energy on pump-probe delay.[207]

By exploiting the capabilities of PEEM to follow excitation processes with high spatial and temporal resolution, charge transfer processes within single Cu_2O nanocrystals could be detected with unmatched precision in Ref. 40. Following Wulff's construction principle, the crystallites developed truncated pyramidal shapes, exposing large (111)-oriented side facets and a (100) top plane (Fig. 5). After excitation with 2.4 eV pump pulses, the evolution of the charge distribution within the particle could be detected in real time, revealing a net electron transfer from (111) to (100) facets. Electric-field and work-function effects were identified as driving forces for this charge flow. Its relevance for photochemical applications was proven by correlating the induced photo-voltage measured on the Cu_2O crystallites with the efficiency of the hydrogen-evolution reaction.[40]

The above paragraph underlined how structural, optical and chemical properties of Cu_2O closely interfere at the nanometer scale, and should consequently be probed simultaneously within one spatially resolving experiment. In the following section, we therefore discuss the optical properties of Cu_2O surfaces as probed with STM luminescence spectroscopy at the atomic scale.

4.3. Spatially resolved optical measurements on Cu_2O surfaces

The optical response of dielectric materials exhibits pronounced spatial inhomogeneity, arising from the presence of structural defects and their ability to trap mobile optical modes, such as excitons. In the case of Cu_2O, optical inhomogeneity originates from O and Cu vacancies in the lattice, as well as from grain boundaries and line defects in polycrystalline materials.[1,26] The variable thickness of oxide films introduces another source of spatially inhomogeneous optical signals.[208] Given the fundamental wave-character of light, conventional optical spectroscopy is intrinsically unable to record nanometer spatial variations in the luminescence response, as clearly stated in Abbes diffraction limit. To achieve spatial resolution well below the wavelength of visible light, nearfield optical techniques can be employed, such as scanning near-field optical microscopy (SNOM) and STM luminescence spectroscopy.[209,210] In both cases, the strong electromagnetic field-enhancement inside the tip-sample cavity and the symmetry breaking due to the sensor tip enable coupling to evanescent waves in the microscope gap.[211] Detection of these wave components in the far-field now yields optical information on a sub-nanometer length scale, sufficient to probe light emission from individual oxide defects.

In the context of cuprous oxide, STM luminescence spectroscopy at 100 K was employed to probe the local emission response from $Cu_2O(111)$ surfaces. In the case of bulk crystals, STM luminescence has been triggered by injecting electrons from the tip into the oxide CB (Fig. 38).[212] The photon flux sets in at ~2.5 V sample bias, corresponding to the band onset, and monotonously rises with voltage due to Auger-type excitations. The injected electrons then recombine with holes at the VB top of the p-type conductor, whereby different decay channels give rise to different wavelength maxima in the STM luminescence spectra (Fig. 38 a,b). The by far most intense peak is at 920 nm and matches a similar peak in the PL data, where it was assigned to Cu vacancies in the lattice (see Fig. 36a). Also, the V_O-mediated and the free-exciton peak are discernable at 750 and 620 nm, respectively, yet with strongly reduced intensity compared to the V_{Cu} emission. The largely different weights of V_{Cu}, V_O and excitonic peaks in photo- and STM luminescence spectra reflect the deviating excitation schemes that involve electron-hole pairs in PL but hot electrons injected from the tip in the STM studies (Fig. 38b). In the latter case, the CB electrons can directly decay towards E_F via Cu vacancy states without forming an exciton first, explaining the dominance of the V_{Cu}-induced emission.[212]

STM luminescence spectroscopy provides the unique possibility to probe optical signals with nanometer spatial resolution. For this purpose, the tip is scanned across the surface and the emitted light is probed with a sensitive photomultiplier in the far-field.[213] Such photon maps acquired on bulk $Cu_2O(111)$ display high overall intensity but hardly any spatial modulations of the emission yield, a finding that is independent of tunneling current and bias voltage (Fig. 38c).[212] The result is especially surprising, as the most intense emission peak was spectrally assigned to Cu vacancies and should thus arise from local emission centers in the surface (Fig. 38a). The missing correlation between defect landscape and optical response can be explained, however, with the long excitation lifetime in Cu_2O. In fact, electrons injected into the oxide CB can migrate over large distances before they decay via Cu vacancies in the lattice.[20] As a consequence, any spatial correlation between the point of electron injection and the point of radiative decay is lost and the respective optical maps exhibit homogenous emission intensity. To identify local optical centers in the surface, the mobility of the excited modes needs to be reduced, for instance by performing experiments at even lower temperature. Successful STM luminescence studies with single-defect resolution were reported for dielectrics with dipole-allowed optical transitions and short radiative lifetimes, for example for GaAs and Eu-doped MgO.[214,215] As thin films have naturally a lower lattice quality than bulk crystals, STM photon maps of Cu_2O layers also revealed pronounced spatial variations, as shown next.

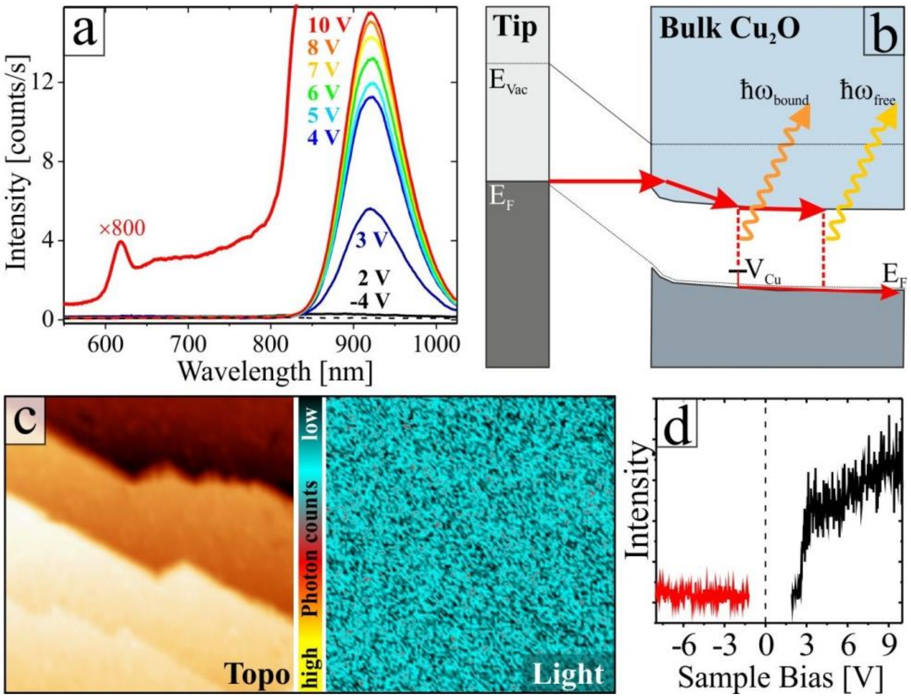

Figure 38: (a) Bias-dependent STM luminescence spectra acquired on bulk $Cu_2O(111)$ (acquisition time 60s, 0.25 nA). (b) Underlying emission mechanism in the STM. The requirement for photon emission is electron injection from the STM tip into the oxide CB. (c) STM photon map of $Cu_2O(111)$ (150×150 nm^2, 4.4 V, 0.25 nA). The spatially homogenous nature of the emission reflects the high mobility of optical modes in the oxide surface. (d) Integral emission intensity measured as a function of bias voltage with a photomultiplier tube.[212]

Respective STM studies have been performed on Cu_2O/Au(111) films, and spatially modulated luminescence maps were indeed detected although the emission mechanism was distinctively different from the one on bulk crystals.[212,216] For Cu_2O/Au(111) thin films, STM luminescence could be recorded at both bias polarities, i.e., for tunneling into the CB and out of the VB (Fig. 39). Spectrally, both tunneling directions gave rise to the same emission envelop, namely a broad maximum extending from 700 to 950 nm. In contrast, the emission fine structure, i.e., the number and position of individual peaks was found to depend on the nature of the STM tip used in the experiments.[217] Both peculiarities, a polarity independent spectral signature and the critical role of the sensor tip, identified the emission mechanism to be governed by plasmon modes in the tip-sample cavitiy.[210,211] In the experiment, the plasmons are sustained by coherent oscillations of the free electron gases in the gold tip and the gold sample below the oxide film, generating a field-enhancement window between 700-950 nm in agreement with the detected emission response (Fig. 39b). The Cu_2O film, on the other hand, has low carrier density and, apart from a small redshift due to its intrinsic polarizability, contributes only little to these cavity plasmons.[208] Its intrinsic optical modes thus remain invisible, also because the Cu_2O excitons have much longer radiative lifetimes and much lower oscillator strength than the STM cavity plasmons.[216]

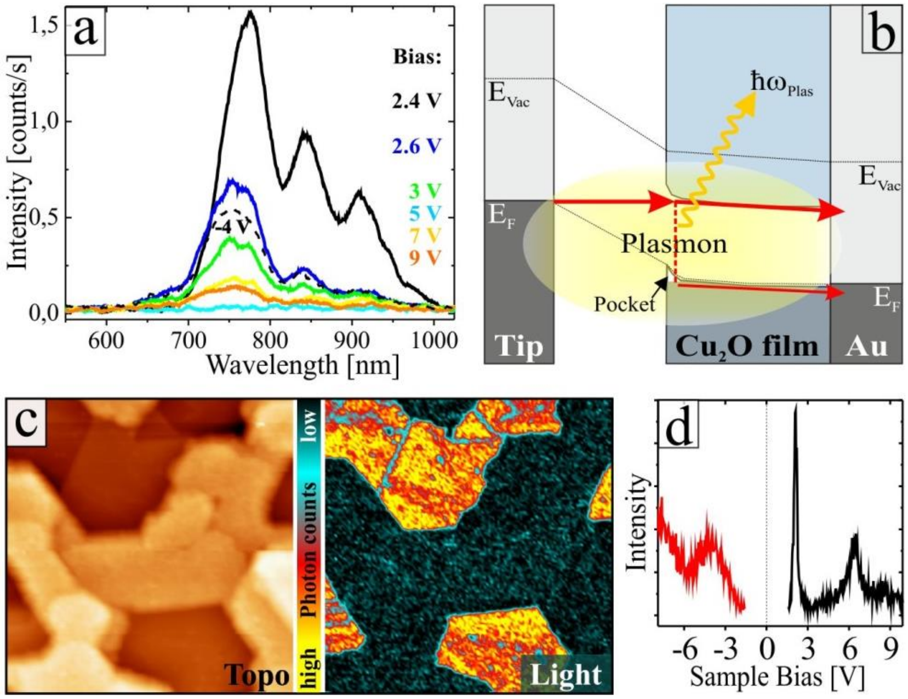

Figure 39: (a) Bias-dependent STM luminescence spectra acquired on Cu_2O/Au(111) films (acquisition time 60s, 1.0 nA). The spectral response is independent of bias polarity in this case. (b) Emission mechanism governed by the excitation of cavity plasmons in the STM gap. (c) STM photon map of a Cu_2O/Au(111) film (150×150 nm^2, 5.5 V, 1.0 nA). At the selected bias, the emission involves field emission resonances and distinctively deviates for a Cu_3O_2 surface oxide (bright) and thick Cu_2O patches (dark). (d) Integral emission intensity measured as a function of bias voltage with a photomultiplier tube.[212]

The bias-dependence of the luminescence yield perfectly corroborates the above emission scenario (Fig. 39d). At negative polarity, the detected intensity runs through a maximum at -4 V, slightly dependent on the oxide thickness. It can be linked to an emission channel, where electrons start from E_F in the Au(111) support, proceed to the oxide CB that bends downward in the tip-electric field, and recombine with holes in the VB via plasmon excitation. At positive polarity, the emission gets initiated at 2.5 V when electrons populate the CB and decay from there to the VB via plasmon stimulation. An additional maximum is detected at ~6.0 V that can be assigned to electron recombination via field emission resonances. The latter are bound electronic states in the classical part of the tip-sample junction with energies depending on the local work function.[218] Electrons trapped in such high-bias resonances have long lifetimes, making them ideally suited for plasmon stimulation via inelastic energy losses.[219] Moreover, a distinct work-function dependence makes this emission channel sensitive to the oxide film thickness, and produces the pronounced contrast seen in the STM photon maps (Fig. 39c). Hereby, a Cu_3O_2 monolayer film that can be viewed as oxide precursor on Au(111) exhibits the lowest work function and consequently appears bright already in photon maps taken at 5.5 V.[82] For thicker films, the resonance condition gets fulfilled at higher bias and those turn bright only in maps taken above 6.0 V.[213] In clear difference to bulk crystals, photon maps of Cu_2O films thus exhibit a pronounced thickness-dependent contrast, although the associated emission channel contains no direct information on the Cu_2O optical modes.

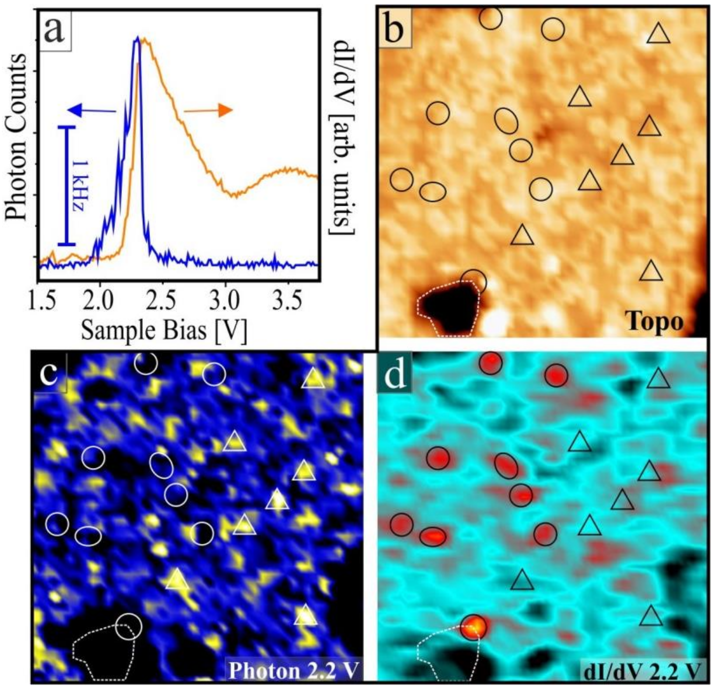

Figure 40: (a) Bias-dependent STM luminescence yield measured with a photomultiplier tube and simultaneously detected dI/dV signal for a Cu_2O/Au(111) thin film. The luminescence maximum corresponds to an excitation energy inside the band gap. (b) Topography, (c) photon- and (d) dI/dV-map of the film taken at 2.2 V (25×25 nm^2, I = 1 nA). Characteristic luminescence (triangles) and electronic spots (ellipses) do not coincide with topographic features in the surface, suggesting that the relevant emission centers correspond to single V_O defects in subsurface positions.[217]

Incompatible with the plasmon-picture developed above, the thin-film luminescence runs through a sharp intensity maximum at 2.1 V that is higher than at any other excitation bias and exhibits only 100 mV half width (Fig. 40a).[217] Surprisingly, the respective bias position lies inside the Cu_2O band gap, as the CB only starts at 2.3 eV, as deduced from a sharp increase in the differential conductance. Although the spectral signature still indicates cavity plasmons as source of the light emission, the resonance-like maximum points to an excitation pathway linked to the Cu_2O electronic structure. Using hybrid DFT calculations, this path has been assigned to resonant tunneling into defect states introduced by oxygen vacancies. Their energy positions were determined to 1.7 and 1.6 eV above the VB top for V_{O2+} and V_{O+} defects, respectively, although only V_{O2+} defects are of relevance for Cu_2O/Au(111) films with their pronounced p-type nature.[195] The calculated defect energy is therefore 0.4 V lower than the experimental resonance position (2.1 V), a discrepancy that can be explained however with band-bending effects in the tip-sample junction of the STM.[217] In fact the upshift of the resonance can be reproduced with a plate-capacitor model that takes the oxide thickness (10 nm) and the Cu_2O dielectric constant ($\varepsilon_r = 7.1$) into account.[220] The defect-mediated excitation scenario also explains the high efficiency of the emission channel, as elastic electron transport into CB states is prohibited at the bias voltage inside the band gap. Conversely, an inelastic transport channel into the VB remains accessible, generating the bright photon emission observed in the measurements (Fig. 40a). The small FWHM of the resonance of 100 meV finally results from the intrinsic width of the gap state convoluted with a distribution of V_O defects in different layers below the oxide surface.[217]

The luminescence from V_O defects leaves sharp and discernible fingerprints also in photon maps acquired from metal-supported Cu_2O films.[217] Their high spatial localization can be rationalized with the fact that once electrons have been injected into a discrete defect state, no diffusive motion of the mode is possible anymore and radiative decay occurs directly at the point of excitation. Consequently, the photon maps taken at 2.1-2.2 V sample bias are highly inhomogeneous in space, with sharp, localized emission centers alternating with dark regions (Fig. 40 b,c). The optical centers are randomly distributed in the surface and have a mean diameter of ~1 nm, although some centers exhibit non-spherical shapes due to agglomeration effects. Following the above discussion, the local emission spots can safely be assigned to single oxygen vacancies in the Cu_2O films. The assignment is strengthened by the observation that they disappear from the maps if electrons are injected into delocalized conduction states at higher bias. Interestingly, simultaneously recorded topographic and dI/dV maps do not show common features with the photon maps, as visualized by triangles (for luminescence maxima) and ellipses (for electronic features) in panels (c) and (d) of Fig. 40. Apparently, the O vacancies cannot be recognized in the topographic maps, indicating a position below the oxide surface. This finding agrees well with the theoretical prediction that O vacancies are instable in the Cu_2O(111) surface and tend to move deeper into the oxide matrix.[114,128] The electronic and optical features appear uncorrelated as well, i.e., regions with pronounced optical and electronic activity do not coincide. This is in perfect agreement with the proposed emission mechanism, in which V_O luminescence relies on inelastic electron transport, while the dI/dV channel probes elastic electron exchange between tip and sample.[217] The detection of single V_O defects via STM luminescence thus arises from a fortunate interplay of effective inelastic tunneling via plasmon stimulation in absence of elastic transport paths.

The observation of single-defect luminescence in Cu_2O is unprecedented and has not been reported for any other dielectric oxides so far. Given the pivotal role of cationic and anionic defects for controlling oxide properties, the possibility to identify individual defects in the surface region is expected to gain much more attention in the future. In fact, Cu_2O is far from being ideal for this kind of measurements, as the dark character of ground-state excitons hampers their observation in STM luminescence maps. Consequently, the technique may produce even more promising results if an oxide with direct band gap, such as ZnO, is used in the experiments.

5. Doping of Cu_2O surfaces

In the final chapter of this review article, we discuss possibilities to modify surface and bulk properties of cuprous oxide by inserting foreign atoms. Hereby, cationic (metal ions) and anionic (nitrogen) dopants will be considered, and both experimental and theoretical viewpoints will be compiled. We will start our discussion with nitrogen doping of cuprous oxide, as this approach has gained much attention in the literature as a means to increase the conductivity and p-type character of the oxide material.

5.1. Nitrogen-doping

Two main scenarios have been considered on how nitrogen gets introduced into the Cu_2O lattice.[15] In the first case, a nitrogen atom substitutes a lattice-oxygen species, producing a so called N_O defect (Fig. 41a). In a purely ionic picture, the dopant would trap an extra electron from nearby Cu ions, which increases the number of hole states in the VB and thus promotes the p-type character of the material. In a second scenario, a lattice Cu gets replaced by an N_2 molecule, $(N_2)_{Cu}$, which introduces a new low-lying acceptor state in the band gap and thus increases the oxide conductivity at low temperature (Fig. 41b). The thermodynamic preference for one or the model is subject of intense discussions already for several years.

The N_O substitution scenario has been theoretically addressed first in a DFT / CASTEP study.[221] The authors find an unoccupied and spin-polarized in-gap resonance that has mostly N *2p* character and locates at 0.9 eV above the VB top. Although the Bader charge on the N atom is increased by 12% with respect to the initial oxygen, no complete charge transfer is revealed and no indication of additional hole states is found in the calculations. The new in-gap state was proposed to give rise to an optical transition at 1.5 eV in absorption spectra. In a subsequent hybrid DFT study, alternative positions were explored for N dopants in the Cu_2O lattice.[15] Using an ab-initio thermodynamic approach, substitutional N_O and $(N_2)_{Cu}$ defects were found to be thermodynamically preferred at Cu-rich and Cu-poor chemical potentials, respectively, while anionic substitution with N_2, $(N_2)_O$, or interstitial nitrogen atoms (N_i^{oct}, N_i^{tet}) turned out to be unstable (Fig. 41c). Similarly to the previous paper,[221] the N_O defect produces a deep transition state inside the band gap (0.53 eV above the VB top) that can neither serve as electron acceptor nor explain the increased p-type conductivity of N-doped Cu_2O. In contrast, the $(N_2)_{Cu}$ substitution introduces a suitable acceptor state with ~0.2 eV activation energy for VB electrons, being compatible with the experimental conductivity measured for bulk Cu_2O at temperatures below 100 K (Fig. 2).[10] Moreover, the $(N_2)_{Cu}$ related defect state strongly overlaps with the VB and has delocalized character, corroborating its ability to act as shallow acceptor. The work further suggests that Cu_2O luminescence can be used to distinguish between $(N)_O$ and $(N_2)_{Cu}$ defects formed upon nitrogen doping.[15] The former produce an optical band at ~1.6 eV, which blue-shifts to 1.9 eV in the latter case.

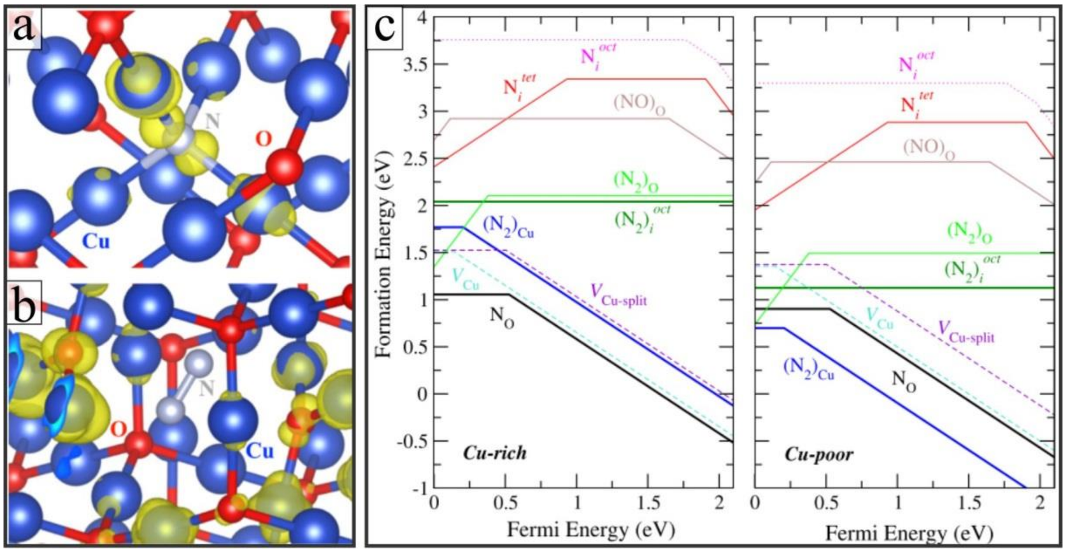

Figure 41: Local structure of (a) N_O and (b) $(N_2)_{Cu}$ defects in Cu_2O as calculated with a DFT HSE approach. (c) Formation energies of N-related defects as a function of E_F at Cu-rich and Cu-poor growth conditions.[15]

The validity of the two nitrogen doping scenarios has been explored in numerous experimental studies, so far without clear preference for either one or the other model. The common approach to synthesize N-doped Cu_2O in these works was magnetron sputtering of copper in a mixture of oxygen and nitrogen. The nitrogen concentration inside the sample was typically probed by secondary-ion mass-spectrometry (SIMS) or XPS, and could be varied between 10^{17} to 10^{21} atoms/cm^3 (Fig. 42a).[14,222,223] In early photoluminescence experiments, an emerging peak at 875 nm (1.85 eV) was assigned to the N-dopants.[224] Unfortunately, the spectra lacked all the other characteristic fingerprints of bulk Cu_2O, especially the free-exciton, O- and Cu-vacancy related luminescence maxima. In a couple of further experiments, an increasing hole density and a decreasing sheet-resistance of the Cu_2O films was taken as evidence for successful nitrogen doping (Fig. 42b).[223,225,226] Also, the contact resistance between Cu_2O and different metal electrodes was found to decrease with increasing N-doping level.[227] However, no direct indication for N-species populating either O or Cu substitutional sites could be provided in those studies. Moreover, it could not be precluded that the detected electronic effects were actually triggered by parasitic changes in crystallinity or morphology of the oxide material instead of the intended doping effect.

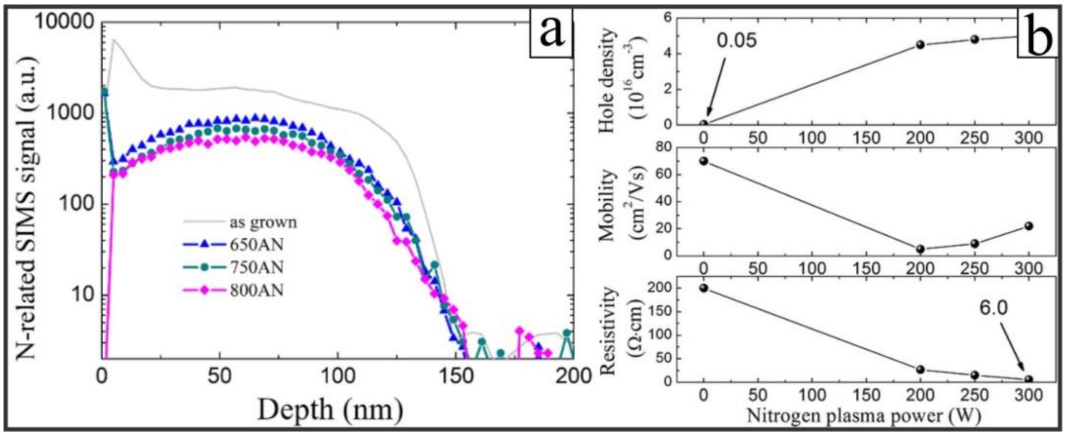

Figure 42: (a) Nitrogen concentration in differently annealed Cu_2O:N samples of 150 nm thickness measured with SIMS. (b) Hole density, hole mobility, and sheet resistance of Cu_2O:N samples annealed at 750°C as the function of the nitrogen plasma power used for preparation.[14]

Also, PL spectroscopy has been exploited to pinpoint the impact of nitrogen doping on the optical response of Cu_2O.[14] Instead of the PL maximum predicted by theory,[15] the experiments revealed a strong V_O-related resonance at 1.65 eV (750 nm) in the N-doped films that decreased in intensity during oxygen annealing. The diminishing V_O luminescence was hereby taken as evidence that interstitial nitrogen in the Cu_2O lattice fill the defect sites. However, the occurrence of a strong V_O emission could also be interpreted as compensation effect, in which N atoms in O substitutional sites generate O vacancies in order to keep the oxide charge neutral. The observed reduction of the V_O luminescence would then be the consequence of vacancy annihilation due to oxygen incorporation from the gas phase, a scenario that was discarded by the authors. In another work, the N concentration in the reactive gas used for Cu oxidation was found to determine the stoichiometry of the evolving copper oxide films.[228] While CuO was the dominant phase in an N-poor growth environment, the phase shifted towards Cu_2O with increasing nitrogen concentration. Simultaneously, the oxide band gap was found to widen, an effect that was assigned to N-doping but could be triggered by the phase transformation as well. In fact, none of the other optical studies could reveal a band-gap increase in Cu_2O upon nitrogen-doping.[223] Only very few works addressed the topic of N_2 incorporation into Cu_2O films.[229] One study successfully detected a N_2 Raman signal at 2250 cm^{-1} in line with the formation of $(N_2)_{Cu}$ defects, although most of the N-species still got incorporated in the form on N_O defects, as deduced from a rising oxide conductivity at higher N_2 flow rate. Moreover, a recent XPS study confirmed the presence of various N-species in nitrogen-doped Cu_2O, one due to substitutional N_O defects (E_B = 396 eV), and two related to N_2-derived species (E_B = 399 and 405 eV).[230] Somehow unexpected, the atomic N dopants turned into embedded molecular species upon annealing the oxide sample, suggesting higher thermodynamic stability of the latter. A systematic nitrogen-doping experiment of cupric oxide (CuO) is finally described in Ref. 231. It reproduced major doping effects found for Cu_2O before, such as an increasing hole concentration and a reduced carrier mobility at higher doping level. Also, the activation barrier for charge transport was carefully determined to ~0.15 eV in a wide temperature window, which compares to 0.27 eV for non-doped CuO.

In summary, the mechanistic picture for nitrogen-doping of copper oxide remains incomplete and inconsistent at many points, despite the large number of experimental and theoretical studies. Moreover, experiments performed with a rigorous surface-science approach are still missing, although they would probably provide atomic-scale insights into the nature of the nitrogen dopants. The situation thus resembles the one on N-doped TiO_2, where internal compensation mechanisms, e.g., O vacancy formation, counteract the expected doping effects, and the overall picture appeared to be much more complex than initially anticipated.[232]

5.2. *Alternative dopants*

While anionic doping of Cu_2O concerned mostly nitrogen, a few theoretical studies addressed the insertion of other anions into the oxide lattice. Halogen doping (F, Cl, Br, I) generally induces an impurity level just below the CB edge, which in turn promotes an n-type conductance behavior of Cu_2O.[233] With higher atomic number of the halogen, the donor level shifts towards the band edge, yet at the expense of an increasing lattice distortion and a larger defect formation energy. Due to this interplay, n-type doping of Cu_2O is predicted to be most successful with Cl atoms substituting the lattice oxygen.

Cationic doping was mostly explored from a theoretical point of view, either as a means to promote the p-type conductivity of Cu_2O or to narrow down its band gap and improve its photo-activity. A first systematic DFT PBE study of metal doping was carried out by Nolan and Elliott, placing different metal ions onto Cu substitutional sites and compensating their unmatched valence by Cu vacancies.[234] They identified two fundamental effects. While dopants with large ionic radius, e.g., La^{3+}, Sr^{2+} and Ba^{2+}, trigger a sizeable lattice distortion that widens the Cu_2O band gap, strongly interacting species, such as In^{3+}, Ti^{4+} and Ce^{4+}, introduce defect levels inside the gap region that in turn reduce the optical transition energies. The impact of doping on the magnetic response of Cu_2O was explored by substituting copper with Mn, Fe, Co or Ni atoms in the oxide lattice.[235] Especially, Fe (Mn) was found to induce large magnetic moments associated with a ferro (antiferro)-magnetic response of the intrinsically non-magnetic Cu_2O. The latter was additionally altered by the presence of O vacancies in the lattice. The interaction between metal dopants and Cu vacancies was further explored in a detailed DFT-HSE study by Carter et al.[11] Hereby, the insertion of Mg, Mn and Zn single-atom dopants was found to be exothermic and accompanied by Cu vacancy formation. Li incorporation, on the other hand, was endothermic and, given its iso-charged nature, not compensated by a Cu defect (Fig. 43). Moreover, most dopants seem to prefer a tetrahedral coordination in the oxide lattice, with the compensating Cu vacancy located in the next coordination shell. Most interestingly, the formation of split vacancies was largely suppressed in the presence of metal dopants, especially for substitutional Li, removing a potential trapping site for charge carriers in the oxide material. Appropriate metal doping was therefore suggested to be a means to improve the photoconductivity of bulk Cu_2O.[11] Hydrogen interstitials were finally proposed to change the conductance response of Cu_2O from p- to n-type.[236]

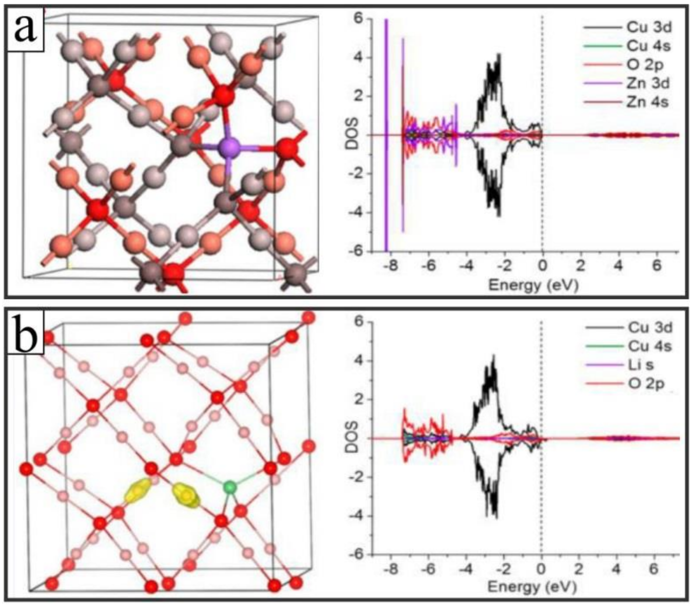

Figure 43: Relaxed structure of (a) Zn-doped Cu_2O with a Cu vacancy and (b) Li-doped Cu_2O, as calculated with DFT-HSE. In both cases, the dopant takes a tetrahedral coordination with oxygen in the lattice. The yellow color in (b) marks the excess spin density introduced by the Li defect. The projected DOS for the two doping configurations is depicted in the right panels.[11]

In contrast to multiple theoretical studies aiming at cationic doping of Cu_2O, the number of experiments addressing this topic is surprisingly small. Ni-doped Cu_2O films, grown by pulsed-laser deposition from a Ni:CuO target, were shown to develop a higher hole concentrations than pristine films, in agreement with the formation of compensating Cu vacancies in the lattice.[237] Moreover, the increasing Ni content triggered a gradual phase change from Cu_2O to CuO during film growth. Photoluminescence spectroscopy was used to investigate the effect of Mn-doping of Cu_2O films. According to XPS, the Mn ions take a 2+ charge state and occupy Cu substitutional sites. An optical transition between two Mn crystal-field states produced a pronounced blue-light emission at ~480 nm, while excitonic bands were largely suppressed.

Attempts to dope Cu_2O with sodium ions did not result in apparent changes of the electronic or optical response, as concluded from XPS and PL measurements.[238] The effect of alkali doping thus needs to be examined more carefully in forthcoming studies.

In summary, metal doping might be a powerful approach to change fundamental properties of cuprous oxide. Hereby, the carrier density is modulated by introducing Cu vacancies to compensate the charge mismatch with the aliovalent dopants.[11,234] In addition, defect states inserted by substitutional dopants may open dipole-allowed transitions across the band gap, releasing optical constraints imposed by the dark nature of ground-state excitons in Cu_2O. However similar to anionic doping, the studies on cation-doped Cu_2O are still in their infancy and high-quality doping experiments are hardly found in the literature.

6. Summary and Outlook

This article aimed at introducing the surface properties of cuprous oxide (Cu_2O), putting special emphasis on the thermodynamically preferred (111) surface. The first section addressed the profound differences between ultrathin Cu-O precursor oxides, as grown on many (111)-oriented metal supports such as Cu(111), Pt(111) and Au(111), and a truly bulk-type Cu_2O(111) surface. It demonstrated that ultrathin Cu-O layers cannot serve as model systems for the respective bulk material, as structural, electronic and optical properties deviate substantially. Moreover, experimental instructions were given on how thick Cu_2O and CuO films with bulk-like properties can be fabricated reliably. For this purpose, the temperature and pressure-dependent oxidation behavior of copper was studied via time-resolved optical schemes, revealing that Cu oxidation does not take place at O_2 partial pressures below 50 mbar.

The central, third chapter provided detailed insights into the atomic-scale properties of low-index Cu_2O planes, especially the (111), (100) and (110) one. All three surfaces are subject to massive reconstructions, driven by the strongly covalent nature of the Cu-O bond as well as by the inherent polarity of the (100) and (110) bulk cuts. The (111) surface develops a $(\sqrt{3}\times\sqrt{3})R30°$ reconstruction at vacuum-compatible preparation conditions that could be associated with the nano-pyramidal surface model proposed by DFT calculations. Hereby, Cu_4O nanopyramids populate every third Cu_6O_6 ring of the non-reconstructed surface, which saturates all O_{cus}-derived dangling bonds and drastically reduces the surface energy. The resulting Cu-deficiency of the $(\sqrt{3}\times\sqrt{3})R30°$ termination gives rise to an electron accumulation in the surface, which in turn leads to an upward band bending, the formation of an empty VB pocket and a work function increase. The experimentally deduced (3,0;1,1) phase of Cu_2O(100), on the other hand, largely follows the requirements for polarity compensation and primarily involves Cu-dimerization accompanied by a reduction of the copper surface charges. The atomic structure of Cu_2O(110), on the other hand, had only be explored by DFT calculations so far, and high-resolution microscopy data, confirming the proposed models, are unavailable at this point.

Chapter four reviewed the optical properties of Cu_2O, connecting the bulk optical response as governed by para- and ortho-excitons as well as their trapping behavior at lattice defects, with the luminescence characteristics of thin films. In particular, experimental techniques to probe the atomic-scale optical response of Cu_2O(111) by means of STM luminescence spectroscopy were presented. Experimental and theoretical studies dealing with the impact of cationic and anionic dopants in the Cu_2O lattice finally completed this review article. Here, mainly nitrogen doping as a means to enhance the carrier concentration, and metal doping to modify the excitonic response of Cu_2O have been discussed.

Given its pronounced p-type character, a band gap in the visible spectral range and an adaptable exciton response, cuprous oxide might become a decisive ingredient for future electronic, photovoltaic and photochemical applications. Despite this enormous potential, pivotal properties of the material are not sufficiently characterized and explored at this point. This concerns, for example, the termination of the catalytically relevant (110) surface, the precise structure and localization of Cu vacancies including the energy position of associated gap states as well as the role of dopants in the oxide lattice. Although tremendous progress has been made in the preparation, atomic-scale characterization, and modeling of cuprous oxide in recent years, as demonstrated in this article, a substantial amount of work still lies ahead of experimentalists and theoreticians. However, these efforts will pay out eventually, as new building blocks for photochemical and opto-electronic technologies may be established.

Acknowledgments

This work would have been impossible without the enthusiastic contribution of several PhD students and postdocs in our groups that should be acknowledged at this point: Hanna Fedderwitz, Christoph Möller, Alexander Gloystein, Mina Soltanmohammadi. Financial support was provided by the DFG grant Ni 650 5-1 and 5-2: ‘Towards an atomic-scale understanding of ideal, defective and doped cuprous oxide surfaces and interfaces’.

List of References

---

[1] B.K. Meyer, A. Polity, D. Reppin, M. Becker, P. Hering, P.J. Klar, T. Sander, C. Reindl, J. Benz, M. Eickhoff, C. Heiliger, M. Heinemann, J. Bläsing, a. Krost, S. Shokovets, C. Müller, C. Ronning, Binary copper oxide semiconductors: From materials towards devices, Phys. Status Solidi. 249 (2012) 1487–1509. https://doi.org/10.1002/pssb.201248128.

[2] C. Gattinoni, A. Michaelides, Atomistic details of oxide surfaces and surface oxidation: the example of copper and its oxides, Surf. Sci. Rep. 70 (2015) 424–447. https://doi.org/10.1016/j.surfrep.2015.07.001.

[3] B. Keimer, S. A. Kivelson, M.R. Norman, S. Uchida, J. Zaanen, From quantum matter to high-temperature superconductivity in copper oxides, Nature 518 (2015) 179-186. https://doi.org/ 10.1038/nature14165.

[4] A. Zivković, J. Sheehama, M.E.A. Warwick, D.R. Jones, C. Mitchel, D. Likius, V. Uahengo, N.Y. Dzade, S. Meenakshisundaram, C.W. Dunnill, N.H. De Leeuw, Structural and electronic properties of Cu_4O_3: The role of native impurities, Pure Appl. Chem. 93 (2021) 1229–1244. https://doi.org/10.1515/pac-2021-0114.

[5] M. Heinemann, B. Eifert, C. Heiliger, Band structure and phase stability of the copper oxides Cu_2O, CuO, and Cu_4O_3, Phys. Rev. B 87 (2013) 115111. https://doi.org/10.1103/PhysRevB.87.115111.

[6] M. Nolan, S.D. Elliott, The p-type conduction mechanism in Cu_2O: a first principles study, Phys. Chem. Chem. Phys. 8 (2006) 5350–53. https://doi.org/10.1039/b611969g.

[7] H. Raebiger, S. Lany, A. Zunger, Origins of the p-type nature and cation deficiency in Cu2O and related materials, Phys. Rev. B. 76 (2007) 045209. https://doi.org/10.1103/PhysRevB.76.045209.

[8] A. M. Deml, A. M. Holder, R. P. O'Hayre, C. B. Musgrave, V. Steyanovic, J. Phys. Chem. Lett 6 (2015)1948-1953. https://doi.org/10.1021/acs.jpclett.5b00710.

[9] P.J. Isherwood, J.M. Walls, Cupric oxide-based p-type transparent conductors, Energy Procedia 60 (2014) 129 – 134. https://doi.org/10.1016/j.egypro.2014.12.354.

[10] M. Nyborg, I. Kolevatov, G.C. Vásquez, K. Bergum, E. Monakhov, Dominant defects and carrier transport in single crystalline cuprous oxide: A new attribution of optical transitions, J. Appl. Phys. 130 (2021) 175701. https://doi.org/10.1063/5.0059406.

[11] L.Y. Isseroff, E. Carter, Electronic structure of pure and doped cuprous oxide with copper vacancies: Suppression of trap states, Chem. Mater. 25 (2013) 253–265. https://doi.org/10.1021/cm3040278.

[12] D.O. Scanlon, B.J. Morgan, G.W. Watson, A. Walsh, Acceptor levels in p-type Cu_2O: Rationalizing theory and Experiment, Phys. Rev. Lett. 103 (2009) 096405. https://doi.org/10.1103/PhysRevLett.103.096405.

[13] G.K. Paul, Y. Nawa, H. Sato, T. Sakurai, K. Akimoto, Defects in Cu_2O studied by deep level transient spectroscopy, Appl. Phys. Lett. 88 (2006) 2–5. https://doi.org/10.1063/1.2175492.

[14] J. Li, Z. Mei, L. Liu, H. Liang, A. Azarov, A. Kuznetsov, Y. Liu, A. Ji, Q. Meng, X. Du, Probing defects in nitrogen-doped Cu_2O, Sci. Rep. 4 (2014) 1–6. https://doi.org/10.1038/srep07240.

[15] J. T-Thienprasert, S. Limpijumnong, Identification of nitrogen acceptor in Cu_2O: First-principles study, Appl. Phys. Lett. 107 (2015) 221905. https://doi.org/10.1063/1.4936760.

[16] W. Tiano, M. Dapiaggi, G. Artioli, Thermal expansion in cuprite-type structures from 10 K to decomposition temperature: Cu_2O and Ag_2O, J. Appl. Crystallogr. 36 (2003) 1461–1463. https://doi.org/10.1107/S0021889803020818.

[17] J. Warren, K. O'Hara, J. Wolfe, Two-body decay of thermalized excitons, Phys. Rev. B - Condens. Matter Mater. Phys. 61 (2000) 8215–8223. https://doi.org/10.1103/PhysRevB.61.8215.

[18] T. Kazimierczuk, D. Fröhlich, S. Scheel, H. Stolz, M. Bayer, Giant Rydberg excitons in the copper oxide Cu_2O, Nature. 514 (2014) 343–347. https://doi.org/10.1038/nature13832.

[19] J.L. Lin, J.P. Wolfe, Bose-Einstein Condensation of Paraexcitons in Stressed Cu_2O, Phys. Rev. Lett. 71 (1993) 1222–1225. https://doi.org/10.1103/PhysRevLett.71.1222.

[20] D. Snoke, G.M. Kavoulakis, Bose-Einstein condensation of excitons in Cu_2O: Progress over 30 years, Reports Prog. Phys. 77 (2014) 116501. https://doi.org/10.1088/0034-4885/77/11/116501.

---

[21] K.E. O'Hara, J.R. Gullingsrud, J.P. Wolfe, Auger decay of excitons in Cu_2O, Phys. Rev. B - Condens. Matter Mater. Phys. 60 (1999) 10872–10885. https://doi.org/10.1103/PhysRevB.60.10872.

[22] J.I. Jang, Y. Sun, B. Watkins, J.B. Ketterson, Bound excitons in Cu_2O: Efficient internal free exciton detector, Phys. Rev. B - Condens. Matter Mater. Phys. 74 (2006) 235204. https://doi.org/10.1103/PhysRevB.74.235204.

[23] S. Koirala, N. Naka, K. Tanaka, Correlated lifetimes of free paraexcitons and excitons trapped at oxygen vacancies in cuprous oxide, J. Lumin. 134 (2013) 524–527. https://doi.org/10.1016/j.jlumin.2012.07.035.

[24] D.W. Snoke, J.P. Wolfe, A. Mysyrowicz, Evidence for Bose-Einstein condensation of excitons in Cu_2O, Phys. Rev. B 41 (1990) 11171. https://doi.org/10.1103/physrevb.41.11171.

[25] D. Snoke, Spontaneous Bose coherence of excitons and polaritons, Science 298 (2002) 1368–1372. https://doi.org/10.1126/science.1078082.

[26] T. Ito, T. Masumi, Detailed Examination of Relaxation Processes of Excitons in Photoluminescence Spectra of Cu_2O, J. Phys. Soc. Japan. 66 (1997) 2185–2193. https://doi.org/10.1143/JPSJ.66.2185.

[27] L. O. Grondahl, The Copper-Cuprous-Oxide Rectifier and Photoelectric Cell, Rev. Mod. Phys. 5 (1933) 141. https://doi.org/10.1103/RevModPhys.5.141.

[28] L.C. Olsen, F.W. Addis, W. Miller, Experimental and theoretical studies of Cu_2O solar cells, Sol. Cells. 7 (1983) 247–279. https://doi.org/10.1016/0379-6787(82)90050-3.

[29] S. Chatterjee, S.K. Saha, A.J. Pal, Formation of all-oxide solar cells in atmospheric condition based on Cu_2O thin-films grown through SILAR technique, Sol. Energy Mater. Sol. Cells. 147 (2016) 17–26. https://doi.org/10.1016/j.solmat.2015.11.045.

[30] T.K.S. Wong, S. Zhuk, S. Masudy-Panah, G.K. Dalapati, Current Status and Future Prospects of Copper Oxide Heterojunction Solar Cells, Materials 9 (2016) 271. https://doi.org/10.3390/ma9040271.

[31] A. Mittiga, E. Salza, F. Sarto, M. Tucci, R. Vasanthi, Heterojunction solar cell with 2% efficiency based on a Cu_2O substrate, Appl. Phys. Lett. 88 (2006) 163502. https://doi.org/10.1063/1.2194315.

[32] H. M. Wei, H. B. Gong, L. Chen, M. Zi, B. Q. Cao, Photovoltaic Efficiency Enhancement of Cu_2O Solar Cells Achieved by Controlling Homojunction Orientation and Surface Microstructure J. Phys. Chem. C 116 (2012) 10510–10515, https://doi.org/10.1021/jp301904s.

[33] J.F. Pierson, a. Thobor-Keck, a. Billard, Cuprite, paramelaconite and tenorite films deposited by reactive magnetron sputtering, Appl. Surf. Sci. 210 (2003) 359–367. https://doi.org/10.1016/S0169-4332(03)00108-9.

[34] M. Yin, C.-K. Wu, Y. Lou, C. Burda, J.T. Koberstein, Y. Zhu, S. O'Brien, Copper oxide nanocrystals., J. Am. Chem. Soc. 127 (2005) 9506–11. https://doi.org/10.1021/ja050006u.

[35] Z. Yang, C.-K. Chiang, H.-T. Chang, Synthesis of fluorescent and photovoltaic Cu_2O nanocubes., Nanotechnology. 19 (2008) 025604. https://doi.org/10.1088/0957-4484/19/02/025604.

[36] C.H. Kuo, M.H. Huang, Morphologically controlled synthesis of Cu_2O nanocrystals and their properties, Nano Today. 5 (2010) 106–116. https://doi.org/10.1016/j.nantod.2010.02.001.

[37] Y. Shang, L. Guo, Facet-Controlled Synthetic Strategy of Cu_2O-Based Crystals for Catalysis and Sensing, Adv. Sci. 2 (2015) 1500140. https://doi.org/10.1002/advs.201500140.

[38] S. Sun, X. Zhang, Q. Yang, S. Liang, X. Zhang, Z. Yang, Cuprous oxide (Cu_2O) crystals with tailored architectures: A comprehensive review on synthesis, fundamental properties, functional modifications and applications, Prog. Mater. Sci. 96 (2018) 111–173. https://doi.org/10.1016/j.pmatsci.2018.03.006.

[39] H. Bao, W. Zhang, D. Shang, Q. Hua, Y. Ma, Z. Jiang, J. Yang, W. Huang, Shape-dependent reducibility of cuprous oxide nanocrystals, J. Phys. Chem. C. 114 (2010) 6676–6680. https://doi.org/10.1021/jp101617z.

[40] R. Chen, Z. Ren, Y. Liang, G. Zhang, T. Dittrich, R. Liu, Y. Liu, Y. Zhao, S. Pang, H. An, C. Ni, P. Zhou, K. Han, F. Fan, C. Li, Spatiotemporal imaging of charge transfer in photocatalyst particles, Nature. 610 (2022) 296–301. https://doi.org/10.1038/s41586-022-05183-1.

[41] C.S. Tan, S.C. Hsu, W.H. Ke, L.J. Chen, M.H. Huang, Facet-dependent electrical conductivity properties of Cu_2O crystals, Nano Lett. 15 (2015) 2155–2160. https://doi.org/10.1021/acs.nanolett.5b00150.

---

[42] Q.B. Zhang, K.L. Zhang, D.G. Xu, G.C. Yang, H. Huang, F.D. Nie, C.M. Liu, S.H. Yang, CuO nanostructures: Synthesis, characterization, growth mechanisms, fundamental properties, and applications, Prog. Mat. Sci. 60 (2014) 208-337. https://doi.org/10.1016/j.pmatsci.2013.09.003.

[43] O. Baranov, K. Bazaka, T. Belmonte, C. Riccardi, H.E. Roman, M. Mohandas, S. Xu, U. Cvelbarb, I. Levchenko, Recent innovations in the technology and applications of low-dimensional CuO nanostructures for sensing, energy and catalysis, Nanoscale Horiz. 8 (2023) 568–602. https://doi.org/10.1039/D2NH00546H.

[44] X. Ren, H. Wang, J. Chen, W. Xu, Q. He, H. Wang, F. Zhan, S. Chen, L. Chen, Emerging 2D Copper-Based Materials for Energy Storage and Conversion: A Review and Perspective, Small 19 (2023) 2204121. https://doi.org/10.1002/smll.202204121.

[45] G.G. Jernigan, G. Somorjai, Carbon Monoxide Oxidation over Three Different Oxidation States of Copper: Metallic Copper, Copper (I) Oxide, and Copper (II) Oxide -A Surface Science and Kinetic Study, J. Catal. 147 (1994) 567–577. https://doi.org/10.1006/jcat.1994.1173.

[46] M.M. Günter, T. Ressler, R.E. Jentoft, B. Bems, Redox Behavior of Copper Oxide /Zinc Oxide Catalysts in the Steam Reforming of Methanol, J. Catalysis 203 (2001) 133-149. https://doi.org/10.1006/jcat.2001.3322.

[47] Y.M. Liu, J.-T. Liu, S.-Z. Liu, J. Li, Z.-H. Gao, Z.-J. Zuo, W. Huang, Reaction mechanisms of methanol synthesis from CO/CO_2 hydrogenation on Cu_2O (111), J. CO_2 Utilization 20 (2017) 59-65. https://doi.org/10.1016/j.jcou.2017.05.005.

[48] Z. Gu, H. Shen, L. Shang, X. Lv, L. Qian, G. Zheng, Nanostructured Copper-Based Electrocatalysts for CO_2 Reduction, Small Methods 2 (2018) 1800121. https://doi.org/10.1002/smtd.201800121.

[49] Y.S. Panova, A.S. Kashin, M.G. Vorobev, E.S. Degtyareva, V.P. Ananikov, Nature of the Copper-Oxide-Mediated C–S Cross-Coupling Reaction: Leaching of Catalytically Active Species from the Metal Oxide Surface, ACS Catal. (2016) 3637–3643. https://doi.org/10.1021/acscatal.6b00337.

[50] S. Kakuta, T. Abe, Photocatalytic activity of Cu_2O nanoparticles prepared through novel synthesis method of precursor reduction in the presence of thiosulfate, Solid State Sci. 11 (2009) 1465–1469. https://doi.org/10.1016/j.solidstatesciences.2009.05.002.

[51] J. Cheng, L. Wu, J. Luo, Cuprous oxide photocathodes for solar water splitting, Chem. Phys. Rev. 3 (2022) 031306. https://doi.org/10.1063/5.0095088.

[52] Y.A. Wu, I. McNulty, C. Liu, et al., Facet-dependent active sites of a single Cu_2O particle photocatalyst for CO_2 reduction to methanol, Nat. Energy 4 (2019) 957–968. https://doi.org/10.1038/s41560-019-0490-3.

[53] Z. Zheng, B. Huang, Z. Wang, M. Guo, X. Qin, X. Zhang, P. Wang, Y. Dai, Crystal faces of Cu_2O and their stabilities in photocatalytic reactions, J. Phys. Chem. C. 113 (2009) 14448–14453. https://doi.org/10.1021/jp904198d.

[54] O. Kubaschewski, B.E. Hopkins, Oxidation of Metals and Alloys, (Butterworths, London, 1962).

[55] A.T. Fromhold. Jr., Theory of Metal Oxidation: Fundamentals, (North-Holland, Amsterdam, 1976).

[56] Y. Zhu, K. Mimura, J.-W. Lim, M. Isshiki, Q. Jiang, Brief review of oxidation kinetics of copper at 350-1050 °C, Metall. Mater. Trans. A. 37 (2006) 1231–1237. https://doi.org/10.1007/s11661-006-1074-y.

[57] G. Papadimitropoulos, N. Vourdas, V.E. Vamvakas, D. Davazoglou, Optical and structural properties of copper oxide thin films grown by oxidation of metal layers, Thin Solid Films. 515 (2006) 2428–2432. https://doi.org/10.1016/j.tsf.2006.06.002.

[58] G.K.P. Ramanandan, G. Ramakrishnan, P.C.M. Planken, Oxidation kinetics of nanoscale copper films studied by terahertz transmission spectroscopy, J. Appl. Phys. 111 (2012). https://doi.org/10.1063/1.4729808.

[59] A. Manara, V. Sirtori, L. Mammarella, Optical Ellipsometry and Electron Spectroscopy Studies of Copper Oxidation Related to Copper on Printed Circuit Boards, Surf. Interface Anal. 18 (1992) 32–38. https://doi.org/10.1002/sia.740180106.

[60] M. Rauh, P. Wißmann, The oxidation kinetics of thin copper films studied by ellipsometry, Thin Solid Films. 228 (1993) 121–124. https://doi.org/10.1016/j.tsf.2005.11.031.

---

[61] B.H. Liu, M. Huber, M.A. van Spronsen, M. Salmeron, H. Bluhm, Ambient pressure X-ray photoelectron spectroscopy study of room-temperature oxygen adsorption on Cu(1 0 0) and Cu(1 1 1), Appl. Surf. Sci. 583 (2022) 152438. https://doi.org/10.1016/j.apsusc.2022.152438.

[62] J. Li, G. Vizkelethy, P. Revesz, J.W. Mayer, K.N. Tu, Oxidation and Reduction of Copper Oxide Thin Films. J. Appl. Phys. 69 (1991) 1020–1029. https://aip.scitation.org/doi/10.1063/1.347417.

[63] K. Fujita, D. Ando, M. Uchikoshi, K. Mimura, M. Isshiki, New model for low-temperature oxidation of copper single crystal, Appl. Surf. Sci. 276 (2013) 347–358. https://doi.org/10.1016/j.apsusc.2013.03.096.

[64] A. Atkinson, Transport processes during the growth of oxide films at elevated temperature, Rev. Mod. Phys. 57 (1985) 437–470. https://doi.org/10.1103/RevModPhys.57.437.

[65] G. Tammann, Über Anlauffarben von Metallen, Zeitschrift Für Anorg. Und Allg. Chemie. 111 (1920) 78–89. https://doi.org/10.1002/zaac.19201110107.

[66] N.E. Pilling, R.E. Bedworth, The Oxidation of Metals at High Temperatures, J. Inst. Metals 29 (1923) 529–582.

[67] C. Wagner, Beitrag zur Theorie des Anlaufvorgangs, Z. Phys. Chem. 21 (1933) 25–41. https://doi.org/10.1515/zpch-1933-2105.

[68] N. Cabrera, N.F. Mott, Theory of the oxidation of metals, Reports Prog. Phys. 12 (1949) 163–184. https://doi.org/10.1088/0034-4885/12/1/308.

[69] A.T. Fromhold, E.L. Cook, Kinetics of oxide film growth on metal crystals: Thermal electron emission and ionic diffusion, Phys. Rev. 163 (1967) 650–664. https://doi.org/10.1103/PhysRev.163.650.

[70] M.A.H. Lanyon, B.M.W. Trapnell, The interaction of oxygen with clean metal surfaces, Proc. Roy. Soc. 227 (1955) 387–399. https://doi.org/10.1098/rspa.1955.0018.

[71] F. Jensen, F. Besenbacher, E. Laegsgaard, I. Stensgaard, Oxidation of Cu(111) - two new oxygen induced reconstructions, Surf. Sci. Lett. 259 (1991) L774. https://doi.org/10.1016/0039-6028(91)90550-C.

[72] F. Jensen, F. Besenbacher, I. Stensgaard, Two new oxygen induced reconstructions on Cu(111), Surf. Sci. 269–270 (1992) 400–404. https://doi.org/10.1016/0039-6028(92)91282-G.

[73] Y.J. Lee, T.T. Ly, T. Lee, K. Palotás, S.Y. Jeong, J. Kim, A. Soon, Completing the picture of initial oxidation on copper, Appl. Surf. Sci. 562 (2021). https://doi.org/10.1016/j.apsusc.2021.150148.

[74] A.J. Therrien, R. Zhang, F.R. Lucci, M.D. Marcinkowski, A. Hensley, J.S. McEwen, E.C.H. Sykes, Structurally Accurate Model for the “29”-Structure of Cu_xO/Cu(111): A DFT and STM Study, J. Phys. Chem. C. 120 (2016) 10879–10886. https://doi.org/10.1021/acs.jpcc.6b01284.

[75] A.J. Therrien, A.J.R. Hensley, R. Zhang, A. Pronschinske, M.D. Marcinkowski, J.S. McEwen, E.C.H. Sykes, Characterizing the geometric and electronic structure of defects in the “29” copper surface oxide, J. Chem. Phys. 147 (2017). https://doi.org/10.1063/1.4996729.

[76] T.T. Ly, T. Lee, S. Kim, Y. Lee, G. Duvjir, K. Jang, Growing Ultrathin Cu_2O Films on Highly Crystalline Cu(111): A Closer Inspection from Microscopy and Theory, J Phys Chem C. 123 (2019) 12716. https://doi.org/10.1021/acs.jpcc.9b00255.

[77] A. Soon, M. Todorova, B. Delley, C. Stampfl, Oxygen adsorption and stability of surface oxides on Cu(111): A first-principles investigation, Phys. Rev. B. 73 (2006) 165424. https://doi.org/10.1103/PhysRevB.73.165424.

[78] F. Yang, Y. Choi, P. Liu, J. Hrbek, J. a. Rodriguez, Autocatalytic Reduction of a Cu_2O/Cu(111) Surface by CO: STM, XPS, and DFT Studies †, J. Phys. Chem. C. 114 (2010) 17042–17050. https://doi.org/10.1021/jp1029079.

[79] A.E. Baber, F. Xu, F. Dvorak, K. Mudiyanselage, M. Soldemo, J. Weissenrieder, S.D. Senanayake, J.T. Sadowski, J. a Rodriguez, V. Matolín, M.G. White, D.J. Stacchiola, In Situ Imaging of Cu_2O under Reducing Conditions: Formation of Metallic Fronts by Mass Transfer., J. Am. Chem. Soc. 135 (2013) 16781–4. https://doi.org/10.1021/ja408506y.

[80] H. Sträter, H. Fedderwitz, B. Groß, N. Nilius, Growth and Surface Properties of Cuprous Oxide Films on Au(111), J. Phys. Chem. C. 119 (2015) 5975–5981. https://doi.org/10.1021/jp511327h.

[81] Q. Liu, N. Han, S. Zhang, J. Zhao, F. Yang, X. Bao, Tuning the structures of two-dimensional cuprous oxide confined on Au(111), Nano Res. 2 (2018) 1–11. https://doi.org/10.1007/s12274-018-2109-6.

---

[82] C. Möller, H. Fedderwitz, C. Noguera, J. Goniakowski, N. Nilius, Temperature-dependent phase evolution of copper-oxide thin-films on Au(111), Phys. Chem. Chem. Phys. 20 (2018) 5636–5643. https://doi.org/10.1039/C7CP08387D.

[83] A. Gloystein and N. Nilius, Copper Oxidation on Pt(111)—More than a Surface Oxide?, J. Phys. Chem. C 123 (2019) 26939–26946. https://doi.org/10.1021/acs.jpcc.9b06935.

[84] F. Grillo, H. Früchtl, S. M. Francis, N. V. Richardson, Site selectivity in the growth of copper islands on Au (111), New J. Phys. 13 (2011) 013044. https://doi.org/10.1088/1367-2630/13/1/013044.

[85] Q. Liu, Y. Ning, W. Huang, Q. Fu, F. Yang, X. Bao, Origin of the thickness-dependent oxidation of ultrathin Cu films on Au(111), J. Phys. Chem. C. (2018) acs.jpcc.8b00460. https://doi.org/10.1021/acs.jpcc.8b00460.

[86] C.S. Ho, S. Banerjee, J.P. Roszell, B.E. Koel, Alloy formation and chemisorption at Cu/Pt(111) bimetallic surfaces using alkali ISS, XPD, and TPD, Surf. Sci. 617 *(*2013) 192–198. https://doi.org/10.1016/j.susc.2013.08.009.

[87] T. Lee, Y. Lee, S. Piccinin, A. Soon, A. Ab Initio Thermodynamics of Surface Oxide Structures under Controlled Growth Conditions, J. Phys. Chem. C 121 (2017) 2228–2233. https://doi.org/10.1021/acs.jpcc.6b11445.

[88] F. Yang, Y. Choi, P. Liu, D. Stacchiola, J. Hrbek, A. Rodriguez, Identification of 5-7 Defects in a Copper Oxide Surface, J. Am. Chem. Soc. 133 (2011) 11474–11477. https://doi.org/10.1021/ja204652v.

[89] W. Wang, Z. Wen, S. Hu, Z. Li, X. Wu, J. Zhu, X. Shao, An ultrathin cuprite film on Pt(111) with high reactivity to CO, Chem. Commun. 55 (2019) 5825–5828. https://doi.org/10.1039/c9cc01002e.

[90] K.P. Rice, J. Han, I.P. Campbell, M.P. Stoykovich, In situ Absorbance Spectroscopy for Characterizing the Low Temperature Oxidation Kinetics of Sputtered Copper Films, Oxid. Met. 83 (2015) 89–99. https://doi.org/10.1007/s11085-014-9508-1.

[91] Z. Grzesik, M. Migdalska, Oxidation mechanism of Cu$_2$O and defect structure of CuO at high temperatures, High Temp. Mater. Process. 30 (2011) 277–287. https://doi.org/10.1515/HTMP.2011.046.

[92] W.J. Moore, B. Selikson, The Diffusion of Copper in Cuprous Oxide, J. Chem. Phys. 19 (1951) 1539–1543. https://doi.org/10.1063/1.1700614.

[93] P.K. Krishnamoorthy, S.C. Sircar, Oxidation kinetics of copper in the thin film range, Acta Metall. 17 (1969) 1009–1012. https://doi.org/10.1016/0001-6160(69)90046-7.

[94] S. Roy, S. Sircar, A critical appraisal of the logarithmic rate law in thin-film formation during oxidation of copper and its alloys, Oxid. Met. 15 (1981) 9–20. https://doi.org/10.1007/BF00603754.

[95] I. Platzman, R. Brener, H. Haick, R. Tannenbaum, Oxidation of polycrystalline copper thin films at ambient conditions, J. Phys. Chem. C. 112 (2008) 1101–1108. https://doi.org/10.1021/jp076981k.

[96] B. Maack, N. Nilius, Oxidation of polycrystalline copper films – Pressure and temperature dependence, Thin Solid Films 651 (2018) 24-30. https://doi.org/10.1016/j.tsf.2018.02.007.

[97] B. Maack, N. Nilius, In-situ optical view onto copper oxidation – role of reactive interfaces and self-heating, Corros. Sci. 159 (2019) 108112. https://doi.org/10.1016/j.corsci.2019.108112.

[98] B. Harbecke, Coherent and Incoherent Reflection and Transmission of Multilayer Structures, Appl. Phys. B. 39 (1986) 165–170. https://doi.org/10.1007/BF00697414.

[99] J. C. M. Garnett, Colours in metal glasses and in metallic films, Philos. Trans. R. Soc. London. Ser. A. 203 (1904) 385–420. https://doi.org/10.1098/rsta.1904.0024.

[100] D. A. Bruggemann, Berechnung verschiedener physikalischer Konstanten von heterogenen Substanzen, Ann. Phys. 5 (1935) 636–664. https://doi.org/10.1002/andp.19354160705

[101] S.-K. Lee, H.-C. Hsu, W.-H. Tuan, Oxidation behavior of copper at a temperature below 300 °C and the methodology for passivation, Mat. Res. 19 (2016) 51. https://doi.org/10.1590/1980-5373-MR-2015-0139.

[102] F. Perinet, J. Duigou, C. Monty, Non-Stoichiometric Compounds, (Springer Netherlands, Dordrecht 1989).

[103] Y. Watanabe, R.W. Mowbray, K.P. Rice, M.P. Stoykovich, Kinetic description of metal nanocrystal oxidation: a combined theoretical and experimental approach for determining morphology and diffusion parameters in hollow nanoparticles by the nanoscale Kirkendall effect, Philosophical Magazine 94 (2014) 3487-3506. https://doi.org/10.1080/14786435.2014.962640

---

[104] B. Maack, N. Nilius, Impact of granularity on the oxidation kinetics of copper, Phys. Stat. Solidi b 257 (2020) 1900778. https://doi.org/10.1002/pssb.201900778.

[105] B. Maack, N. Nilius, Morphological and kinetic insights into Cu_2O–CuO oxidation, Phys. Stat. Solidi b 257 (2020) 1900365. https://doi.org/10.1002/pssb.201900365.

[106] K.H. Schulz, D.F. Cox, Photoemission and low-energy-electron-diffraction study of clean and oxygen-dosed Cu_2O (111) and (100) surfaces, Phys. Rev. B. 43 (1991) 1610–1621. https://doi.org/10.1103/PhysRevB.43.1610.

[107] J. Goniakowski, F. Finocchi, C. Noguera, Polarity of oxide surfaces and nanostructures, Reports Prog. Phys. 71 (2007) 016501. https://doi.org/10.1088/0034-4885/71/1/016501.

[108] P. W. Tasker, The Stability of ionic-crystal surfaces, J. Phys. C, 12 (1979) 4977-4984. https://doi.org/10.1088/0022-3719/12/22/036.

[109] C. Noguera, Polar oxide surfaces, J. Phys. Condensed Matter 12 (2000) R367. https://doi.org/10.1088/0953-8984/12/31/201.

[110] C. Noguera, J. Goniakowski, Polarity in oxide nano-objects, Chem. Rev. 113 (2013) 4073-4105. https://doi.org/10.1021/cr3003032.

[111] D.O. Scanlon, B.J. Morgan, G.W. Watson, Modelling the polaronic nature of p-type defects in Cu_2O: the failure of GGA and GGA+U., J. Chem. Phys. 131 (2009) 124703. https://doi.org/10.1063/1.3231869.

[112] L.Y. Isseroff, E. a. Carter, Importance of reference Hamiltonians containing exact exchange for accurate one-shot GW calculations of Cu_2O, Phys. Rev. B - Condens. Matter Mater. Phys. 85 (2012) 235142. https://doi.org/10.1103/PhysRevB.85.235142.

[113] Nilius, N.; Fedderwitz, H.; Groß, B.; Noguera, C.; Goniakowski, J. Incorrect DFT-GGA predictions of the stability of non-stoichiometric/polar dielectric surfaces: The case of Cu_2O(111), Phys. Chem. Chem. Phys. 18 (2016) 6729–6733. https://doi.org/10.1039/C5CP06933E.

[114] A. Gloystein, N. Nilius, J. Goniakowski, C. Noguera, The nanopyramidal reconstruction of Cu_2O(111): A long-standing surface puzzle solved by STM and DFT, J. Phys. Chem. C 124 (2020) 26937–26943. https://doi.org/10.1021/acs.jpcc.0c09330.

[115] A. Soon, M. Todorova, B. Delley, C. Stampfl, Thermodynamic stability and structure of copper oxide surfaces: A first-principles investigation, Phys. Rev. B. 75 (2007) 125420. https://doi.org/10.1103/PhysRevB.75.125420.

[116] M.M. Islam, B. Diawara, V. Maurice, P. Marcus, First principles investigation on the stabilization mechanisms of the polar copper terminated Cu_2O(1 1 1) surface, Surf. Sci. 603 (2009) 2087–2095. https://doi.org/10.1016/j.susc.2009.04.005.

[117] L.I. Bendavid, E.A. Carter, First-principles predictions of the structure, stability, and photocatalytic potential of Cu_2O surfaces, J. Phys. Chem. B. 117 (2013) 15750–15760. https://doi.org/10.1021/jp406454c.

[118] C. Li, F. Wang, S.F. Li, Q. Sun, Y. Jia, Stability and electronic properties of the O-terminated Cu_2O(111) surfaces: First-principles investigation, Phys. Lett. A 374 (2010) 2994–2998. https://doi.org/10.1016/j.physleta.2010.05.029.

[119] A. Önsten, M. Göthelid, U.O. Karlsson, Atomic structure of Cu_2O(111), Surf. Sci. 603 (2009) 257–264. https://doi.org/10.1016/j.susc.2008.10.048.

[120] M. Sterrer, M. Heyde, M. Nowicki, N. Nilius, T. Risse, H-P. Rust, G. Pacchioni, H.-J. Freund, Identification of color centers on MgO(001) thin films with STM, J. Phys. Chem. B 110 (2006) 46. https://doi.org/10.1021/jp056306f.

[121] A. Gloystein, J. A. Creed, N. Nilius, Atomic view on the (111) surface of a Cu_2O single crystal: Reconstruction, electronic properties, and band-bending effects, J. Phys. Chem. C 126 (2022) 16834–16840. https://doi.org/10.1021/acs.jpcc.2c04335.

[122] R. Zhang, L. Li, L. Frazer, K.B. Chang, K.R. Poeppelmeier, M.K.Y. Chan, J.R. Guest, Atomistic determination of the surface structure of Cu_2O(111): Experiment and theory, Phys. Chem. Chem. Phys. 20 (2018) 27456–27463. https://doi.org/10.1039/c8cp06023a.

---

[123] A. Gloystein, N. Nilius, High pressure oxidation of copper on Au(111) – A route towards bulk-like cuprous oxide films, J. Phys. Chem. C 124 (2020) 28605-28613. https://doi.org/10.1021/acs.jpcc.0c09773.

[124] M. Soltanmohammadi, E. Spurio, A. Gloystein, P. Luches, N. Nilius, Photoluminescence spectroscopy of cuprous oxide: Bulk crystal versus crystalline films, Phys. Stat. Solidi A 220 (2023) 2200887. https://doi.org/10.1002/pssa.202200887.

[125] S. Poulston, P.M. Parlett, P. Stone, M. Bowker, Surface oxidation and reduction of CuO and Cu_2O studied with XPS and XAES, Surf. Interface Anal. 24 (1996) 811–820. https://doi.org/10.1002/(SICI)1096-9918(199611)24:12<811::AID-SIA191>3.0.CO;2-Z.

[126] D. Tahir, S. Tougaard, Electronic and optical properties of Cu, CuO and Cu_2O studied by electron spectroscopy, J. Phys. Condens. Matter. 24 (2012) 175002. https://doi.org/10.1088/0953-8984/24/17/175002.

[127] T.T. Ly, T. Lee, K. Sanghwa, Y. Lee, G. Duvjir, K. Jang, K. Palotás, S.-Y. Jeong, A. Soon, K. Jungdae, Growing Ultrathin Cu_2O films on highly crystalline Cu(111): A closer inspection from microscopy and theory, J. Phys. Chem. C 123 (2019) 12716-12721. https://doi.org/10.1021/acs.jpcc.9b00255.

[128] H. Wu, N. Zhang, H. Wang, First-principles study of oxygen-vacancy Cu_2O(111) surface, J. Theor. Comput. Chem. 11 (2012) 1261-1280. https://doi.org/10.1142/S0219633612500848.

[129] L. Grad, Z. Novotny, M. Hengsberger, J. Osterwalder, Influence of surface defect density on the ultrafast hot carrier relaxation and transport in Cu_2O photoelectrodes, Sci. Rep. 10 (2020). https://doi.org/10.1038/s41598-020-67589-z.

[130] A. Önsten, J. Weissenrieder, D. Stoltz, S. Yu, M. Göthelid, U.O. Karlsson, Role of Defects in Surface Chemistry on Cu_2O(111), J. Phys. Chem. C. 117 (2013) 19357–19364. https://doi.org/10.1021/jp3112217.

[131] Cox, P. A, Transition metal oxides an introduction to their electronic structure and properties, Series of monographs on chemistry (Oxford, Clarendon Pr., 1992). https://doi.org/10.1002/ange.19931050352.

[132] A.K. Mishra, A. Roldan, N.H. de Leeuw, A density functional theory study of the adsorption behaviour of CO_2 on Cu_2O surfaces, J. Chem. Phys. 145 (2016) 044709. https://doi.org/10.1063/1.4958804.

[133] A. Gloystein, N. Nilius, C. Noguera, J. Goniakowski, Termination-dependent electronic structure and atomic-scale screening behavior of the Cu_2O(111) surface, J. Phys. Condens. Matter 33 (2021) 484001. https://doi.org/10.1088/1361-648X/ac2534.

[134] A. Gloystein, N. Nilius, Empty valence-band pocket in p-type Cu_2O(111) probed with STM conductance spectroscopy, Phys. Stat. Solidi B 258 (2021) 2100337. https://doi.org/10.1002/pssb.202100337.

[135] A.F. Wright, J.S. Nelson, Theory of the copper vacancy in cuprous oxide, J. Appl. Phys. 2002, 92, 5849. https://doi.org/10.1063/1.1516620.

[136] O. Porat, I. Riess, Defect chemistry of $Cu_{2-y}O$ at elevated temperatures. Part II: Electrical conductivity, thermoelectric power and charged point defects, Solid State Ionics 81 (1995) 29. https://doi.org/10.1016/0167-2738(95)00169-7. O. Porat, I. Riess, Defect chemistry of $Cu_{2-y}O$ at elevated temperatures. Part I: Non-stoichiometry, phase width and dominant point defects, Solid State Ionics 74 (1994) 229. https://doi.org/10.1016/0167-2738(94)90215-1.

[137] J. Xue, R.J. Dieckmann, The non-stoichiometry and the point defect structure of cuprous oxide ($Cu_{2-\delta}O$), Phys. Chem. Solids 51 (1990) 1263. https://doi.org/10.1016/0022-3697(90)90003-X.

[138] S. Aggarwal, J. Töpfer, T.-L. Tsai, R. Dieckmann, Point defects and transport in binary and ternary, non-stoichiometric oxides, Solid State Ionics 101 (1997) 321. https://doi.org/10.1016/S0167-2738(97)84048-9.

[139] L. Papadimitiriou, DLTS evaluation of nonexponential transients of defect levels in cuprous oxide (Cu_2O), Solid-State Electron. 36 (1993) 431. https://doi.org/10.1016/0038-1101(93)90098-B.

[140] G.K. Paul, Y. Nawa, H. Sato, T. Sakurai, K. Akimoto, Defects in Cu_2O studied by deep level transient spectroscopy, Appl. Phys. Lett. 88 (2006) 141901. https://doi.org/10.1063/1.2175492.

[141] Y.S. Lee, M.T. Winkler, S.C. Siah, R. Brandt, T. Buonassisi, Hall mobility of cuprous oxide thin films deposited by reactive direct-current magnetron sputtering, Appl. Phys. Lett. 98 (2011) 192115. https://doi.org/10.1063/1.3589810.

---

[142] J. Thewes, J. Heckötter, T. Kazimierczuk, M. Aßmann, D. Fröhlich, M. Bayer, M. a. Semina, M.M. Glazov, Observation of high angular momentum excitons in cuprous oxide, Phys. Rev. Lett. 115 (2015) 027402. https://doi.org/10.1103/PhysRevLett.115.027402.

[143] Kolesnychenko O Y, Kolesnichenko Y A, Shklyarevskii O I and van Kempen H, Field-emission resonance measurements with mechanically controlled break junctions, Physica B 291 (2000) 246–255. https://doi.org/10.1016/S0921-4526(99)02884-7

[144] D. Leuenberger, W.D. Zabka, O.F.R. Shah, S. Schnidrig, B. Probst, R. Alberto, J. Osterwalder, Atomically resolved band bending effects in a p-n heterojunction of Cu_2O and a Co macrocycle, Nano Lett. 17 (2017) 6620–6625. https://doi.org/10.1021/acs.nanolett.7b02486.

[145] A. Önsten, J. Weissenrieder, D. Stoltz, S. Yu, M. Göthelid, U.O. Karlsson, Role of defects in surface chemistry on Cu_2O(111), J. Phys. Chem. C. 117 (2013) 19357–19364. https://doi.org/10.1021/jp3112217.

[146] C. X. Kronawitter, C. Riplinger, X. He, P. Zahl, E.A. Carter, P. Sutter, B.E. Koel, Hydrogen-bonded cyclic water clusters nucleated on an oxide surface, J. Am. Chem. Soc. 136 (2014) 13283–13288. https://doi.org/10.1021/ja5056214.

[147] C. Möller and N. Nilius, Water Adsorption on Cu_2O(111) Surfaces – An STM study, J. Phys. Chem. C 121 (2017) 20877–20881. https://doi.org/10.1021/acs.jpcc.7b06996.

[148] C. Möller, J. Barreto, F. Stavale, H. Tissot, S. Shaikhutdinov, H.J. Freund, N. Nilius, Water adsorption to crystalline Cu_2O thin films: Structural and vibrational properties, J. Phys. Chem. C. 122 (2018) 2195–2199. https://doi.org/10.1021/acs.jpcc.7b10835.

[149] Z. Besharat, J. Halldin Stenlid, M. Soldemo, K. Marks, A. Önsten, M. Johnson, H. Öström, J. Weissenrieder, T. Brinck, M. Göthelid, Dehydrogenation of methanol on Cu_2O(100) and (111), J. Chem. Phys. 146 (2017). https://doi.org/10.1063/1.4989472.

[150] L. Bendavid, E. Carter, CO_2 adsorption on Cu_2O (111): A DFT+ U and DFT-D study, J. Phys. Chem. C. 117 (2013) 26048–26059. http://pubs.acs.org/doi/abs/10.1021/jp407468t.

[151] C. Riplinger, E.A. Carter, Cooperative Effects in water binding to cuprous oxide surfaces, J. Phys. Chem. C. 119 (2015) 9311–9323. https://doi.org/10.1021/acs.jpcc.5b00383.

[152] X. Yu, X. Zhang, S. Wang, G. Feng, A computational study on water adsorption on Cu_2O(111) surfaces: The effects of coverage and oxygen defect, Appl. Surf. Sci. 343 (2015) 33–40. https://doi.org/10.1016/j.apsusc.2015.03.065.

[153] R. Zhang, J. Li, B. Wang, L. Ling, Fundamental studies about the interaction of water with perfect, oxygen-vacancy and pre-covered oxygen Cu_2O(111) surfaces: Thermochemistry, barrier, product, Appl. Surf. Sci. 279 (2013) 260–271. https://doi.org/10.1016/j.apsusc.2013.04.078.

[154] R. Zhang, J. Li, B. Wang, L. Ling, Fundamental studies about the interaction of water with perfect, oxygen-vacancy and pre-covered oxygen Cu_2O(111) surfaces: Thermochemistry, barrier, product, Appl. Surf. Sci. 279 (2013) 260–271. https://doi.org/10.1016/j.apsusc.2013.04.078.

[155] X. Yu, X. Zhang, X. Tian, S. Wang, G. Feng, Density functional theory calculations on oxygen adsorption on the Cu_2O surfaces, Appl. Surf. Sci. 324 (2015) 53–60. https://doi.org/10.1016/j.apsusc.2014.10.056.

[156] Y. Guo, X. Yu, Q. Yu, Y. Li, Y. Liu, C. Zhao, L. Jin, Z. Liu, J. Li, Exploring stability of transition-metal single atoms on Cu_2O surfaces, J. Phys. Chem. C 126 (2022), 8065–8078. https://doi.org/10.1021/acs.jpcc.2c00751.

[157] C. Wang, Y. Kong, M. Soldemo, Z. Wu, H. Tissot, B. Karagoz, K. Marks, J.H. Stenlid, A. Shavorskiy, E. Kokkonen, S. Kaya, D.J. Stacchiola, J. Weissenrieder, Stabilization of Cu_2O through site-selective formation of a Co_1Cu hybrid single-atom catalyst, Chem. Mater. 34 (2022) 2313–2320. https://doi.org/10.1021/acs.chemmater.1c04137.

[158] D.F. Cox, K.H. Schulz, Interaction of CO with Cu^+ cations: CO adsorption on Cu_2O(100), Surf. Sci. 249 (1991) 138–148. https://doi.org/10.1016/0039-6028(91)90839-K.

[159] N.D. McClenaghan, P. Hu, C. Hardacre, A density functional theory study of the surface relaxation and reactivity of Cu_2O(100), Surf. Sci. 464, (2000) 223–232. https://doi.org/10.1016/S0039-6028(00)00678-6.

---

[160] D. Le, S. Stolbov, T.S. Rahman, Reactivity of the $Cu_2O(100)$ surface: Insights from first principles calculations, Surf. Sci. 603 (2009) 1637–1645. https://doi.org/10.1016/j.susc.2008.12.039.

[161] M.M. Islam, B. Diawara, V. Maurice, P. Marcus, Surface reconstruction modes of $Cu_2O(001)$ surface: A first principles study, Surf. Sci. 604 (2010) 1516–1523. https://doi.org/10.1016/j.susc.2010.05.020.

[162] M. Soldemo, J.H. Stenlid, Z. Besharat, M. Ghadami Yazdi, A. Önsten, C. Leygraf, M. Göthelid, T. Brinck, J. Weissenrieder, The surface structure of $Cu_2O(100)$, J. Phys. Chem. C. 120 (2016) 4373–4381. https://doi.org/10.1021/acs.jpcc.5b11350.

[163] H. Tissot, C. Wang, J. Halldin Stenlid, T. Brinck, J. Weissenrieder, The surface structure of $Cu_2O(100)$: Nature of defects, J. Phys. Chem. C 123 (2018) 7696–7704. https://doi.org/10.1021/acs.jpcc.8b05156.

[164] D.F. Cox, K.H. Schulz, H_2O adsorption on $Cu_2O(100)$, Surf. Sci. 256 (1991) 67–76. https://doi.org/10.1016/0167-2584(91)91161-O.

[165] K.H. Schulz, D.F. Cox, Surface hydride formation on a metal oxide surface: the interaction of atomic hydrogen with $Cu_2O(100)$, Surf. Sci. 278 (1992) 9–18. https://doi.org/10.1016/0039-6028(92)90579-U.

[166] S. Vollmer, G. Witte, C. Wöll, Results for CO adsorption to Cu(100), Catal. Lett. 77 (2001) 97-101. DOI10.1023/A:1012755616064.

[167] J.H. Stenlid, M. Soldemo, A.J. Johansson, C. Leygraf, M. Göthelid, J. Weissenrieder, T. Brinck, Reactivity at the $Cu_2O(100)$:Cu-H_2O interface: a combined DFT and PES study, Phys. Chem. Chem. Phys. 18 (2016) 30570–30584. https://doi.org/10.1039/C6CP04410G.

[168] K. Marks, Z. Besharat, M. Soldemo, A. Önsten, J. Weissenrieder, J.H. Stenlid, H. Ostrom, M. Gothelid, Adsorption and decomposition of ethanol on $Cu_2O(111)$ and (100), J. Phys. Chem. C 123 (2019) 20384-20392. https://doi.org/10.1021/acs.jpcc.9b05394.

[169] C. Wang, H. Tissot, C. Escudero, V. Pérez-Dieste, D. Stacchiola, J. Weissenrieder, Redox Properties of $Cu_2O(100)$ and (111) Surfaces, J. Phys. Chem. C. 122 (2018) 28684–28691. https://doi.org/10.1021/acs.jpcc.8b08494.

[170] S. Hong, D. Le, T. Rahman, Deactivation of $Cu_2O(100)$ by CO poisoning, Top. Catal. 56 (2013) 1082–1087. https://doi.org/10.1007/s11244-013-0073-7.

[171] M.A. Nygren, L.G.M Pettersson, H_2O interaction with the polar $Cu_2O(100)$ surface: A theoretical study, J. Phys. Chem. 100 (1996) 1874-1878. J. Phys. Chem. 100 (1996) 1874–1878. https://doi.org/10.1021/jp9524183

[172] C.A. Celaya, C. Delesma, S. Torres-Arellano, P.J. Sebastian, J. Muniz, Understanding CO_2 conversion into hydrocarbons via a photoreductive process supported on the $Cu_2O(100)$, (110) and (111) surface facets, Fuel 306 (2021) 121643, DOI10.1016/j.fuel.2021.121643.

[173] K.X. Yao, X.M. Yin, T.H. Wang, H.C. Zeng, Two types of Cu_2O nanocrystals unifaceted with {001} or {110} planes, J. Am. Chem. Soc. 132 (2010) 6131–6144. https://doi.org/10.1021/ja100151f.

[174] Q. Hua, D. Shang, W. Zhang, K. Chen, S. Chang, Y. Ma, Z. Jiang, J. Yang, W. Huang, Morphological evolution of Cu_2O nanocrystals in an acid solution: Stability of different crystal planes, Langmuir. 27 (2011) 665–671. https://doi.org/10.1021/la104475s.

[175] J. Lin, W. Hao, Y. Shang, X. Wang, D. Qiu, G. Ma, C. Chen, S. Li, L. Guo, Direct experimental observation of facet-dependent SERS of Cu_2O polyhedra, Small. 14 (2018) 1703274. https://doi.org/10.1002/smll.201703274.

[176] K. Matsuzaki, K. Nomura, H. Yanagi, T. Kamiya, M. Hirano, H. Hosono, Effects of post-annealing on (110) Cu_2O epitaxial films and origin of low mobility in Cu_2O thin-film transistor, Phys. Status Solidi Appl. Mater. Sci. 206 (2009) 2192–2197. https://doi.org/10.1002/pssa.200881795.

[177] Y. Tolstova, S.S. Wilson, H. a. Atwater, Single phase, single orientation $Cu_2O(100)$ and (110) thin films grown by plasma-assisted molecular beam epitaxy, J. Cryst. Growth. 410 (2015) 77–81. https://doi.org/10.1016/j.jcrysgro.2014.10.045.

[178] L. Li, R. Zhang, J. Vinson, E.L. Shirley, J.P. Greeley, J.R. Guest, M.K.Y. Chan, Imaging catalytic activation of CO_2 on Cu_2O (110): A first-principles study, Chem. Mater. 30 (2018) 1912–1923. https://doi.org/10.1021/acs.chemmater.7b04803.

---

[179] H. Chen, T. Fan, Y. Ji, CO_2 Reduction mechanism on the $Cu_2O(110)$ surface: A first-principles study, ChemPhysChem. (2023). https://doi.org/10.1002/cphc.202300047.

[180] W. Zou, L. Liu, L. Zhang, L. Li, Y. Cao, X. Wang, C. Tang, F. Gao, L. Dong, Crystal-plane effects on surface and catalytic properties of Cu_2O nanocrystals for NO reduction by CO, Appl. Catal., A 505 (2015) 334−343. https://doi.org/10.1016/j.apcata.2015.08.021.

[181] S.A. Saraireh, M. Altarawneh, Density functional theory periodic slab calculations of adsorption and dissociation of H_2O on the $Cu_2O(110)$:CuO surface, Canad. J. Physics 91 (2013) 1101-1106. https://doi.org/10.1139/cjp-2013-0272.

[182] M. Altarawneh, M.W. Radny, P. V. Smith, J.C. MacKie, E.M. Kennedy, B.Z. Dlugogorski, A. Soon, C. Stampfl, A first-principles density functional study of chlorophenol adsorption on Cu2 O (110):CuO, J. Chem. Phys. 130 (2009). https://doi.org/10.1063/1.3123534.

[183] I.C. Man, Ş.G. Şoriga, V. Pârvulescu, Theoretical study of the adsorption of bromobenzene and aniline on $Cu_2O(110)$:CuO and $Cu_2O(111)$:CuO surfaces, Chem. Phys. Lett. 604 (2014) 38–45. https://doi.org/10.1016/j.cplett.2014.04.043.

[184] K. H. L. Zhang, K. Xi, M. G. Blamire, R. G. Egdell, P-type transparent conducting oxides, J. Phys. Cond. Matt. 28I (2016) 383002. https:\\doi.org\10.1088/0953-8984/28/38/383002

[185] J.W. Hodby, T.E. Jenkins, C. Schwab, H. Tamura, D. Trivich, Cyclotron resonance of electrons and of holes in cuprous oxide, Cu 2O, J. Phys. C Solid State Phys. 9 (1976) 1429–1439. https://doi.org/10.1088/0022-3719/9/8/014.

[186] C.S. Weiner, N. Caswell, P.Y. Yu, M. A., Ortho- to para exciton conversion in Cu_2O, Solid State Commun. 46 (1983) 105–108. https://doi.org/10.1016/0038-1098(83)90588-4.

[187] D.W. Snoke, A.J. Shields, M. Cardona, Phonon-absorption recombination luminescence of room-temperature excitons in Cu_2O, Phys. Rev B. 45 (1992) 11693. https://doi.org/10.1103/PhysRevB.45.11693.

[188] N. Harukawa, S. Murakami, S. Tamon, S. Ijuin, A. Ohmori, K. Abe, T. Shigenari, Temperature dependence of luminescence lifetime in Cu_2O, J. Lumin. 89 (2000) 1231–1233. https://doi.org/10.1016/S0022-2313(99)00524-4.

[189] H. Stolz, F. Schöne, D. Semkat, Interaction of rydberg excitons in cuprous oxide with phonons and photons: Optical linewidth and polariton effect, New J. Phys. 20 (2018) 023019. DOI 10.1088/1367-2630/aaa396.

[190] J. Heckötter, M. Freitag, D. Fröhlich, M. Aßmann, M. Bayer, M.A. Semina, M.M. Glazov, High-resolution study of the yellow excitons in Cu_2O subject to an electric field, Phys. Rev. B. 95 (2017) 035210. https://doi.org/10.1103/PhysRevB.95.035210.

[191] K. Yoshioka, E. Chae, M. Kuwata-Gonokami, Transition to a Bose–Einstein condensate and relaxation explosion of excitons at sub-Kelvin temperatures, Nature Commun. 2 (2011) 328. https://doi.org/10.1038/ncomms1335.

[192] G.P. Pollack, D. Trivich, Photoelectric properties of cuprous oxide, J. Appl. Phys. 46 (1975) 163–172. https://doi.org/10.1063/1.321312.

[193] P.R. Markworth, R.P.H. Chang, Y. Sun, G.K. Wong, J.B. Ketterson, Epitaxial stabilization of orthorhombic cuprous oxide films on MgO(110), J. Mater. Res. 16 (2001) 914–921. https://doi.org/10.1557/JMR.2001.0130.

[194] H. Solache-Carranco, G. Juárez-Diaz, A. Esparza-García, M. Briseño-García, M. Galván-Arellano, J. Martínez-Juárez, G. Romero-Paredes, R. Peña-Sierra, Photoluminescence and X-ray diffraction studies on Cu_2O J. Lumin. 129 (2009) 1483. https://doi.org/10.1016/j.jlumin.2009.02.033.

[195] C. Ricca, L. Grad, M. Hengsberger, J. Osterwalder, U. Aschauer, Importance of surface oxygen vacancies for ultrafast hot carrier relaxation and transport in Cu_2O, Phys. Rev. Res. 3 (2021) 1–8. https://doi.org/10.1103/PhysRevResearch.3.043219.

[196] N. Dongfang, Y. S. Al-Hamdani, M. Iannuzzi, Understanding the role of oxygen-vacancy defects in $Cu_2O(111)$ from first-principle calculations, Electron. Struct. 5 (2023) 035001. https://doi.org/10.1088/2516-1075/ace0aa.

[197] L. Frazer, K.B. Chang, R.D. Schaller, K.R. Poeppelmeier, J.B Ketterson, Vacancy relaxation in cuprous oxide ($Cu_{2-x}O_{1-y}$), J. Lumin. 183 (2017) 281–290. https://doi.org/10.1016/j.jlumin.2016.11.011.

---

[198] Y. Yang, S. Niu, D. Han, T. Liu, G. Wang, Y. Li, Progress in Developing Metal Oxide Nanomaterials for Photoelectrochemical Water Splitting, Adv. Energy Mater. 7 (2017) 1–26. https://doi.org/10.1002/aenm.201700555.

[199] I. V. Bagal, N.R. Chodankar, M.A. Hassan, A. Waseem, M.A. Johar, D.H. Kim, S.W. Ryu, Cu2O as an emerging photocathode for solar water splitting - A status review, Int. J. Hydrogen Energy. 44 (2019) 21351–21378. https://doi.org/10.1016/j.ijhydene.2019.06.184.

[200] L. Wu, L.K. Tsui, N. Swami, G. Zangari, Photoelectrochemical stability of electrodeposited Cu2O films, J. Phys. Chem. C. 114 (2010) 11551–11556. https://doi.org/10.1021/jp103437y.

[201] K.A. Khan, Stability of a Cu2O photoelectrode in an electrochemical cell and the performances of the photoelectrode coated with Au and SiO thin films, Appl. Energy. 65 (2000) 59–66. https://doi.org/10.1016/S0306-2619(99)00060-4.

[202] Y. Yang, J. Han, X. Ning, J. Su, J. Shi, W. Cao, W. Xu, Photoelectrochemical stability improvement of cuprous oxide (Cu2O) thin films in aqueous solution, Int. J. Energy Res. 2016; 40 (2016) 112–123. https://doi.org/10.1002/er.

[203] C. T. Campbell, Ultrathin metal films and particles on oxide surfaces: Structural, electronic and chemisorptive properties, Surf. Sci. Rep. 27 (1997) 1-111, DOI10.1016/S0167-5729(96)00011-8.

[204] M. Bäumer, H.J. Freund, Metal deposits on well-ordered oxide films, Prog. Surf. Sci. 61 (1999) 127-198, DOI 10.1016/S0079-6816(99)00012-X.

[205] N. Nilius, Properties of oxide thin films and their adsorption behavior studied by scanning tunneling microscopy and conductance spectroscopy, Surf. Sci. Rep. 64 (2009) 595-659. https://doi.org/10.1016/j.surfrep.2009.07.004.

[206] L. Trinkler, D. Dai, L. Chang, M.M. Chou, T. Wu, J. Gabrusenoks, D. Nilova, R. Ruska, B. Berzina, R. Nedzinskas, Luminescence Properties of Epitaxial Cu_2O Thin Films Electrodeposited on Metallic Substrates and Cu 2 O Single Crystals, Materials (Basel). 16 (2023) 4349. https://doi.org/10.3390/ma16124349.

[207] M. Borgwardt, S.T. Omelchenko, M. Favaro, P. Plate, C. Höhn, D. Abou-Ras, K. Schwarzburg, R. van de Krol, H.A. Atwater, N.S. Lewis, R. Eichberger, D. Friedrich, Femtosecond time-resolved two-photon photoemission studies of ultrafast carrier relaxation in Cu_2O photoelectrodes, Nat. Commun. 10 (2019) 1–7. https://doi.org/10.1038/s41467-019-10143-x.

[208] H.M. Benia, P. Myrach, N. Nilius, Photon emission spectroscopy of thin MgO films with the STM: from a tip-mediated to an intrinsic emission characteristic, New J. Phys. 10 (2008) 013010. https://doi.org/10.1088/1367-2630/10/1/013010.

[209] L. Novotny, B. Hecht, Principles of Nano-Optics, (Cambridge Univ. Press, 2006). https://doi.org/10.1017/CBO9780511813535.

[210] R. Berndt, R. Gaisch, J. K. Gimzewski, B. Reihl, R. R. Schlittler, W. D. Schneider, M. Tschudy, Photon-emission at molecular resolution induced by STM, Science 262 (1993) 1425-1427, DOI10.1126/science.262.5138.1425.

[211] P. Johansson, R. Monreal, Theory for photon emission from a scanning tunneling microscope, Zeitschrift für Phys. B Condens. Matter. 84 (1991) 269–275. https://doi.org/10.1007/BF01313548.

[212] N. Nilius, A. Gloystein, Luminescence from Cuprous Oxide in a Scanning Tunneling Microscope: Competition between Plasmonic and Excitonic Response, *ACS Photonics* 9 (2022) 3625-3632. DOI10.1021/acsphotonics.2c01109.

[213] H.M. Benia, N. Nilius, H.-J. Freund, Photon mapping of MgO thin films with an STM, Surf. Sci. Lett. 601 (2007) L55. https://doi.org/10.1016/j.susc.2007.03.017.

[214] G. Mahieu, B. Grandidier, D. Deresmes, J.P. Nys, D. Stiévenard, P. Ebert, Direct evidence for shallow acceptor states with nonspherical symmetry in GaAs, Phys. Rev. Lett. 94 (2005) 1–4. https://doi.org/10.1103/PhysRevLett.94.026407.

[215] F. Stavale, N. Nilius, H.-J. Freund, Probing the luminescence of single Eu_2O_3 nanoislands on MgO(001) with STM, Appl. Phys. Lett. 101 (2012) 013109. https://doi.org/10.1063/1.4731638.

[216] A Gloystein, N. Nilius, Copper oxide phases probed via plasmonic light emission in the STM, New J. Phys. 23 (2021) 093021. https://doi.org/10.1088/1367-2630/ac219f.

---

[217] A. Gloystein, M. Soltanmohammadi, N. Nilius, Light Emission from Single Oxygen Vacancies in Cu_2O Films Probed with Scanning Tunneling Microscopy, *J. Phys. Chem. Lett* 14 (2023) 3980-3985. https://doi.org/10.1021/acs.jpclett.3c00642.

[218] S. Becker, J.A. Golovchenko, B.S. Schwartzentruber, Electron Interferometry at Crystal Surfaces, Phys. Rev. Lett. 55 (1985) 987. https://doi.org/10.1103/PhysRevLett.55.987.

[219] J. Martínez-Blanco, S. Fölsch, Light emission from Ag(111) driven by inelastic tunneling in the field emission regime. J. Phys.: Condens. Matter 27 (2015) 255008. https://doi.org/ 10.1088/0953-8984/27/25/255008.

[220] A. Gloystein, C. Möller, N. Nilius, Negative differential conductance in the electron-transport through copper-rich cuprous oxide thin films, *New J. Phys.*21 (2019) 113026. https://doi.org/10.1088/1367-2630/ab51f2.

[221] Z. Zhao, X. He, J. Yi, C. Ma, Y. Cao, J. Qiu, First-principles study on the doping effects of nitrogen on the electronic structure and optical properties of Cu_2O, RSC Adv. 3 (2013) 84–90. https://doi.org/10.1039/c2ra22297c.

[222] Y.S. Lee, J. Heo, M.T. Winkler, S.C. Siah, S.B. Kim, R.G. Gordon, T. Buonassisi, Nitrogen-doped cuprous oxide as a p-type hole-transporting layer in thin-film solar cells, J. Mater. Chem. A. 1 (2013) 15416–15422. https://doi.org/10.1039/c3ta13208k.

[223] Ø. Nordseth, R. Kumar, K. Bergum, I. Chilibon, S.E. Foss, E. Monakhov, Nitrogen-doped Cu_2O thin films for photovoltaic applications, Materials 12 (2019) 3038. https://doi.org/10.3390/ma12183038.

[224] S. Ishizuka, S. Kato, Y. Okamoto, K. Akimoto, Hydrogen treatment for polycrystalline nitrogen-doped Cu_2O thin film, J. Cryst. Growth. 237–239 (2002) 616–620. https://doi.org/10.1016/S0022-0248(01)01975-3.

[225] Y.M. Lu, C.Y. Chen, M.H. Lin, Effect of hydrogen plasma treatment on the electrical properties of sputtered N-doped cuprous oxide films, Mater. Sci. Eng. B Solid-State Mater. Adv. Technol. 118 (2005) 179–182. https://doi.org/10.1016/j.mseb.2004.12.046.

[226] Y.S. Lee, M.T. Winkler, S.C. Siah, R. Brandt, T. Buonassisi, Growth and p-type doping of cuprous oxide thin-films for photovoltaic applications, Conf. Rec. IEEE Photovolt. Spec. Conf. (2012) 2557–2558. https://doi.org/10.1109/PVSC.2012.6318116.

[227] S. Cheng Siah, Y. Seog Lee, Y. Segal, T. Buonassisi, Low contact resistivity of metals on nitrogen-doped cuprous oxide (Cu_2O) thin-films, J. Appl. Phys. 112 (2012) 2010–2015. https://doi.org/10.1063/1.4758305.

[228] S. Masudy-Panah, K. Radhakrishnan, A. Kumar, T.I. Wong, R. Yi, G.K. Dalapati, Optical bandgap widening and phase transformation of nitrogen doped cupric oxide, J. Appl. Phys. 118 (2015). https://doi.org/10.1063/1.4936318.

[229] J. Benz, K.P. Hering, B. Kramm, A. Polity, P.J. Klar, S.C. Siah, T. Buonassisi, The influence of nitrogen doping on the electrical and vibrational properties of Cu_2O, Phys. Status Solidi Basic Res. 254 (2017) 1–5. https://doi.org/10.1002/pssb.201600421.

[230] F. Ye, J.J. Zeng, Y. Bin Qiu, X.M. Cai, B. Wang, H. Wang, D.P. Zhang, P. Fan, V.A.L. Roy, Deposition-rate controlled nitrogen-doping into cuprous oxide and its thermal stability, Thin Solid Films. 674 (2019) 44–51. https://doi.org/10.1016/j.tsf.2019.02.005.

[231] M.A.M. Patwary, M. Ohishi, K. Saito, Q. Guo, K.M. Yu, T. Tanaka, Effect of Nitrogen Doping on Structural, Electrical, and Optical Properties of CuO Thin Films Synthesized by Radio Frequency Magnetron Sputtering for Photovoltaic Application, ECS J. Solid State Sci. Technol. 10 (2021) 065019. https://doi.org/10.1149/2162-8777/ac0a98.

[232] R. Asahi, T. Morikawa, H. Irie, T. Ohwaki, Nitrogen-Doped Titanium Dioxide as Visible-Light-Sensitive Photocatalyst: Designs, Developments, and Prospects, Chem. Rev. 114 (2014) 9824–9852. https://doi.org/10.1021/cr5000738.

[233] Z.Y. Zhao, J. Yi, D.C. Zhou, Electronic structures of halogen-doped Cu_2O based on DFT calculations, Chinese Phys. B. 23 (2014). https://doi.org/10.1088/1674-1056/23/1/017401.

[234] M. Nolan, S.D. Elliott, Tuning the transparency of Cu_2O with substitutional cation doping, Chem. Mater. 20 (2008) 5522–5531. https://doi.org/10.1021/cm703395k.

---

[235] M. Sieberer, J. Redinger, P. Mohn, Electronic and magnetic structure of cuprous oxide doped with Mn, Fe, Co, and Ni: A density-functional theory study, Phys. Rev. B. 75 (2007) 035203. https://doi.org/10.1103/PhysRevB.75.035203.

[236] A. Larabi, A. Mahmoudi, M. Mebarki, M. Dergal, First principle investigation of hydrogen behavior in M doped Cu_2O (M = Na, Li and Ti), Condens. Matter Phys. 22 (2019) 23702. https://doi.org/10.5488/CMP.22.23702.

[237] N. Kikuchi, K. Tonooka, Electrical and structural properties of Ni-doped Cu_2O films prepared by pulsed laser deposition, Thin Solid Films. 486 (2005) 33–37. https://doi.org/10.1016/j.tsf.2004.12.044.

[238] A. Chowdhury, P.K. Bijalwan, R.K. Sahu, Investigations on the role of alkali to obtain modulated defect concentrations for Cu_2O thin films, Appl. Surf. Sci. 289 (2014) 430–436. https://doi.org/10.1016/j.apsusc.2013.10.183.